SAPIENZA
UNIVERSITÀ DI ROMA

Development of an innovative device for beam range monitoring in particle therapy

Scuola di Dottorato in Fisica

Dottorato di Ricerca in Fisica – XXX Ciclo

Candidate

Giacomo Traini

ID number 1239980

Thesis Advisor

Prof. Vincenzo Patera

Co-Advisor

Prof. Adalberto Sciubba

A thesis submitted in partial fulfillment of the requirements
for the degree of Doctor of Philosophy in Physics

31 October 2017

Thesis not yet defended

Development of an innovative device for beam range monitoring in particle therapy
Ph.D. thesis. Sapienza – University of Rome

This thesis has been typeset by LaTeX and the Sapthesis class.

Author's email: giacomo.traini@roma1.infn.it

Contents

Introduction

According the WHO (*World Health Organisation*), cancer is the second leading cause of death globally, and accounted for 8.8 million death in 2015 [1]. Nowadays, three main therapies are mainly used for tumour treatment: surgery, in which the tumour is mechanically removed, chemotherapy, in which the cancer cells death is induced by drugs, and radiotherapy, in which the tumour is exposed to radiations to kill the ill cells. A kind of therapy, or more often a combination of them, is chosen according the tumour biological properties and localisation in the human body.

The *Particle Therapy* (PT) is a particular kind of radiation therapy in which accelerated light ions beams are exploited instead of photons, commonly used in conventional radiotherapy. One of the most advantageous PT features is its capability to achieve high localised dose distribution, allowing to concentrate most of the energy release in the tumour volume. As a results, the undesired amount of radiation absorbed by the healthy tissues is minimised, and the probability of side effects occurrence is reduced. Moreover, charged particles induce more efficiently the tumour cell death than photons, better resulting in the radio-resistant tumours therapy .

One of the most important still open issue in PT is represented by the treatment quality assurance: despite the therapy efficacy, a control system capable to provide a real-time feedback on the dose distribution delivered to the patient is missing in the clinical practice. The planned target volume has to be stretched with respect to the tumour boundaries to prevent partial tumour irradiations, degrading the intrinsic precision of the PT. For the same reason, the treatment have to be administered in multiple sessions ($\sim$10 for a full treatment, each one taking $\sim$20 minutes), increasing costs. Since in PT the capability to deliver an the dose at a certain depth depends from the capability to properly predict the beam range in the patient, the scientific community have addressed several researches to develop on-line beam range verification techniques. In PT the beam particles does not escape from the patient, and the most followed approach consists of an indirect range measurement, exploiting the secondary particles produced due to the nuclear interaction between the beam projectiles and the crossed tissues nuclei.

In this thesis, an innovative range verification technique that exploits charged secondary fragments, particularly suitable for ^{12}C ion treatments, is proposed. The development of a detector, named *Dose Profiler* and specifically designed for this purpose, is presented. The Dose Profiler has been developed within the INSIDE (*INnovative Solution for hadrontherapy*) collaboration, to be used in the treatment room of CNAO (*Centro Nazionale di Terapia Oncologica*), combined with a PET-like detector, thought to monitor the beam range by means of the β^+ activity induced

by the beam interactions in the patient.

In chapter 1 the PT is introduced, reviewing the underlying physics processes and the biological consequences of the interactions between a therapeutic beam and the human tissues.

In chapter 2 the secondary particles emitted in a PT treatment and the related beam range monitoring techniques currently under investigation are illustrated, discussing their features and limitations. A brief review of some measurement performed to evaluate the feasibility of charged secondary particles monitoring is presented.

In chapter 3 the Dose Profiler design is described: the development of the detector layout, the front-end electronics, the trigger and data acquisition systems are examined.

In chapter 4 the beam range reconstruction algorithm is investigated, and the expected detector performances evaluated by means of Monte Carlo simulation are reported.

In chapter 5 the measurements performed to characterise the Dose Profiler are presented. Cosmic rays have been exploited to preliminary tune the detector, then a test-beam at Trento Proton Therapy centre has been performed to evaluate the detector response with protons at energies of interest for PT applications. The measured detection efficiency and spatial resolution are shown.

In chapter 6 the preliminary results of the data-taking campaign performed at CNAO to study of the secondary charged fragments, produced by Carbon ion beams impinging an anthropomorphic phantom, are presented. The emission profiles of charged secondary fragments are shown, and a preliminary analysis on the technique applicability in a clinical scenario is carried out.

Chapter 1

Particle Therapy

The idea to use radiations for cancer therapy was born as soon as X-Rays were discovered by Wilhelm Röntgen, in 1895. From the empirical observation of the severe burns caused by the radiation exposure on the normal tissues, it followed immediately that the X-Rays capability to damage cells could have been exploited to treat diseases in which destructive effects are beneficial, as cancers. From the biological point of view, radiation therapy kills cancer cells by damaging their DNA, avoiding the cells reproductions and inducing cell apoptosis. When the damaged cells die, they are broken down and eliminated by the body's natural processes.

In the conventional modern radiotherapy X-Rays are delivered to the patient, with two main different methods according the type of tumour and the placement in the body. Radiation could come from radioactive material conveniently placed close to the tumour (internal radiation therapy, also named *Brachytherapy*), or can be sent in the form of photon beam by means of electrons acceleration with a LINAC (external-beam radiation therapy), reaching photon by energies up to 25 MeV.

The physical *dose* (D), defined as the energy loss by ionising radiation per mass unit (eq. 1.1), is used to quantify the radiation effects. It is expressed in *gray* ($1\ Gy = 1\ J/kg$)

$$D = \frac{dE}{dm} \tag{1.1}$$

As it will be discussed in this chapter, the dose is connected to the biological damage level induced to the cells. In radiation therapy 100% of the planned dose would be delivered in the target volume, represented by the tumour boundaries. Unfortunately X-Rays absorption can not be completely restricted to the cancer cells, but healthy tissues are involved as well, due to the X-Rays ballistic. This leads to the appearance of side effects, that may occur months or years after the therapy administration, including a large set of pathologies depending on the cancer type, i.e. fibrosis, infertility or a second cancer caused by radiation exposure [2]. The cutting-edge technology actually available in traditional radiotherapy is the IMRT (*Intensity-Modulated Radiation Therapy*), in which six up to nine non co-planar photon beams are used to build up an highly conformal dose distribution [3], helping to spare the healthy tissues and organs at risk close to the tumour.

In the last decades, an alternative form of radiation therapy called *Particle Therapy* (also called *Hadrontherapy* or *ion-therapy*) is widespread increasing. In PT

accelerated light ion beams, mainly protons or ^{12}C ions, in the energy range of 50-250 MeV (protons) and 150-400 MeV/u (^{12}C ions), are used instead of photons. The main advantage led by charged ions is due to their characteristic energy loss curve: most of the kinetic energy released by a charged particle is localised at the end of the particle path, in a few mm wide region called *Bragg Peak* (BP). This peculiar property allows to build treatment plans in which the undesired dose to healthy tissues results considerably lower than what is possible to achieve in conventional radiotherapy. Moreover, the different physics processes involved in the energy loss in PT lead to a higher biological damage to the cells, especially for ^{12}C ions treatments, making the PT recommended for radio-resistant tumours treatment.

Although the idea to use charged particles for medical purposes has been proposed for the first time in 1946 by R. Wilson [4], the development of PT has principally occurred in the last 20 years thanks to accelerators building cost reduction, as a consequence of the acquisition of new knowledges and technologies on hadron accelerators, used for the fundamental research in particle physics. The diffusion of PT is now strongly growing year on year: according the PTCOG (*Particle Therapy Co-Operative Group*), an international organisation that promotes the PT in the world, there are 62 active facilities, 43 are under construction and more than 20 are planned to be built in the next years [5]. From 1950s until 2015 155k patients have been treated with PT, 130k with proton beams, 20k with ^{12}C ion beams and the remaining with different kind of charged particles (^{4}He ion, π^{-}).

In this chapter the particle therapy is presented. Firstly the physics processes underlying the PT concepts are reviewed, as well as the biological effects. Finally the beam range monitoring issue in PT is introduced.

1.1 Physical bases

The purpose of this section is to make a description of the physics processes that govern the dose release in PT. The interaction of charged particles crossing a material is well known by physicists, since is of paramount importance for the development of particle detection devices. In a general treatment on the interaction of charged particles with matter, *light* charged particles (e^{-}, e^{+}) have to be distinguished from *heavy* charged particles (muons, protons, pions, α-particles, and other heavier ions), since different physics processes are involved. According the goal of this section, only the physics of heavy charged particles will be treated.

1.1.1 Energy loss

When a heavy charged particle passes through matter, the most probable process that takes place is the inelastic collision with the atomic electrons of the material. In each collision a small fraction of the kinetic energy is lost, being transferred to the electron. If this amount of energy is larger than the electron-nucleus binding energy, the electron comes out from the atomic shell and becomes free, ionising the atom. In rare cases the transferred energy could be enough to generate δ-rays, electrons which can travel far away from the impact point and that are their-self source of other ionisations processes. In any case, the energy usually transferred in a single

collision is small, but since a large number of collisions occurs also in thin layer of normal dense material, the incident particle significantly reduces the kinetic energy until it is stopped or exits from the medium. The average energy lost by a particle per path unit is called *stopping power* (S):

$$S = -\frac{dE}{dx} \tag{1.2}$$

The dose released in a thin slice material with density ρ and considering a parallel particle beam with flux F can be calculated in eq. 1.3

$$D\,[Gy] = 1.6 \cdot 10^{-9} \cdot \frac{dE}{dx}\left[\frac{keV}{\mu m}\right] \cdot F\left[\mathrm{cm}^{-2}\right] \cdot \frac{1}{\rho}\left[\frac{\mathrm{cm}^3}{g}\right] \tag{1.3}$$

where S is the stopping power defined above.

The Linear Energy Transfer (LET) is a quantity often used in radiation dosimetry, defined as the amount of the transferred energy from a ionising radiation to a medium per unit distance only due to electronic collisions. It is clearly related to the stopping power S, since they coincide when the other possible energy loss processes (for instance nuclear collisions, *Bremsstralhung*) are negligible.

For charged particles in the energy range commonly used in PT treatments (50-450 MeV/u), the inelastic collisions with electrons represent the main contribution to the stopping power. *Bremsstralhung* is totally negligible at these energies (so it is excluded from this treatise). The elastic scattering with nuclei give generally a low contribution to the amount of energy lost, since the nuclei mass is bigger than the projectile mass. When this assumption is not valid, also this contribution should be considered.

The stopping power due to the atomic electron collisions was firstly evaluated by Bohr, using classic mechanics (for more details see [7]). The Bohr's formula was later revisited by Bethe and Bloch, that made the correct calculations using quantum mechanics arguments. The final equation, commonly known as *Bethe-Bloch* formula, is reported in eq. 1.4, and all the physical constants used are described in the table 1.1.

$$-\frac{dE}{dx} = 2\pi\frac{N_A Z\rho}{A}\frac{r_e^2 m_e c^2 z^2}{\beta^2}\left(ln\frac{2m_e c^2\beta^2\gamma^2 W_{max}}{I^2} - 2\beta^2 - \delta(\gamma) - 2\frac{C}{Z}\right) \tag{1.4}$$

W_{max} indicates the maximum energy that can be transferred in a collision. From simple kinematic consideration it results to be:

$$W_{max} = \frac{2m_e c^2\beta^2\gamma^2}{1 + \frac{2m_e}{M}\sqrt{1+\beta^2\gamma^2} + \frac{m_e^2}{M^2}} \tag{1.5}$$

The mean excitation potential I is the average energy needed to excite an electron of the target material. It's a difficult quantity to analytically calculate, because the frequencies of the single atomic levels for each atomic species have to be known. It is generally indirectly deduced by dE/dx measurements. The δ term takes into

N_A	Avogadro's number
Z	Atomic number of absorbing material
A	Atomic weight of absorbing material
ρ	Density of absorbing material
r_e	Classical e^- radius
m_e	e^- mass
c	Light speed
z	Charge of projectile (in units of e)
β	v/c of projectile
γ	Lorentz factor

Table 1.1

account of the fact that the electric field of the incident particle tends to polarise the crossed medium. Due to this polarisation the electrons more distant to the particle trajectory are shielded and they give a lower contribution to the energy loss. It clearly depends of the medium density ρ, so it is named *density effect*, and it counts more when the projectile speed is high. The C term, also named *shell correction*, takes into account for the effects that arise when the incident particle velocity is comparable with the electrons one.

From the eq.1.4 it follows that the stopping power for non relativistic particles is dominated by the $1/\beta^2$ factor. The dE/dx rapidly decreases with increasing the velocity, reaching a minimum, and then it follows a slowly increasing trend, with a logarithmic dependence on the relativistic factor $\beta\gamma$ (*relativistic rise*). In figure 1.1 an example of the stopping power for different kind of particle is shown. The minimum weakly depends of the kind of incident particles, and particles at this point are called MIP (*Minimum Ionizing Particles*). For particles travelling in the same material, the stopping power varies due to the charge z and the mass M, leading to different Bethe-Bloch curves. This features is often used to make particle identification in particle physics experiments.

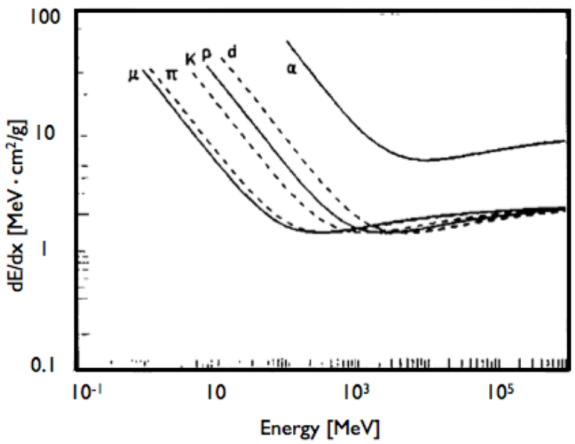

Figure 1.1. Bethe-Bloch curve for different type of charged particles as a function of the kinetic energy [8].

The Bethe-Bloch equation refers to an *average* energy loss per length unit. In fact for a given charged particle the number of collisions with atomic electrons is affected by statistical fluctuation, as well as the energy lost in a single collision. As a consequence, the measured energy spectrum of a monochromatic charged particle beam after the passage through a layer of a given thickness is actually broaden, since the energy loss is different for each single particle. This is known as *Energy straggling*. For relatively thick absorbers the number of collision is well described by a *gaussian* distribution, since the *Central limit theorem* can be assumed. For thinner absorber more complicated models, proposed by Landau and Vavilov, are needed to predict the deposited energy distributions. A more detailed discussion on this argument is out of the purpose of this thesis.

The more interesting consequence driven by the aforementioned considerations is the fact that a heavy charged particles lose most of its kinetic energy when it is stopping, that means at the end of the path in the crossed medium. This feature is the key point on which PT is based. In the figure 1.2 a typical curve of the stopping power as a function of the penetration depth is shown: as the path length increases the dE/dx becomes higher, reaching a peak in proximity of the path ending, where is deposited most of the energy. At the very end, since the charged particles start to pick-up the atomic electrons of the target, the stopping power has a fast drop until the particle is fully stopped. This curve is named *Bragg curve*, and the peak is commonly known as *Bragg peak*.

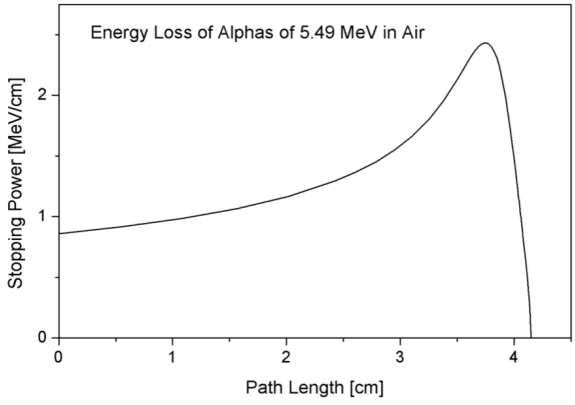

Figure 1.2. Typical Bragg curve [6].

The Bragg peak depth depends both on the incident particle kinetic energy and the crossed material density, while the width is of the order of few mm, and it is caused by the energy straggling. Then, to cover the full tumour volume, beams with different energies are used. The dose distribution that results from the overlapping of different energies beams is commonly named *Spread-Out Bragg Peak* (SOPB), whose an example is shown in figure 1.3. The SOBP is built also taking into account the different biological effects (as will be discussed in 1.2 that the tissues undergo for different beam energies. The particles can be delivered to the patient with two main different strategies: passive beam modulation and active beam scanning. In the first approach the initially narrow beam is first broadened by a scatterer device, while

different Bragg peak depths are obtained by means of passive range modulators. Each patient needs a dedicated hardware according the tumour localisation. For fully active beam delivery the target volume is divided in layers of equal beam energy (*slice*), and each *slice* is divided in smaller elements (*voxels*). The dose on each slides is delivered with a monochromatic beam, irradiating each voxel deflecting the beam particles by means of deflection magnets.

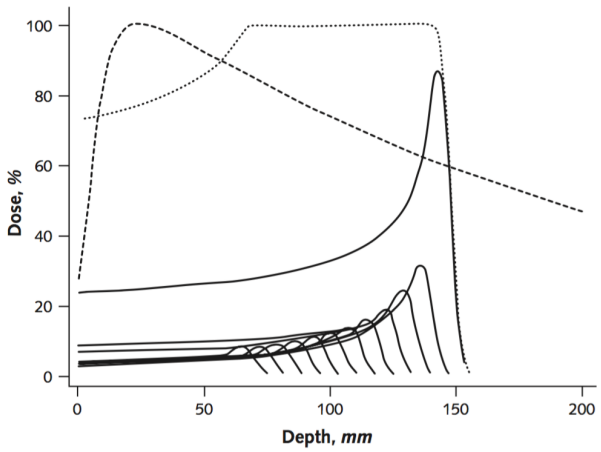

Figure 1.3. The dotted line shows a typical Spread-Out Bragg peak, obtained by the different dose distribution with different Bragg peaks overlap [9]. Instead, the dashed line shows the typical dose distribution given by photons, which reach is maximum after few cm and after exponentially decreases with the depth increasing.

1.1.2 Range

A quantity naturally connected to the energy loss is the total distance that a charged particle of a given energy E_0 can cover travelling in a medium before stopping, also called *range* (R). The range can be experimentally measured sending a monochromatic charged particles beam on targets with different thickness, measuring the fraction of escaped particles for each target as a function of the thickness. In this way, a curve similar to what is shown in the figure 1.4 is achieved. The stochastic nature of the energy loss process, that leads to the energy straggling phenomenon, has implications also for the particle range, since particles with identical initial energy have slightly different ranges (in this case we speak about *range straggling*). Thus, the falling edge of the aforementioned curve is not straight but it follows a smooth line. A *mean range* can be defined as the range at which half of the incoming particles are stopped. In most of practical cases it is more convenient to know the length in which a beam is fully absorbed, called *extrapolated range*. This value is taken extrapolating the tangent to the curve at half height to zero.

According the given definition the range is actually not equal to the total distance covered by the particle in the target, because due to the multiple scattering the trajectory is not straight but it follows a zigzag path. Neglecting this effect and the straggling as well, the range could be derived from the equation 1.4 as follows:

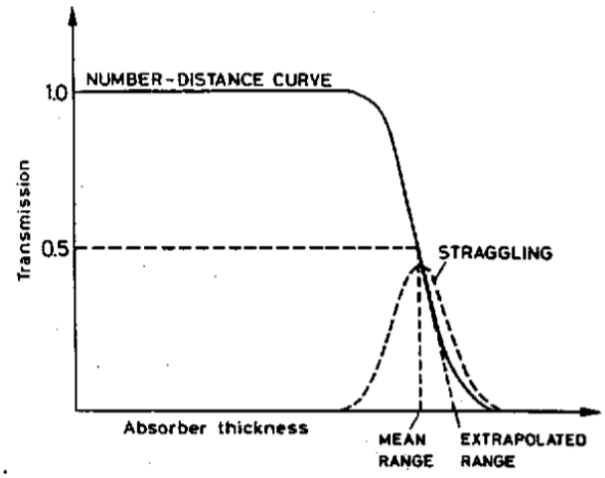

Figure 1.4. Typical curve showing the fraction of transmitted particles as a function of the target thickness [8].

$$R = \int_0^{E_0} \left(\frac{dE}{dx}\right)^{-1} dE' \tag{1.6}$$

This definition is very useful to give raw estimates of ranges using scale laws. For instance it is easy to see that, given a material, for two different ions having respectively masses M_1, M_2, charges z_1, z_2, and the same energy per nucleon the range scale according the equation 1.7:

$$\frac{R_2}{R_1} = \frac{M_2}{M_1}\frac{z_1^2}{z_2^2} \tag{1.7}$$

An example of the range in H_2O as a function of the projectile energy is shown in the figure 1.5.

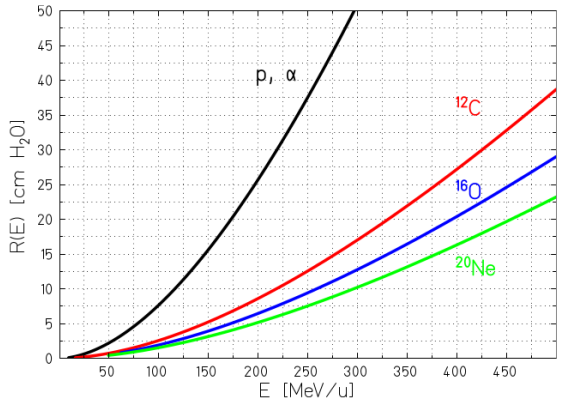

Figure 1.5. Range in H_2O for different kind of ions [9]

1.1.3 Coulomb multiple scattering

Another important interaction that arises when a charged particle passes through the matter is the Coulomb scattering with the target nuclei. The cross-section for this process has been calculated for the first time by Rutherford in 1911, as a result of the famous experiment in which a beam of α particles has been sent on a thin layer of gold to investigate the atomic structure of the matter. It is expressed in the following equation 1.8.

$$\frac{d\sigma}{d\Omega} = z^2 Z^2 r_e^2 \frac{m_e^2 c^2}{4\beta^2 p^2 sin^4(\frac{\theta}{2})} \tag{1.8}$$

This formula is achieved with classical mechanics reasoning, and it's valid under the assumption of non-relativistic projectile with a mass much larger than the nucleus one, thus the nucleus recoil is small and energy transferred is neglected. In the eq. 1.8, p stands for the momentum of the incoming particle, θ is the deflection angle. Due to the dependency on $sin^4(\theta/2)$, it' clear that small deflection angles are more probable. In general the single elastic scattering events occur with lower probability with respect to the inelastic collision with atomic electrons, and for a very thin layer of material the probability to have more than one collision is small: in this case the angular distribution for the deflected particles is given directly by the Rutherford formula. When the number of collision is higher we talk about of *multiple scattering*, but in this case the mathematical calculations are very complicated and a lot of different models are used to evaluate the net deflection suffered by the particle. An exhaustive analysis of such models falls outside of the purpose of this thesis, but it is useful to make a brief description of the gaussian approximation, since it is valid in most of the interesting cases. In fact for most of practical uses, excluding the tails due to the large-angle scattering, the angular distributions can be well approximated by a gaussian distribution centred in $\theta = 0$, with root mean squared θ_0. A reasonable estimate of θ_0 is given by the following empirical formula:

$$\theta_0 = \frac{13.6MeV}{\beta cp} z \sqrt{x/X_0} \left[1 + 0.0038\ ln(x/X_0)\right] \tag{1.9}$$

where p is the momentum of the particle, x is the distance covered in the target, and X_0 is the radiation length of the material. The X_0 definition is provided by eq.1.10.

$$\frac{1}{X_0} = 4\alpha r_e^2 \frac{N_A}{A} \left\{ Z^2 \left[L_{rad} - f(Z) \right] + Z L'_{rad} \right\} \tag{1.10}$$

where the $f(Z)$, L_{rad} and L'_{rad} are provided by [10].

Due to the multiple scattering the therapeutical beam is broadened, especially for low mass ions as p, or α particles, and the delivered dose results laterally spread-out. In fig 1.6, the typical spread for ^{12}C ions and protons in a treatment beam line is shown.

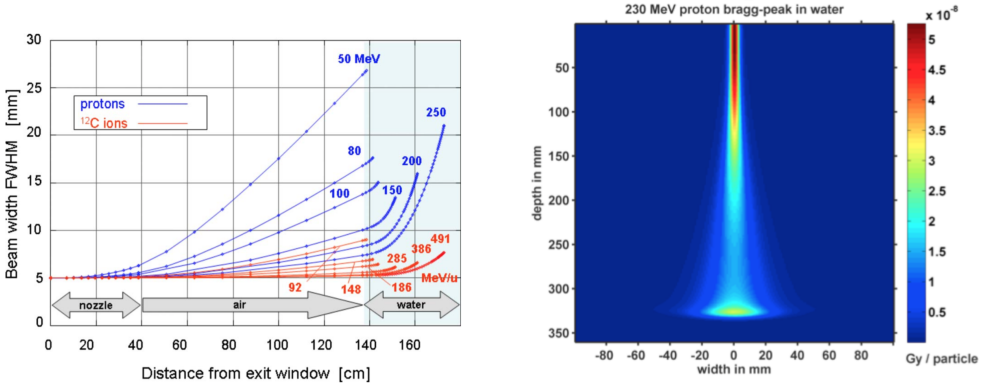

Figure 1.6. Calculated beam spread for ^{12}C ions and protons in a typical treatment beam line [11].

1.1.4 Nuclear fragmentation

For ions of PT interest at energies of several hundreds MeV/u, β is sufficiently high to go beyond the Coulombian barrier, so reactions between nuclei may occur, typically violent nuclear spallation reactions that lead in a complete disintegration of the projectile and target nucleus, or in partial fragmentation. Nuclei are composite particles: each nucleus is composed by protons and neutrons, which are composed by quarks and gluons. Quarks, gluons and their dynamics are mostly confined within nucleons, but residual influences extend slightly beyond nucleon boundaries to give rise to the *nuclear force*, that governs the nucleons-nucleons interactions. The quantum chromodynamics (QCD) is the fundamental theory that describes interactions between quarks and gluons, but at the nucleon energy of interest (hundreds of MeV/u) could not be successfully applied to make predictions on nucleus-nucleus collisions, due to the high complexity of mathematical calculations. This has led to the development to empirical or semi-empirical effective models based on experimental data.

Many simple parametrisations of nuclear interaction use a geometrical approximation, in which the nuclei are assumed to be simply spheres. The collisions between nuclei can be distinguished in central and peripheral collisions depending on the size of the impact parameter with respect to the size of the interacting particles. Central collisions occur for small values of the impact parameter, and are characterised by an almost complete destruction of both the projectile and target nuclei. In these violent processes a large number of particles come out over a wide range of angles. In such a collision, practically all nucleons in both colliding partners are participants. On the other hand, the peripheral collisions occur with increasing size of the impact parameter, and only a few nucleons in the overlap zone effectively interact during the collision. Using the geometrical approximation, the inclusive cross-section for nuclear reactions σ_R is:

$$\sigma_R = \pi(r_p + r_T)^2 \tag{1.11}$$

where r_p is the projectile radius, and r_T the target one. Exploiting the empirical parametrisation of nuclear radius $r = r_0 A^{1/3} - b$, and taking into account of the

projectile energy (E) dependence by means of available experimental data, a generic formula, used for instance for cosmic radiation transport code by NASA, is achieved:

$$\sigma_R(E) = \pi r_0^2 c_1(E)(A_p^{\frac{1}{3}} + A_T^{\frac{1}{3}} + c_2(E))^2 \tag{1.12}$$

where $c_1(E)$ and $c_2(E)$ are two functions that depends on the kind of considered projectile. The equation 1.12 gives reasonable evaluation of the fragmentation cross-section for different ion species, in the energy range from few hundreds MeV/u up to ∼1 GeV/u.

A model often used to describe the physics processes that occurs fragmentation is the so called*ablation-abrasion* model, that describes the nucleus-nucleus collisions through two distinct steps: in the *ablation* stage, which have a time scale of 10^{-22} - 10^{-23}s, the projectile and the target nucleus overlap, and the composition of the interaction partners may be modified, leaving the nuclei in an excitation state. In the *abrasion* state the system thermalizes and de-excites by evaporation of neutrons, protons or light nuclei as well as by fission and emission of gamma rays, with a characteristic time that can variate from 10^{-21}s to 10^{-16}s. A graphical representation of the abrasion-ablation model is shown in the figure 1.7

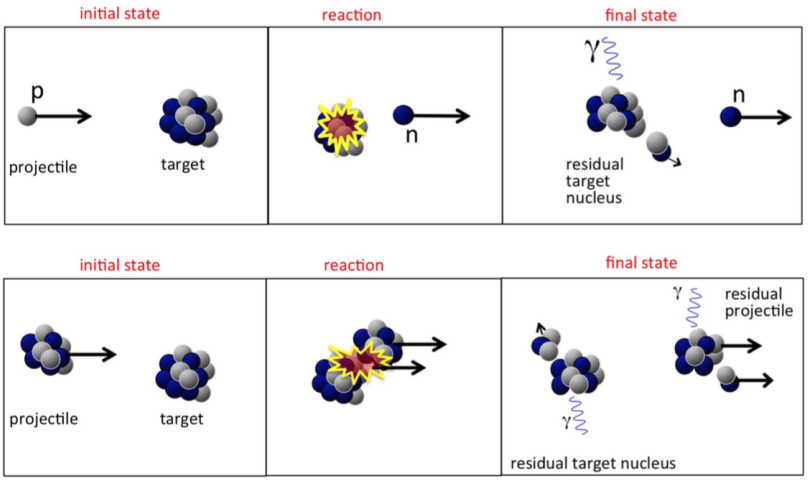

Figure 1.7. Sketch of a typical proton-nucleus reaction (top) and nucleus-nucleus reaction (bottom) [12].

Notwithstanding nuclear interactions are rarer than the electromagnetic processes described in the sections above, they have a great relevance in PT. The main consequences are:

- Primary beam fluence loss. The number of particles deposited at a certain depth depends on the amount of inelastic collisions that the beam particles undergo. For instance, just ∼ 80% of proton hitting a water target at 160 MeV actually stop in the Bragg peak [13]. For Carbon-ions this fraction is generally lower: ∼ %50 of the total primary Carbon ion flux at 290 MeV/u arrives at Bragg peak [14].

- The dose distributions are modified. In the buildup region of the Bragg curve, secondary particles contribute considerably to the total energy deposition. Moreover, the height of the Bragg peak is modified. In addition, in case of heavy ion irradiation, dose is also delivered beyond the Bragg peak, as shown in figures 1.8 and 1.9. The low energetic secondary particles (including neutrons), which are typically emitted at larger angles, contribute to the low dose envelope around the beam. The consequent biological effects cannot be neglected because the charged fragments can be particularly damaging.

- Several secondary particles, that can potentially exit from the patient, are produced. As it will be more clear in the section 1.3, such particles are currently used to develop beam range monitoring techniques.

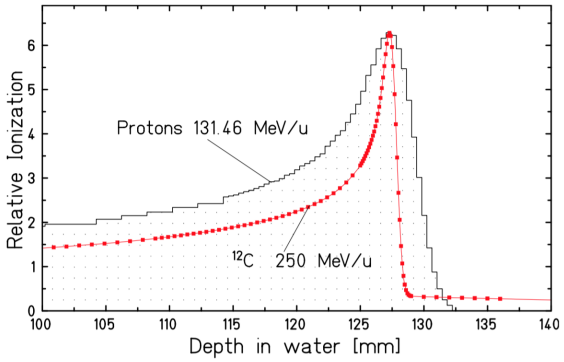

Figure 1.8. Dose released by a 131 MeV proton beam in water (black line), and by a ^{12}C ion beam at 250 MeV/u (red line). The latter shows the characteristic dose tail beyond the Bragg peak due to the fragmentation [15]

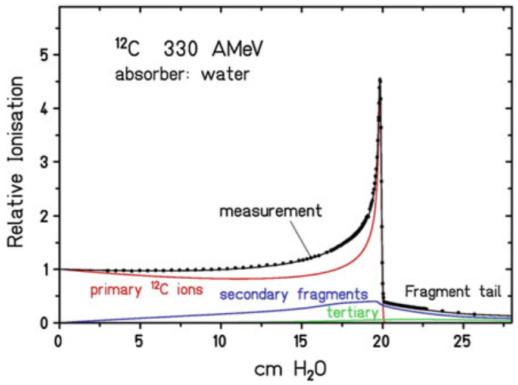

Figure 1.9. Dose contributions of primary ions, secondary and tertiary fragments calculated for 330 MeV/u ^{12}C ion beam stopping in water [16]

1.2 Biological effects

The capability of radiations to provoke the tumour cells death and to prevent their reproduction is related to the capability to inflict irreparable lesions to the cells DNA. Since charged particles cause more severe DNA damages with respect to photons, in addition to the the advantages offered by the peculiar depth-dose profile, particle therapy results particularly convenient with respect to conventional radiotherapy due to the enhanced biological effectiveness in cell killing. This feature makes PT very attractive for the treatment of radio-resistant local tumours.

1.2.1 DNA strand break and ionisation density

The tumour cells damages can be provoked in indirect or direct way. In the former case, the ionised electrons interacting with water molecules produce free radicals (OH^-, H^+), that chemically damage the DNA [17]. In the other case, the primary radiation induces DNA damage by direct ionisations of the DNA molecules. However, the degree of DNA lesion complexity directly depends on the LET, i.e. the ionisation density of the radiation [18]. Photons dose deposition is almost homogeneous in the region of a cell because it is the result of many ionising events which are statistically distributed over the whole volume. Considering a typical radiotherapy photon beam, the distance between two ionisations is > 200 nm. Instead, the dose deposition of an ion passing through a cell is highly concentrated in the track core. The mean free path d between two consequent ionisation events is a function of the projectile charge Z^2 and kinetic energy, increasing in correspondence of the Bragg peak when the projectile is slower. ^{12}C ion d is of the order of few nm. In figure 1.10 the difference of the ionisation in H_2O produced by protons and ^{12}C ions is shown, respectively.

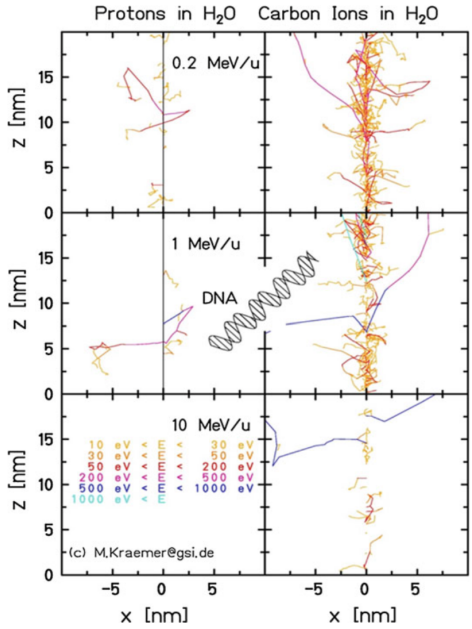

Figure 1.10. Tracks of δ-electrons produced by energetic protons and ^{12}C ions penetrating tissue. The particles enter at x = 0 and move along the z-axis [19]

Since the typical DNA helix dimension is ~ 2 nm, multiple ionisation occur with a higher probability in PT, leading to the creation of DNA *double-strand breaks* (DSB), which are the most irreparable DNA-damages. Other common kind of DNA damages are schematically illustrated in 1.11.

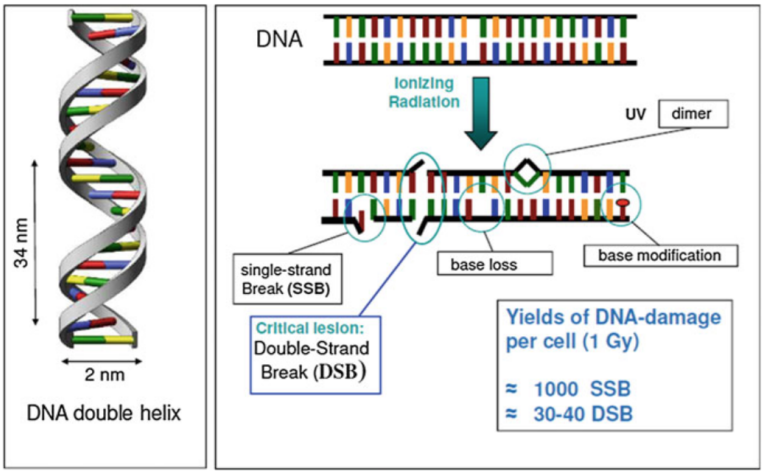

Figure 1.11. DNA-damage induced by ionizing radiation[20]

1.2.2 RBE

The increased effectiveness of charged particles compared to photons is quantified by the Relative Biological Effectiveness (RBE), defined as the ratio of photon and charged particle doses resulting in the same biological effect (eq. 1.13).

$$RBE = \frac{D_{\text{X-Rays}}}{D_{\text{ion}}}\Big|_{\text{isoeffect}} \tag{1.13}$$

The RBE is a complex quantity, depending on physical parameters (i.e., particle type, dose, LET) as well as on biological ones (i.e., tissue type, cell cycle phase, oxygenation level, end point). As a result, the RBE is different for every location in the treatment field, and this has to be taken into account in treatment planning. For fast moving light ions, at the beginning of their path in tissues, the LET is very low and hence RBE is approximately one, while for slow light ions near the BP position, the LET is very high and so it is the RBE (figure 1.12).

In clinical practice a constant RBE = 1.1 is often used in proton treatments [21, 22], considering protons biological effects not much different from photons, since there are not clear clinical evidences against this assumption. Nevertheless, recent studies indicate that RBE variation in proton treatments should be reconsidered, since it seems relevant in particular for normal tissues in the entrance region and for organs at risk close behind the tumour [23], as schematically shown in figure 1.13.

A typical RBE evaluation method consists in the irradiation of a cell sample, measuring the cell survival (S) fraction as function of the absorbed dose. In the standard experimental protocol [24], cell proliferation is analysed about 1-2 weeks

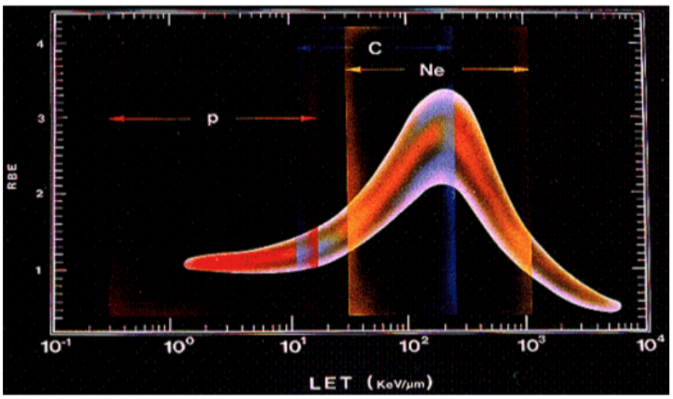

Figure 1.12. RBE as a function of LET for different kind of ions.

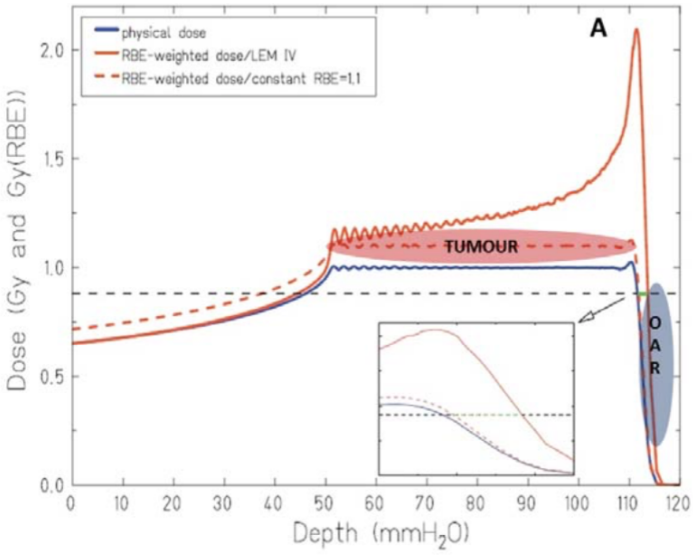

Figure 1.13. Physical and RBE-weighted dose are shown, as obtained with a constant and with a variable RBE. Special emphasis is given to the differences at the distal fall-off, where organ at risk might be located [23].

after irradiation and cells are counted. Typical survival fraction curves for ions and photon irradiation as a function of the dose are shown in figure 1.14, on a logarithmic scale. Ions show an almost exponential relationship between survival and dose, represented as a straight line on the semi-log plot. Instead, X-rays curve shows a non-linear behaviour in form of a shoulder. Survival curves are commonly parametrised with the *linear-quadratic* model [17], given by eq. 1.14

$$S(D) = e^{-\alpha D + \beta D^2} \tag{1.14}$$

where the coefficient α describes the slope at small doses and gives the initially produced irreparable damage, and β the influence of repair which is important at higher doses. The ratio α/β is therefore a measure for the repair capacity of the

cells and takes typical values of 1-3 Gy for cells with high repair potential and close to 10Gy for repair-deficient cells.

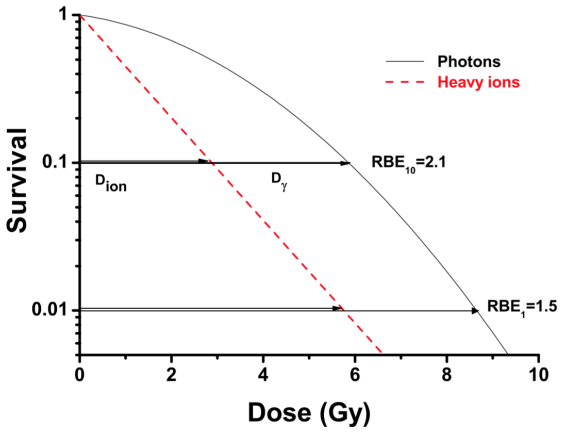

Figure 1.14. Determination of RBE for cell inactivation for 10% and 1% survival level for a typical heavy ion irradiation [11].

1.2.3 OER

Since free radicals are responsible for some DNA lesions, the oxygen level in the tumour tissues has a impact on the radio-sensitivity of the tumour itself. Tumour volume growth is possible only if new vessels are generated to oxygenate tumour cells, but if vessels are not generated sufficiently fast or don't work well, hypoxic regions can develop within the tumour. These regions are usually deep inside the cancer mass, reducing the therapy effectiveness. The Oxygen Enhancement Ratio (OER) parameter, defined if eq. 1.15 has been introduced to give an estimate of such effect.

$$\mathrm{OER} = \frac{D_{hypoxic}}{D_{aerobic}} \tag{1.15}$$

Tumour

$D_{hypoxic}$ and $D_{aerobic}$ are respectively the doses with reduced and normal oxygen supply resulting in the same clinical effect. Contrary to RBE, the OER is a dose-modifying factor and independent of dose. OER typical values are ~ 3 for high-hypoxic tumours, while are ~ 1 for well oxygenated tumours. In figure 1.15 cell survival fraction, reported in [25], can be observed for different kind of radiation and OER. The difference between hypoxic and normal cells is reduced for high-LET radiation. A consistent behaviour has been found for a wide variety of ions and cell lineages [26, 27, 28, 29]. Such effect is expected: high-LET radiation as heavy-ions cause cells damages mainly by direct hit of DNA helix, whereas for low-LET radiation as X-Rays the damages are indirectly inflicted by free-radicals, whose production is affected by the amount of oxygen in cells. Therefore, heavy particles such as carbon ions offer are less sensible to the tumour oxygen level, having a great potential for curing tumours with hypoxic regions.

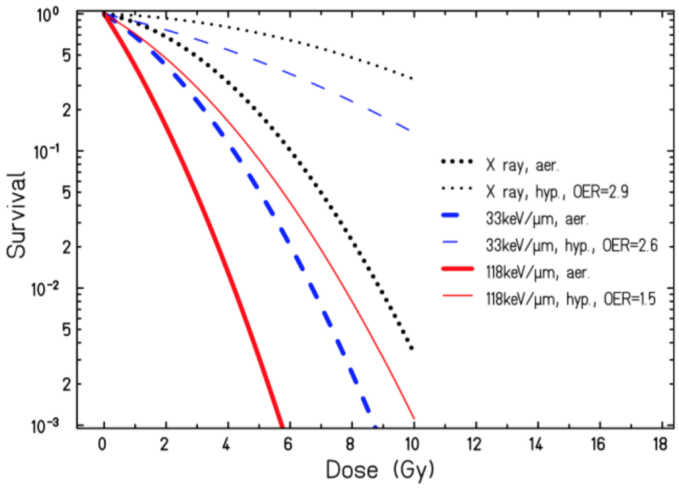

Figure 1.15. Influence of oxygen level on cell survival of human kidney cells for carbon ions at different energies and hence different LET [25].

1.3 Dose monitoring

As it was already stated in this chapter, charged particles offer the possibility to deposit dose much more locally than the photons, thanks to the characteristic dose deposition profile, so that the dose released in healthy tissue can be minimised. On the other hand, PT treatments are more sensitive to beam range uncertainties than photon treatments, because of their steep dose profile. Given a monoenergetic beam, a wrong range estimate results in a shift of the Bragg peak position, leading to an under-dosage of the tumour volume, and at the same time an over-dosage of healthy tissue surrounding the tumour, avoiding to fully profit of the intrinsic PT precision capabilities. A common error source could derive from the organ motion, due to the patient breath. To guarantee the target position stability, the patient is generally kept on the table with the aid of external supports like belts or special masks. However, in some cases the motion caused by breathing is non negligible, for instance when the tumours are localised in the abdomen or in the thorax. The motion is responsible for not only the dislocation of the tumour but also the alterations in the internal density along the beam path, which influence the range of particle beams. The consequences are schematically illustrated in figure 1.16, in which the impact difference between photons and ^{12}C ion beam is highlighted. This effect is almost negligible for photons, and it could have a large impact with carbon ions, where a large amount of energy could be deposited outside the tumour volume (red vertical lines).

Different strategies could be applied to face the problem:

- Rescanning. This approach is based on a statistical dose averaging effect by repeated irradiations of the expanded target volume, using scanned particle beams [30, 31]. The non correlation between the beam motion and the target motion is exploited, and the variance of the average dose decreases with a factor of $1/\sqrt{N}$, with N the scan repetition times [32]. Since the dose per scan

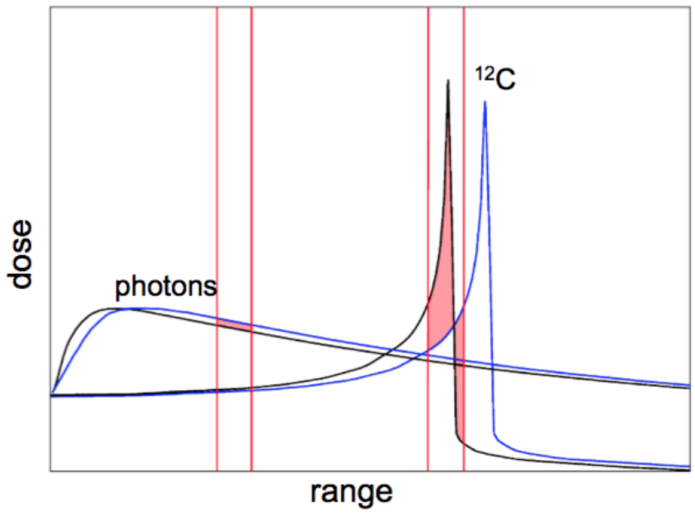

Figure 1.16. Effect of beam range variation. The blue line represent the planned range, while the black line shown the actual delivered dose due to a wrong beam range. The effect is negligible for photons, but could lead to significant a amount of released dose in undesired region in case of ion beam.

has to be lowered, the disadvantage of this technique is on the irradiation time which is extended. Moreover, the beam monitoring ionisation chambers are not sensitive to low currents.

- Gating. The patient irradiation is activated in only in certain instants during respiration cycle, where the target position could be considered almost fixed, requiring a time-resolved monitoring of the respiration. Around the point of maximum exhalation the respiratory signal shows a flat minimum (1.17), so the irradiation is only activated if the signal amplitude stays below a predefined limit, reducing the tumour motion during the irradiation time of $\sim 10\%$ [33]. Also this technique leads to much longer treatment times.

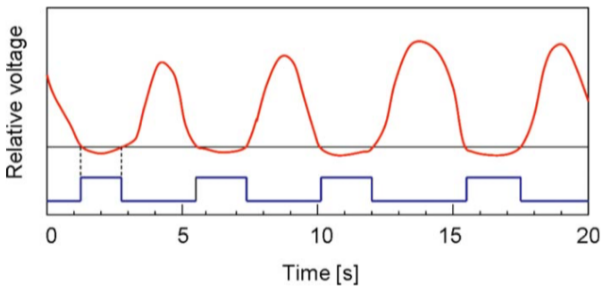

Figure 1.17. Respiratory-gated irradiation principle. The red signal is given by the patient respiration, while the blue is usdd to modulate the irradiation. Ationdapted from [33]

- Motion tracking. The motion compensation can be performed by a real-time tumour tracking. Different techniques are currently under investigation: the

organ motion can be directly measured by means of fluoroscopy and internal radio-opaque fiducial markers, electromagnetic detection and radio-frequency transponders implanted in the patient [34, 35, 36], or in some cases with the help of ultrasonography [35, 37, 38]. Another solution is the prediction of the motion pattern based on respiratory-correlated CT [four-dimensional CT 4D-CT] [39, 40, 38].

However, motion induced by the patient respiration is not the only one reason of mismatch between the planned dose and the actually delivered dose. The sources of beam range error with respect to predictions include anatomical changes (e.g., organ motion, Tumour regression, weight loss), physiological variations, uncertainties in CT Hounsfield units (HU), conversion of HU into particle stopping power, and reconstruction artifacts [41, 42]. All these effects give an overall uncertainty of the order of few millimetres that can be larger than the dimension of the Bragg peak. At present, systems capable to check the target volume dose conformity during the treatment, i.e. on-line, are still missing. The solution applied in treatments is to extend the target volume using *safety margins* of few mm [43, 44], estimated generally with empirical considerations, in order to have a reasonable assurance to cover the whole tumour region. However, this approach clearly degrades the treatments quality, since a fraction of the dose is delivered to healthy tissues. A great effort has been made in the last decades to develop on-line dose monitoring system for PT applications. In addiction to the former considerations, the possibility to have an instantaneous feedback on the delivered dose spatial distribution would allow to reconsider the treatment hypofractionation, which may result in an increased treatment efficacy, due to the larger RBE, and at same time a cost reduction, that still represent an obstacle to the PT diffusion. Considering that in PT all the beam is absorbed in the patient body, the exiting residual beam can not be exploited as in radiotherapy, but techniques based on secondary particles detection have to be developed.

Chapter 2

Beam range monitoring with secondary particles

During PT treatments a large amount of secondary particles is produced, as an outcome of the target or projectile nuclei fragmentation, due to the nuclear interaction (see section 1.7). Secondary photons, neutrons and different types of charged particles are emitted by the patient. The characterisation of such particles in terms of kinetic energy and emission angle spectra has been object of several research in the last decades, in order to evaluate the possibility to develop beam range verification techniques. The main secondary particles produced in PT and the related monitoring technique currently under investigation from the scientific community are illustrated in this chapter.

2.1 Annihilation γ

As a results of fragmentation processes, the passage of the beam in the patient can create β^+ emitters isotopes, which decay emitting a e^+ and a ν_e. The positron travel for few mm inside the patient, until it annihilates with an atomic electron, producing a couple of back-to-back photons with energy of 511 keV. Hence, the emitters activity can be measured with PET-like scanners, reconstructing the emitters distribution inside the patient (proposed for the first time by [45] in 1969). The fragmentation reaction can occur both on the incident particles (projectile fragmentation) and target nuclei (target fragmentation), except in case of proton beams where only the target fragmentation is clearly possible. The β^+ emitters typically produced in PT with the respective lifetimes are summarised in table 2.1. Experimental measurements of β^+ activity production on PMMA target by proton and ^{12}C ions beam are reported in [46, 47].

The mechanism of production affects the shape of the ion-induced activity and its correlation to the deposited dose. In case of proton projectiles, the activated nuclei have very low kinetic energies, and stop in proximity of the interaction point. The resulting emission profile, i.e. the spatial distribution of the e^+ annihilation points, shows a quite flat behaviour and a steep falling edge in correspondence of the Bragg peak (figure 2.2a), due to the energy threshold of reactions [50]. Conversely, projectile fragments keep the projectile boost, travelling much more and accumulating

Radionuclide	Half live (min)	Nuclear reaction channels / Threshold energies (MeV)
^{15}O	2.037	^{16}O(p,pn)^{15}O/16.79
^{11}C	20.385	^{12}C(p,pn)^{11}C/20.61, ^{14}N(p,2p2n)^{11}C/3.22, ^{16}O(p,3p3n)^{11}C/59.64
^{13}N	9.965	^{16}O(p,2p2n)^{13}N/5.66, ^{14}N(p,pn)^{13}N/11.44
^{30}P	2.498	^{31}P(p,pn)^{30}P/19.7
^{38}K	7.636	^{40}Ca(p,2p2n)^{38}K/21.2

Figure 2.1. Most favoured nuclear reaction channels for proton-induced positron emitter productions [48, 49]

at the range end. This results in a peaked activity signal, shown in figure 2.2b. Both kind of correlation with the deposited dose can be exploited for treatment verification, comparing the expectations based on the treatment plan with the PET measurements [51]. A clinical example of Monte Carlo predicted and measured PET distributions in a nasal cavity melanoma is shown in figure 2.3.

At present, the development of *in-beam* techniques, where the data acquisition is performed during the patient irradiation, is under investigation. However, the PET-γ detection is used in clinical practice to perform an after-treatment dose validation, with *offline* and *in-room* approaches. The main features and limitations of the aforementioned techniques are briefly summarised hereafter.

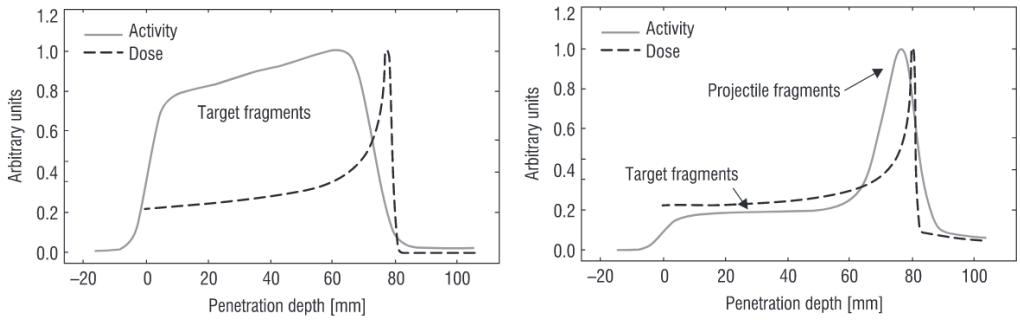

Figure 2.2. PMMA target activation, irradiated with a 110 MeV proton beam (left) and with a 212 MeV/u carbon ion beam (right). The solid line shows the distribution of the β^+ activity in function of the depth, while the dotted line indicates the dose released distribution of the primary beam in function of the depth [52]

2.1.1 Offline and in-room monitoring

In the *offline* approach commercial scanners, placed in a nearby dedicated room, are used to measure the β^+ emitters activity after the treatment [54, 55], resulting attractive because the relatively low costs. Full-ring scanners are commonly used, allowing to maximise the detection angle to enhance the signal level. Long acquisition

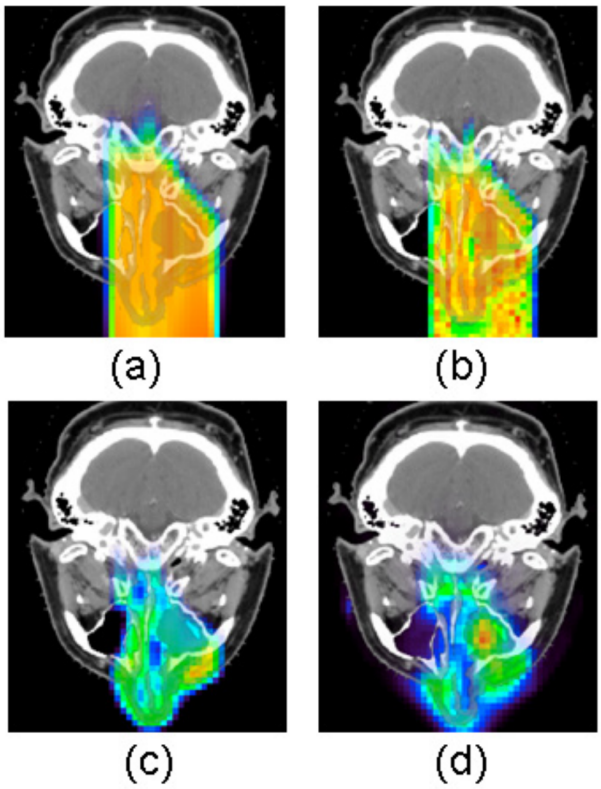

Figure 2.3. (a) Treatment planning dose distribution; (b) Monte Carlo simulated dose distribution; (c), Monte Carlo simulated PET activity distribution; (d), PET measurement. A good agreement is observed between the measured PET activity and the Monte Carlo predictions [53].

times are needed to achieve good results, because a large fraction of the emitters decays during the unavoidable time needed to transfer the patient from the treatment room to the PET room. Moreover, during this time, the correlation between the β^+ activity and the released dose is reducing, resulting in a resolution worsening, due to the biological wash-out. This limitation could be slightly reduced with the *in-room* approach, in which the PET-scanner is localised within the treatment room [56], minimising the patient relocation.

2.1.2 In-beam monitoring

Despite the PET-imaging has been explored for a long time, the application in a *in-beam* monitoring system has represents a challenging issue. Indeed, the radioactivity produced during the treatment is two orders of magnitude below the typical activity administered in standard imaging, and the main β^+ emitting isotopes have a decay time that ranges from $\sim$ 2min, for the ^{15}O radioactive isotope, up to $\sim$ 20min for the ^{11}C, which are comparable with the treatment duration ($\sim$ 10 min). Moreover, it is not possible to install a standard full-ring PET scanner to monitor the patient during the irradiation, then only a double-head system is allowed, limiting the angular acceptance and then reducing the event collection. Hence, a low level of

signal is generated, and a large background due to random coincidences caused by neutrons and prompt-γ (see section 2.2) is also expected, especially in ^{12}C ion beams treatments, where also a lower number of β^+ emitters is produced with respect to proton beams treatments. Promising results with proton beams are achieved by a PET-system proposed by INSIDE collaboration, composed by two LFS (Lutetium Fine Silicate) planar heads of 10×25 cm^2 area, read-out by Silicon PhotoMultipliers [57]. This device, which is being integrated in the CNAO (Centro Nazionale di Adroterapia Oncologica) treatment room, is currently in testing phase. In figure 2.5 the β^+ emitters activity profiles obtained by a PMMA phantom impinged by proton beams, delivering a real treatment plan, are shown. A very good agreement is observed with the predicted distribution evaluated by means of a Monte Carlo simulation.

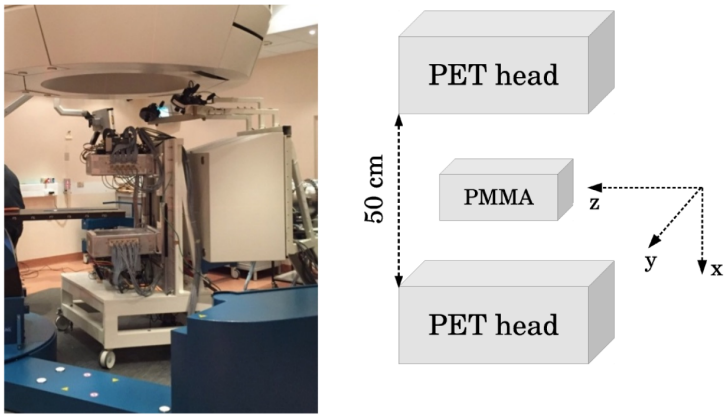

Figure 2.4. Left: the INSIDE in-beam PET installed in one of the CNAO treatment rooms. Right: schematic picture of the experimental set-up [57]. The beam direction is parallel to the positive z axis.

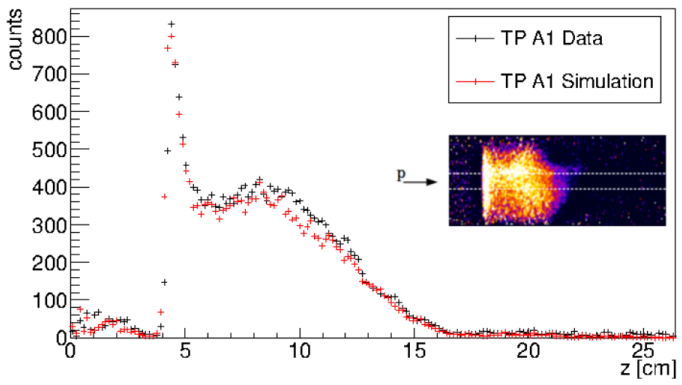

Figure 2.5. Experimental (black curves) and simulated (red curves) activity profiles of real treatment plans (TP) [57].

2.2 Prompt-γ

Prompt-γ term refers to the photons produced by the de-excitation of nuclei excited in the interactions between hadrons and matter. The decays occur with a characteristic time of the order of ~ 1 ns. The idea to use prompt-γ detection to monitor beam ranges in PT was proposed in 2003 in[58], and recent studies have been shown a correlation between the delivered dose and the prompt-γ emission profile, as shown in figure 2.6, for proton and ^{12}C ions impinging different kind of targets [59, 60]. In particular, the correlation between ion range and the emission shape distal fall-off can be exploited for the treatment verification, via a comparison between measured and predicted distributions, in accordance with the treatment planning. Prompt-γ are emitted almost isotropically, in an energy range between 1 MeV and 10 MeV [61, 62]. Thanks to their *prompt* production, the biological wash-out does not have any impact on the beam range reconstruction, unlike PET method. In principle prompt-γ detection could be performed by means of a SPECT (Single Photon Emission Computer Tomography) gamma camera, which is basically composed by a scintillators system for photon detection and localisation, and a collimation system, typically made by lead plates, to select the desired photon direction. The distance between the collimator holes and their thickness depend on the the photon energy, and are responsible for the system spatial resolution and detection efficiency. Unfortunately, the prompt-γ wide energy range avoid to use standard collimators, since huge absorbers would be used, resulting in a low detection efficiency and spatial resolution. Furthermore, a large uncorrelated background due to secondary neutrons, as well as to photons produced by neutrons interactions in the environment, limits the technique performances, particularly in 12C ion beams treatments. Different solutions have been proposed by scientific community. A quick review of the technique under investigation follows hereafter.

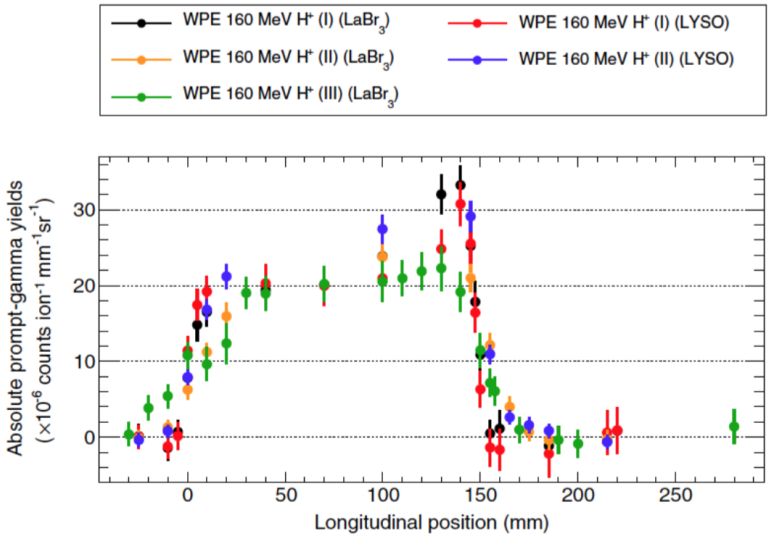

Figure 2.6. Prompt-γ emission profiles obtained irradiating a PMMA target with proton beams at different energies, measured by [60].

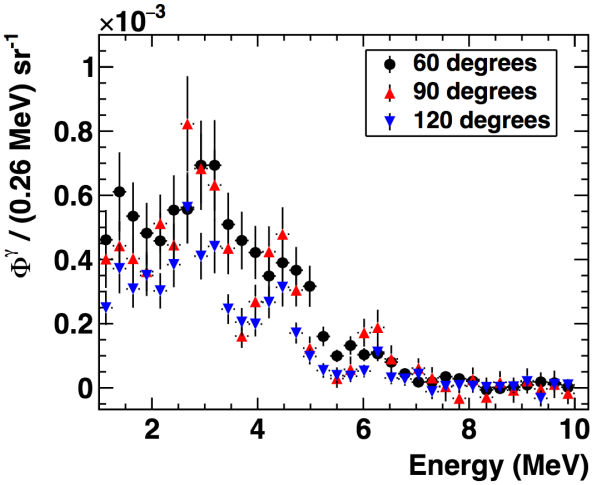

Figure 2.7. Energy spectra of prompt-γ emitted by a PMMA phantom impinged with a 220 MeV/u ^{12}C ion beam and detected at 60° (circles), 90°(triangles up) and 120° (triangles down) with respect to the beam direction [62].

2.2.1 Mechanical collimation

Several different collimators geometries have been investigated, looking for a trade-off between a good spatial resolution and high detection efficiency. The first attempt has been performed using a collimator with a parallel slit geometry [63]. This system is not capable to acquire the full field of view during a single measurement, but has to be moved in different positions. This kind of approach is hard to implement in a PT treatment, because the dose delivering time is not sufficient to collect enough statistics to reconstruct the prompt-γ profile fall-off. To overcome this limitation, the proposed solution are the parallel multi-slit collimation system [64], that can be made large enough to cover the full field of view, and the knife-edge slit collimator [65], which can cover a larger detection area thanks to the slit aperture angle. As sketched in figure 2.8, slit collimation gives a 1D projection of prompt-γ emissions along the beam path on a scintillation detector, making this technique well suited to the measure of a single pencil beam. An accuracy of the order of 1 mm on a single proton pencil beam has been achieved coupling a knife-edge slit camera with LYSO crystal scintillators read-out by SiPMs [65].

2.2.2 Compton cameras

To avoid the use of collimation system, Compton scattering events in a segmented detectors could be exploited to reconstruct the incoming photon direction, providing an higher detection efficiency. Typically, a Compton camera consists of one scatter detector and one absorber detector [66], as schematically illustrated in figure 2.9. The first one is designed to maximise the Compton scattering probability. When a photon of energy E_γ scatters inside the detector, it produces a recoil electron that releases all its kinetic energy E_e inside the detector itself, lowering the incoming photon energy down to $E'_\gamma = E_\gamma - E_e$. Such photon is finally totally absorbed in

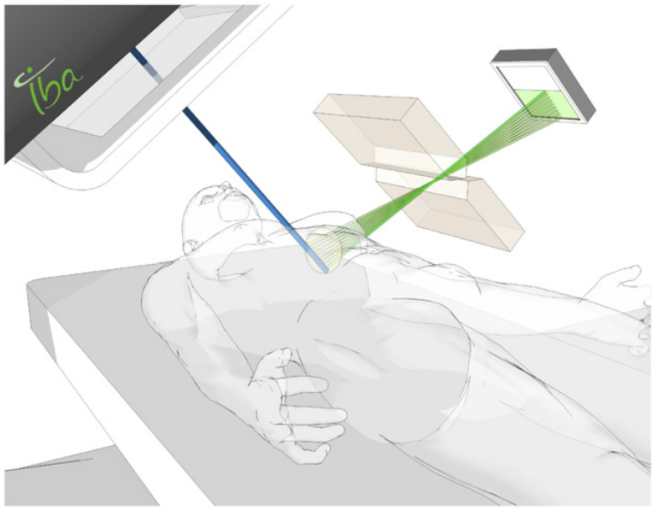

Figure 2.8. Principle of working of prompt-gamma imaging with a knife-edge slit camera [65]

the second detector. It is possible, from the measurement of the deposited energies and interaction positions in both detectors, to reconstruct cones containing their incident trajectories using the Compton kinematic constraints, using the eq. 2.1

$$cos\theta = 1 - m_e c^2 \left(\frac{1}{E'_\gamma} - \frac{1}{E_\gamma} \right) \tag{2.1}$$

estimate where θ stands for the scattering angle between the e^- and the γ. Compton cameras suit well with the prompt-γ energy range, where Compton scattering is typically the most probable kind of interaction. Moreover, unlike collimator-based systems, Compton cameras provide 3-D information on the photon emission point. However, the instrumentation requirements in terms of spatial, time, and energy resolution for the detectors of a Compton camera are especially high, and the reconstruction algorithm is complex and computationally intensive, as the incident direction can not be recovered univocally for each event. At present, the only published experimental available results with proton beams refer to prompt-γ detection below 2 MeV or with beam currents far below the clinical case [67].

2.2.3 Time resolved cameras

A completely different method, which does not make use of collimators as well as Compton camera technique, consists in the estimate of the proton transit time in the target (Prompt Gamma Ray Timing). When a beam particle crosses through the matter, slows down until it stops, interacting with the target nuclei during its path inside the target. At beam energies used in PT, the time difference Δt between the entrance of the proton into the target and the arrival of the prompt-γ to the detector is measurable, being on the order of 1-2 ns for protons with a range of 5-20 cm. Δt is the sum of the proton transit time $t_p(z)$, defined as the time needed to

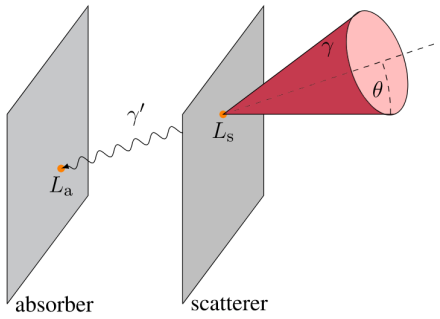

Figure 2.9. Concept of a typical Compton-camera. The incoming photon γ interacts in the scatterer layer, generating a photon γ' with lower energy, absorbed in the other layer. The two interaction points provide the γ' direction, and, while the θ angle given by the eq.2.1 define the cone surface containing all the possible directions of γ [67]

cover a z depth in the target, the γ decay time and the time needed by the photon to reach the detection. Applying the Continuous Slowing Down Approximation, i.e. assuming a stopping power without statistical fluctuations, $t_p(z)$ is provided by eq. 2.2 ([68]),

$$t_p(z) = \int_{z_0}^{z} \frac{1}{v(E)} dz' = \int_{E(z)}^{E_0} \frac{1}{v(E)\rho(z(E))S(E)} dE \tag{2.2}$$

where $v(E)$ is the proton velocity as a function of the kinetic energy E, ρ is the target density at z position, and $S(E)$ is the material stopping power. Thus, Δt can be correlated to the depth of interaction of the proton. The achievable precision of this technique is limited both by detector resolutions and the smearing effect due to the beam bunched structure, entailing the knowledge of the accelerator. With Prompt Gamma Ray Timing range shifts of 2 mm have been measures in homogeneous target within a few seconds data acquisition, assuming therapeutic proton beams and typical ranges [69].

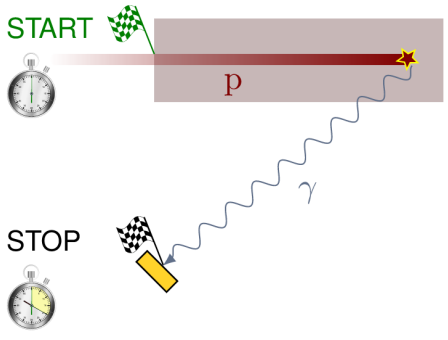

Figure 2.10. Concept of the Prompt Gamma Ray Imaging [67]. The time difference between the proton entrance in the target and the prompt-γ detection is correlated to the emission point

2.3 Charged fragments

As described in section 1.1.4, the target or projectile nuclei fragmentation results in the production of charged fragments of smaller charge. The target fragments are typically produced with very small velocities, so that they stop in micro-metre level ranges. Conversely, the projectile fragments velocity is close to the projectile initial velocity, resulting in longer ranges responsible of an additional amount of dose beyond the Bragg peak. To properly evaluate the fragmentation effect in a PT treatment, dedicated nuclear cross-section experiments [70, 71] and measurements of carbon ion collisions with water targets [72, 73] have been performed. As expected, the largest fraction of the fragments is forward peaked, and are mostly contained within a cone of few degrees with respect to the beam axis. However, the proton component shows not negligible tails at large emission angles. These results have triggered several studies on the possibility to exploit charged fragments for monitoring purposes. In fact, large angles production is the most interesting for monitoring applications, because of the advantageous proton reconstruction resolution (the uncertainty on the emission point reconstruction is proportional to $(sin\theta)^{-1}$, where θ is the proton emission angle). Moreover, protons are the most penetrating charged particles component, which is an important feature since they have to typically cross from 5 to 10 cm in order to exit from the patient. It is naturally expected that the charged particle yield at large angle remains relevant in the case of beams of particles heavier than protons. Therefore, the potential use of charged particle detection for the on-line monitoring of PT treatments can be especially appealing in ^{12}C therapy.

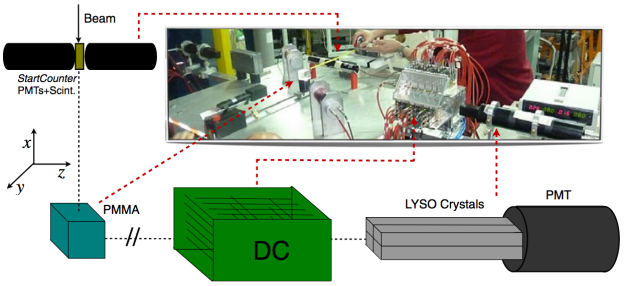

Figure 2.11. Schematic view of the experimental setup used at LNS.

In 2012 the 90° production of charged secondary particles in a $4\times4\times4$ cm^3 PMMA target impinged by a 80 MeV/u ^{12}C beam has been studied at LNS (Laboratori Nazionali del Sud, Catania, Italy) [74]. The experimental setup is shown in figure 2.11: a 12 plates drift chamber (DC) using a 80/20 $ArCO_2$ gas mixture has been used to track the secondary fragments exiting by the PMMA phantom, while a $1.5\times1.5\times12$ cm^3 LYSO crystals 2×2 matrix has been used to measure the fragment energies. In figure 2.12a the emission profile along the beam axis (x_{PMMA}), obtained back-tracing the detected fragment tracks. The expected dose deposited in the target, evaluated by means a Monte Carlo simulation, is superimposed. To demonstrate a relationship between the Bragg peak position and the mean x-position value of the distribution $\bar{x}_{\mathrm{PMMA}}$ of secondary particles emission point, a linear scan of the PMMA target along the beam direction was performed. In figure 2.12b both $\bar{x}_{\mathrm{PMMA}}$ and $\bar{y}_{\mathrm{PMMA}}$ (which is the coordinate of the proton emission point along the vertical

axis) as a function of the expected Bragg peak position x_{Bragg} are shown. A nice correlation was observed for $\bar{x}_{\mathrm{PMMA}}$, while $\bar{y}_{\mathrm{PMMA}}$ remains constant with respect to the BP abscissa, as expected. The overall resolution is $\sim 0.7\ mm$, representing a preliminary indication of the precision achievable in the BP determination using secondary protons.

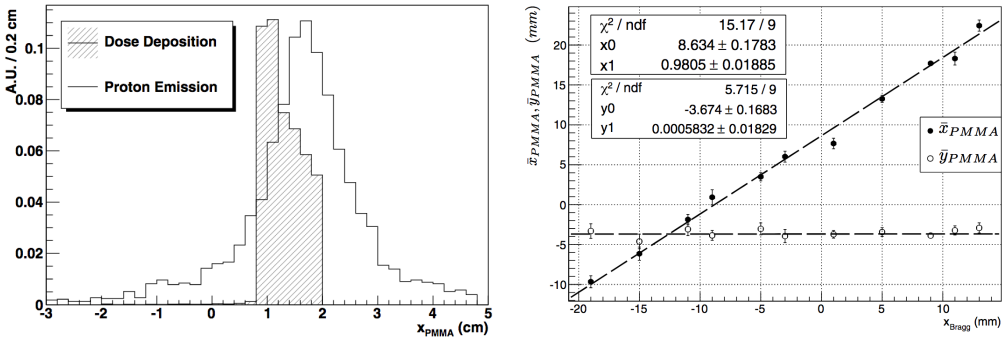

Figure 2.12. Left: secondary fragment measure emission shape. Right: Reconstructed peak position of the secondary proton emission distributionas a function of the expected Bragg peak position Bragg [74]

In 2014 the characterisation of the charged fragments exiting from a $5\times5\times20$ cm^3 PMMA target irradiated with a 220 MeV/u ^{12}C ion beam has been performed at GSI facility [75]. The fluxes per primary ion, the energy spectra and the emission profiles of the charged secondary fragments have been measured exploring two different emission angles, 90° and 60°. A 1.1 mm thick plastic scintillator (SC), acting as a start-counter, has been used to count the incoming primary ions. The aforementioned drift chamber (DC) and LYSO crystal have been used to reconstruct the fragment trajectories and kinetic energies, respectively. Finally, a $10.0 \times 10.0 \times 0.2$ cm^3 plastic scintillator (VETO) was placed between the target and the drift chamber to stop the electrons with energy below 0.55 MeV. The system was arranged as shown in figure 2.13. The results summarised hereafter are actually obtained from a re-analysis, published in 2017 [76], which takes into account the non-uniform LYSO matrix response.

The fragment identification has been performed using the correlation between the time-of-flight (ToF), defined as the time difference between the start-counter SC and the LYSO signals, and the energy released in the LYSO calorimeter E_{LYSO}. In the picture 2.14 the Charge vs TOF distributions are shown. Particle Identification has been performed using a Monte Carlo simulation in which the experimental setup was completely reproduced. For both the explored detection angles the largest fraction of the fragments results to be protons, with a small contamination of deuterons (5-10 %).

Protons were back-traced to the PMMA target with the DC. The reconstructed proton longitudinal emission profile is shown in figure 2.15a, superimposed with the expected dose released in the target. The falling-edge of the emitted proton spatial distribution is clearly linked to the Bragg peak position. The method proposed is to use an analytical function that parametrises the measured spectrum, as shown in figure 2.15b, to derive the Bragg peak position from the function parameters. The

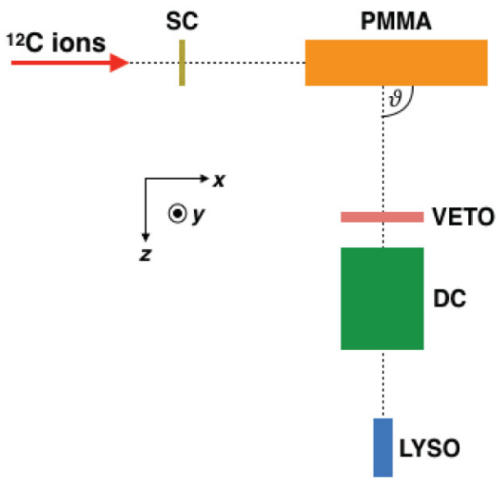

Figure 2.13. Experimental setup used at GSI for fragmentation products characterisation.

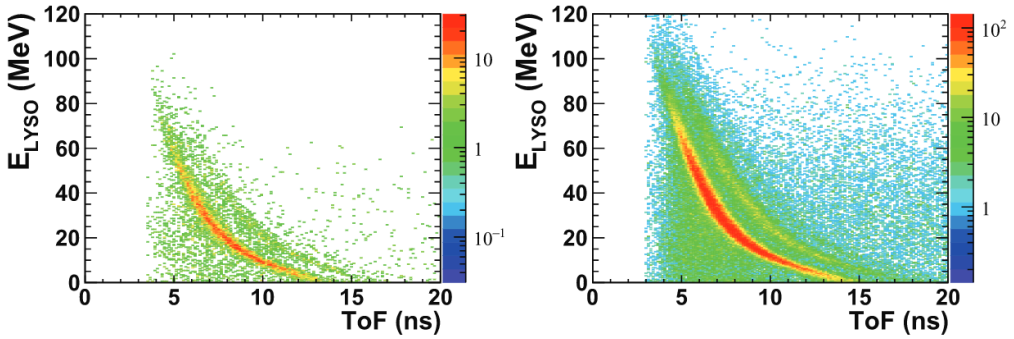

Figure 2.14. E_{LYSO} vs ToF, for proton emitted at 90° (left) and 60° (right) [76]

chosen mathematical model is a double Fermi-Dirac function, described by the eq. 2.3.

$$f(x) = p_0 \frac{1}{1 + e^{\frac{x-p1}{p2}}} \frac{1}{1 + e^{-\frac{x-p3}{p4}}} \tag{2.3}$$

From this model, four usefully quantities related to the Bragg peak position could be derived:

- X_{left} and X_{right}, defined as the x-positions in correspondence of the 40% of the rising and falling edge, respectively.
- Δ_{40}, defined as the difference between X_{left} and X_{right}, which could be associated to the beam range.
- δ_{40}, representing the distance between X_{left} and the x-intercept of the tangent to f(x) at $x = X_{right}$

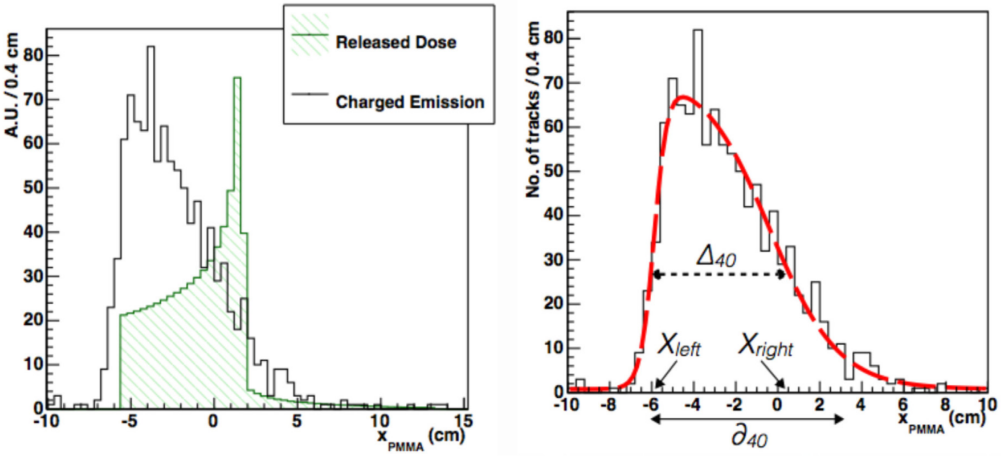

Figure 2.15. Left: longitudinal profile (solid line) of secondary charged particles as a function of the penetration in a PMMA phantom at 90° detection angle (beam entrance at 6.15 cm). Superimposed (hatched), it is shown the beam depth-dose distribution as from MC simulations [75]. Right: longitudinal profile (solid line) as above but with the f(x) function 2.3 superimposed [75].

The estimate of such parameters using a sample of 10^3 tracked charged fragments is provided in figure 2.16. The achieved accuracy is on the order of 3 mm. However, two main elements would influence the accuracy of the proposed methods in monitoring the Bragg peak position in a real treatment: the multiple scattering undergone by the fragments inside the body, and the collected sample statistics. Moreover, the emission shape is strongly affected by the target geometry, since materials with different thicknesses and densities could be crossed, then the Bragg peak correlation with the spatial distribution falling-edge is not straightforward. In chapter 4 a method to overcome this issue will be illustrated.

Angle (deg)	σ_Δ (cm)	σ_δ (cm)	$\sigma_{X_{left}}$ (cm)	$\overline{\Delta_{40}}$ (cm)	$\overline{\delta_{40}}$ (cm)
90	0.34	0.37	0.08	6.60	9.40
60	0.31	0.28	0.09	6.83	9.44

Figure 2.16. Standard deviation and mean values of the parameters used to describe the charged fragments emission distribution [75].

In figure 2.17 the detected $\beta = v/c$ spectra (red triangles) obtained from the ToF, for protons detected at 90° and 60°, normalised to the number of primary carbon ions, are shown. The old published one (black circles) is superimposed. The proton kinetic energy follows immediately transforming the β values with the eq. 2.4

$$E_{kin} = mc^2 \left(\frac{1}{\sqrt{1-\beta^2}} - 1 \right) \tag{2.4}$$

where m is the proton mass. For most of the protons β is in the range between 0.3 and 0.5, corresponding with a E_{kin} between 50 MeV and 150 MeV. At 60° the spectrum is slightly shifted towards higher energies, as expected.

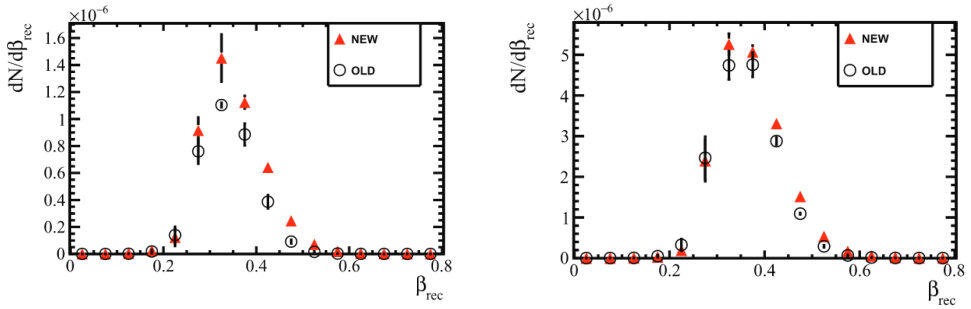

Figure 2.17. Proton detected velocity distributions (red triangles) in the angular configuration at 90° (left) and 60° (right). The comparison with the spectra published in [76] is superimposed (black circles).

The principal issue in using charged fragments as a Bragg peak position probe is the production statistics, that is lowered with increasing angles with respect to the beam incoming direction. The measured fluxes (ϕ_p) per incident primary beam particle (N_{ion}) per solid angle unit ($d\Omega$), defined in 2.5, are summarised in eq. 2.6. A factor ~ 2 between the two emission angle is found.

$$\phi_p = \frac{dN_p}{N_{ion} d\Omega} \tag{2.5}$$

$$\phi_p^{90^\circ} = (4.90 \pm 0.06_{\text{stat}} \pm 0.57_{\text{stat}}) \cdot 10^{-3} \text{sr}^{-1} \tag{2.6}$$
$$\phi_d^{90^\circ} = (0.70 \pm 0.02_{\text{stat}} \pm 0.12_{\text{stat}}) \cdot 10^{-3} \text{sr}^{-1} \tag{2.7}$$
$$\phi_p^{60^\circ} = (11.28 \pm 0.05_{\text{stat}} \pm 2.30_{\text{stat}}) \cdot 10^{-3} \text{sr}^{-1} \tag{2.8}$$
$$\phi_d^{60^\circ} = (2.15 \pm 0.02_{\text{stat}} \pm 0.44_{\text{stat}}) \cdot 10^{-3} \text{sr}^{-1} \tag{2.9}$$

In 2014 a data taking campaign at Heidelberg HIT facility has been performed with a GSI-like setup to extending the aforementioned measurements with different ^{12}C beam energies, as well as to explore non-conventional ions as ^{4}He and ^{16}O. The obtained results are currently in publication stage. The preliminary emission profiles obtained with ^{12}C beams at 220 MeV/u, 180 MeV/u, 160 MeV/u and 120 MeV/u, and with ^{4}He at 145 MeV/u, 125 MeV/u and 100 MeV/u are shown in figure 2.18. Different target setup has been implemented in the two cases. The target has been kept in a fixed position in carbon measurements, so that the distribution rising edge corresponds with the phantom entrance face. Instead the target has been moved for each different helium energy, keeping fixed the Bragg peak position in correspondence of $z = 0$.

In addiction, a very interesting measurement that points out working principle of charged fragments monitoring has been performed irradiating with 270 MeV/u Oxygen ion beam a non homogeneous PMMA phantom, in which 1 cm air gaps were

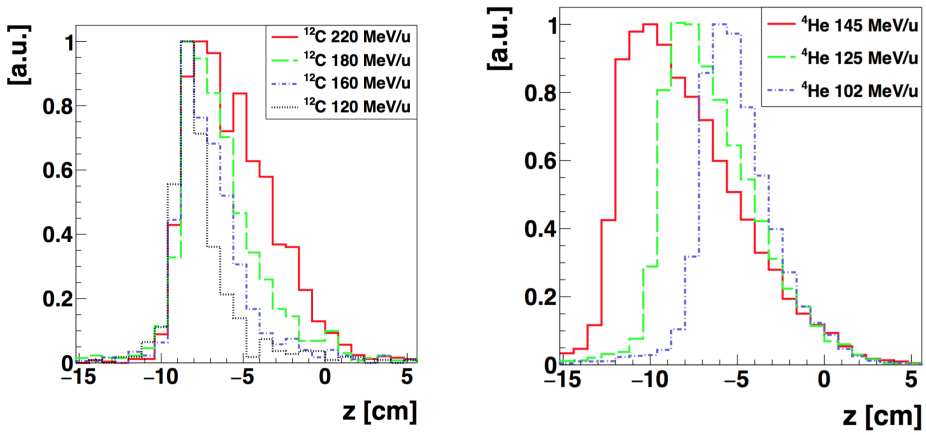

Figure 2.18. Emission shape for charged secondary fragments for different beam energies. Left picture: ^{12}C ion beam, 90°. Right picture: ^{4}He ion beam, 60°.

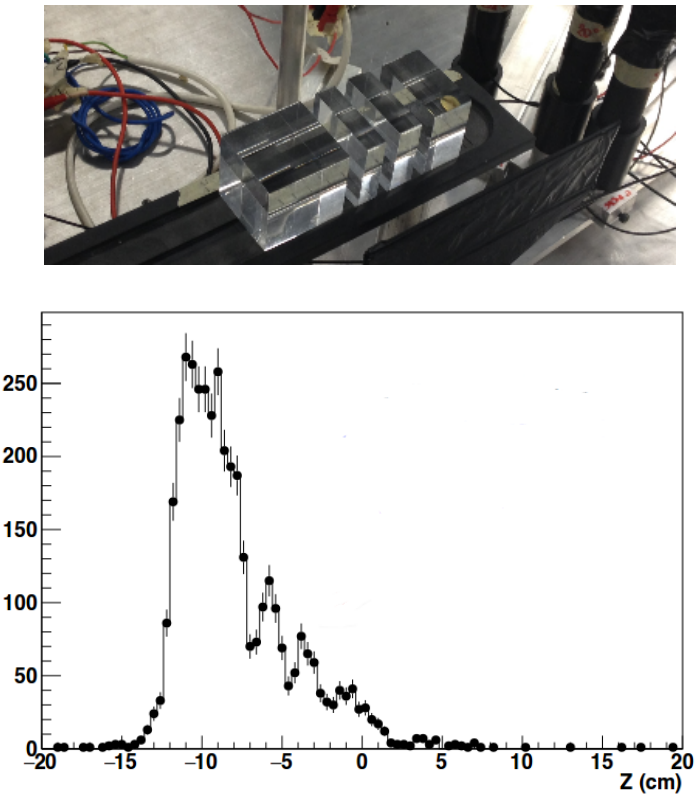

Figure 2.19. Top: non homogeneous phantom. Right: secondary protons emission spatial distribution obtained irradiating the non homogeneaous phantom with ^{16}O beam at 260 MeV/u.

used to recreate densities variations (figure 2.19a). Using a sample of $\sim$ 3000 events, the gaps are clearly visible in the reconstructed profile (figure 2.19b).

The measurements summarised in this chapter shows that the detection of the charged secondary particles emitted at large angles with respect to the beam direction

could be considered a valuable alternative for dose verification in PT, in particular for ^{12}C ion beam treatment due to the larger expected production. The impact of multiple scattering inside the patient on the Bragg peak position reconstruction could be reduced maximising the number of detected fragments. A charged particle detector suitable for clinical applications, designed to monitor the dose distribution during PT treatments, is presented in the following chapter.

Chapter 3

Dose Profiler development

Despite the good results obtained for proton beam range monitoring, ^{12}C ion treatments verification using prompt-γ or β^+ activity is still an issue, due to the low signal to noise ratio caused by the elevate neutron background. The charged fragment detection approach can overcome such limitations. The high detection efficiency and the very low background could balance the scarceness of charged particles production (compared to the neutrals). In this Ph.D. thesis the development of an innovative on-line beam verification technique that exploits charged secondary particles is investigated, and an innovative detector, named *Dose Profiler*, is proposed. The planned field of application of the technique is the on-line range monitoring in Carbon ion treatments, but the technique could be naturally extended also for other ions (^{4}He, ^{16}O) treatments, in which a not negligible secondaries production is expected.

In this chapter the Dose Profiler features are described, analysing in detail the design criteria. The detector is developed in the framework of the INSIDE (Innovative Solution for monitoring in Hadrontherapy) project, funded by MIUR, in order to work in a multimodal in-beam dose monitoring system able to detect at the same time the back-to-back photons from β^+ annihilation. The whole system is planned to be integrated in the treatment room of CNAO (Centro Nazionale di Adroterapia Oncologia), in Pavia (Italy), the Italian facility for proton and carbon ions therapy.

Figure 3.1. One of the three treatment rooms available at CNAO center.

3.1 Dose Profiler layout

The *Dose Profiler* is designed to measure the tracks of the charged secondary particles, in the energy range 50 - 150 MeV. The aim is to assess the beam range from the reconstructed spatial emission shape, achieved extrapolating the detected tracks towards the beam direction. The detector is also thought to measure the charged fragments kinetic energy, in order to potentially exclude the slowest fragments, that suffer of larger multiple scattering. The tracking system is based on scintillating fibres, allowing to have a greater ease of use and maintenance with respect to gas detectors, which is an important requirement for devices operating in clinical environment. Six planes (19.2×19.2 cm^2) of plastic scintillating fibres are used to reconstruct the tracks. Each fibre plane, fixed in an aluminium frame, is composed in by two adjacent layers of fibres arranged in orthogonal x-y directions (384 fibres per view). When charged particles traverse the planes, they deposit energy in the scintillating fibres creating scintillation photons. A small fraction of the scintillation light is then guided by total internal reflection to the fibre ends, where it is detected by Silicon PhotoMultipliers (SiPM). The fired fibres identify the coordinates of the interaction points, revealing the particle trajectory. Finally, the charged particles interact in two thicker plastic scintillator planes (19.2×19.2 cm^2). These additional layers, that constitute the so called *Absorber*, have the purpose to perform the incident particle kinetic energy measurement with an higher resolution with respect to what is possible to achieve with the fibres. To avoid to develop a dedicated read-out system, the Absorber planes are read-out by the same kind of SiPMs and front-end boards used for the fibres. The inter-plane distance is 2 cm, which corresponds to the minimum gap allowed by the front-end electronics, in order to maximise the detector angular acceptance and the compactness as well. The detector is enclosed in an light-tight box, composed by 4 aluminium panels arranged on the lateral surfaces, and a 50 μm Tedlar layer on the detector entrance surface, to avoid fragment energy loss.

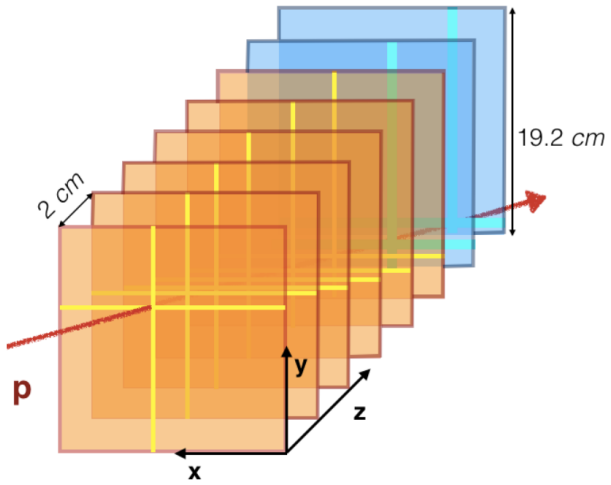

Figure 3.2. Schematic view of the Dose Profiler, illustrating the principle of working. The orange squares correspond to the fibres planes, while the light-blue ones to the absorber.

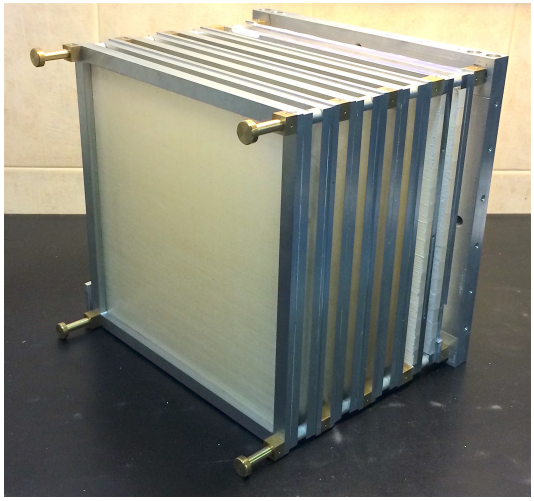

Figure 3.3. View of the Dose Profiler, before the front-end electronics assembling. The six fibres planes and the absorber can be distinguished.

3.1.1 Scintillating Fibres

Double cladding, squared $500 \times 500\ \mu m^2$ fibres (Saint-Gobain BFC-12 3.4) have been chosen as a result of Monte Carlo simulations, in order to achieve an optimal compromise between the total amount of scintillating material, that directly affects the reconstruction spatial resolution because of the multiple scattering, and the signal amplitude generated by the fibres. Each plane is built *weaving* the fibres around a rigid mechanical support, using glue for holding. Then two perpendicularly oriented layers are put in contact and are finally fixed in the aluminium skeleton. As it is evident from the figure 3.5, some dead space due to the glue is unavoidable.

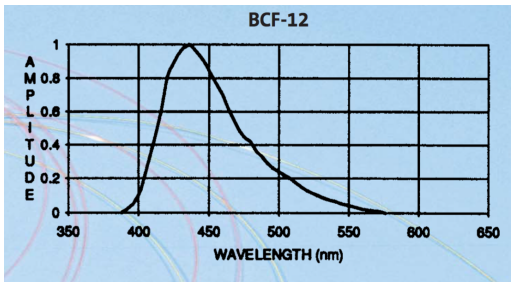

Material	Polystyrene
Cladding thickness	4%
Trapping efficiency	7.2%
Decay time	3.2 ns
Light yield	8000 ph/MeV
Emission peak	435 nm
Attenuation lenght	2.7 m

Figure 3.4. BCF-12 features: the light emission wavelength spectrum is reported on the left, while the main properties are listed in the right table.

3.1.2 Absorber

EJ-200 plastic scintillator ($Z_{eff} = 3.4$) is used for the absorber planes. Each layer has a thickness of 6 mm, corresponding with a total thickness of 2.4 cm crossed by the particles. Each plane is built with 16 scintillator bars ($19.2 \times 1.2 \times 0.6$ cm^3, shown in figure 3.6) placed side by side, and optically insulated each other by means

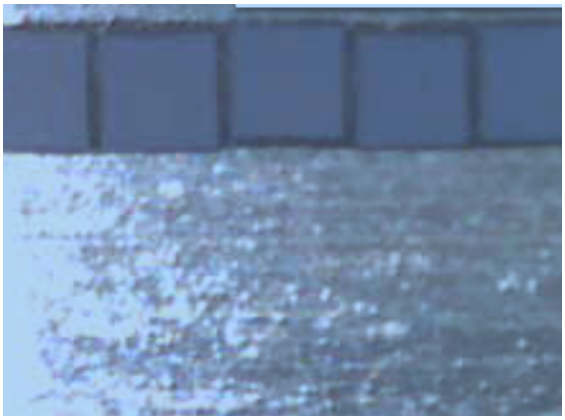

Figure 3.5. Blow-up view of the fibres exit face, evidencing the small but unavoidable dead space due to the building technique.

of TiO_2 paint spread on the lateral surfaces, for a more effective light collection by SiPMs.

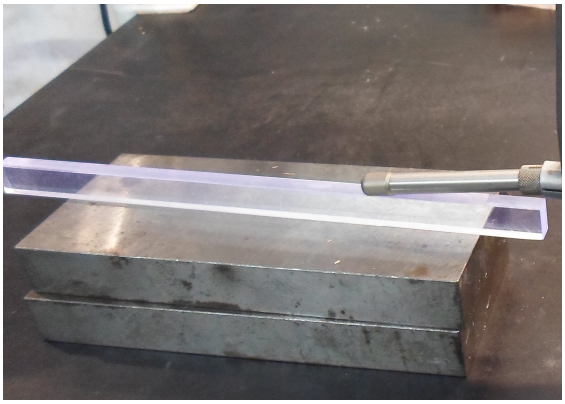

Figure 3.6. EJ-200 plastic scintillator bar, used to assemble the absorber planes. The picture has been taken during the polishing procedure.

3.1.3 Silicon PhotoMultipliers

The largest contribution to the beam range resolution achievable in practical applications is due to the multiple scattering that the charged secondary particles suffer crossing the patient tissues. For these reasons SiPMs (model S12571-050C by Hamamatsu) with a pitch of 1 mm^2 have been chosen for the fibres read-out, obtaining a spatial resolution of the order of $300\mu m$ (1 mm/ $\sqrt{12}$). With this read-out granularity, the overall resolution is not affected by the intrinsic detector spatial resolution, and at the same time this allows to limit the number of the electronic channels, resulting in a simplification of the front-end electronics design.

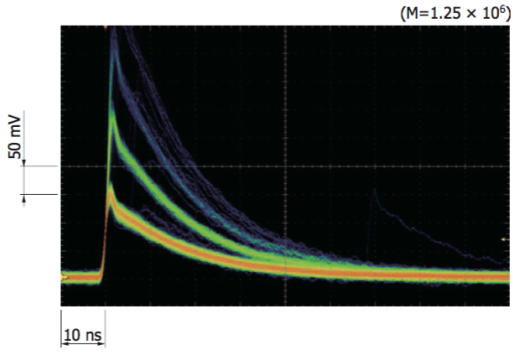

Breakdown Voltage	65 ± 10 V
Peak sensitivity length	450 nm
Quantum efficiency	$\sim 35\%$
Gain (at 25°C)	$1.25 \cdot 10^6$
Dark count rate	~ 100 kHz

Figure 3.7. Hamamatsu S12571-050C main features. In the left picture, a typical SiPM signal is shown. In the right table are summarised the main SiPM properties.

The expected number of photoelectrons $N_{ph.e.}$ produced by a SiPM when a fibre is crossed by a minimum ionising particle (MIP) is:

$$\begin{aligned} N_{ph.e.} &= \frac{dE}{dx} \cdot \Delta x \cdot \mathrm{LY} \cdot \varepsilon_{tr} \cdot \mathrm{QE} \simeq \\ &\simeq 2 \, \frac{MeV}{\mathrm{cm}} \cdot 0.05 \ \mathrm{cm} \cdot 8000 \, \frac{\mathrm{ph}}{MeV} \cdot 7.2\% \cdot 35\% \simeq 20 \end{aligned} \tag{3.1}$$

where dE/dx is the stopping power for a MIP inside polystyrene (data by PDG), Δx is the fibre size, LY is the BCF-12 light yield, ε_{tr} is the fibre trapping efficiency and QE is the expected SiPM efficiency. For proton in the aforementioned energy range, a number of photoelectrons between 3 and 7 times greater is expected. The SiPMs are situated in rectangular (21×4 cm^2) front-end boards, and are arranged in two parallel lines (96 SiPMs per line), as shown in the picture 3.8. Before the assembling, they have been sampled in order to form groups with similar nominal bias voltage (maximum difference 100 mV), assuring an inter-SiPM gain variation below 5% inside a single board. On the top side of the same front-end board, six 32 channel ASICs are welded for the SiPM signal processing.

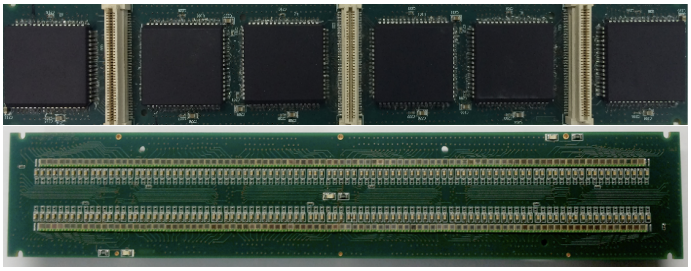

Figure 3.8. Front-end board with SiPMs (bottom view), and read-out ASICs (top view).

Each board performs the read-out of two adjacent fibres planes. A set of four board is needed to fully read-out two adjacent planes, defining the so called *double-plane*. This unit is at the base of the trigger generation, as it is carefully explained further on. The unavoidable dead space of 1 mm between neighbouring SiPMs, due to the sensor packaging, forces to use a couple of parallel boards placed at the

fibres extremities as illustrated in the figure 3.9. The boards geometry is specifically designed so that the fibres that are faced with the dead space in one board, are correctly faced with the SiPM active area on the board placed on the opposite side.

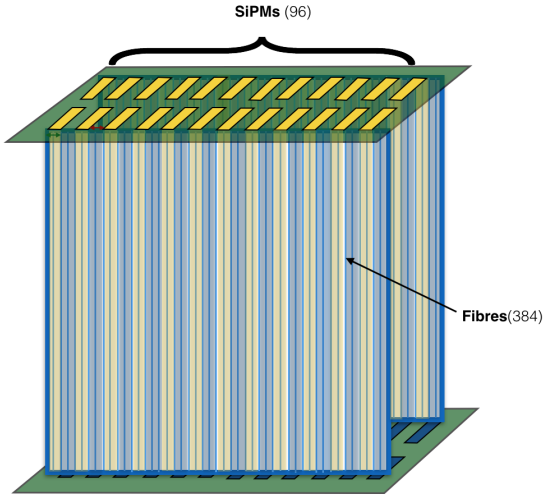

Figure 3.9. Schematic view of SiPM read-out. Due to the 1 mm dead-space between the SiPMs active area, the opposite boards are shifted by 1 mm in order to read-out all the fibres. In the picture, the top and bottom SiPMs read-out the fibres highlighted in yellow and blue, respectively.

16 boards are needed to cover the full detector, resulting in 3072 read-out total number of channels. All the boards are coupled with the fibres by means of a thin layer of optical grease, that completely fill the thin gap between the fibres exit face and the SiPM surface. A picture of the Dose Profiler after the front-end board assembly is shown in the figure 3.10.

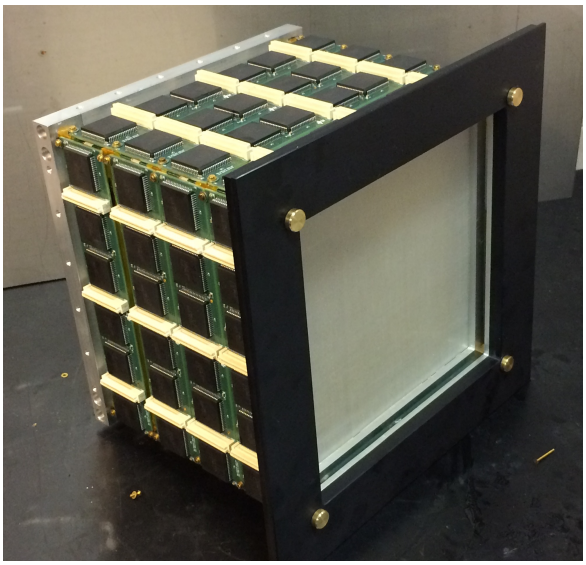

Figure 3.10. View of the Dose Profiler after the installation of the front-end boards.

3.2 Positioning

The placement of the Dose profiler in the CNAO treatment room aims to find a trade-off between the spatial resolution and the number of detected protons. For narrow detection angles with respect to the beam directions the mean kinetic energy of secondary charged fragments is higher, then the resolution worsening due to the multiple scattering is slightly reduced. On the other hand the resolution on the reconstructed secondary proton emission point worsen as a function of $sin\theta^{-1}$ (θ stands for the detection angle), then the resolution on the emission shape can be dominated by such geometrical effect. Furthermore the placement of a detector in a treatment room at angles $< 30°$ is usually challenging or often impossible, due to the geometrical constrains given by the dose delivery and patient positioning system encumbrance. From the above consideration it's clear that the choice of θ in operating conditions is crucial: on the basis of the measurements previously shown and the geometry of the CNAO treatment room, the optimal angle results to be of the order of $\theta \sim 60°$. The chosen distance from the patient is ~ 50 cm, to have a sufficient geometrical acceptance but at the same time preserving the patient comfort during the treatment. In the picture a schematic view of the CNAO treatment room and the planned position of the Dose Profiler, drawn in green, is shown.

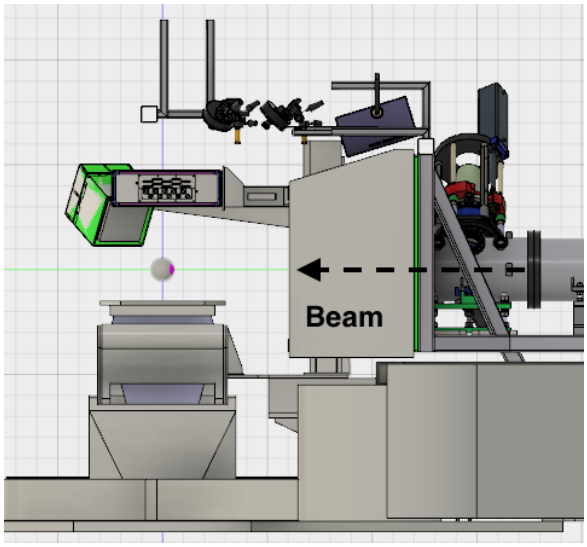

Figure 3.11. CAD view of the CNAO treatment room, with the Dose Profiler (highlighted in green) planned placement.

3.3 Read-out and DAQ system development

Considering the measured secondary proton fluxes in 2.3 at 90° and 60°, the order of magnitude of the expected secondary proton rates in the Dose Profiler field of view at therapeutical beam intensities ($\sim 10^7$ Hz) can be roughly estimated computing the solid angle $\Omega = A/r^2$, where $A = 19.2 \times 19.2$ cm^2 is the detector surface and $r = 50$ cm. It follows an expected rate of the order 5-15 kHz. Hence, the read-out system is designed to sustain a 20 kHz trigger rate. Electronics is organised following

a hierarchical architecture, as shown in figure 3.12: the SiPMs read-out is provided by a set of 96 ASICs, named *BASIC32_ADC*, installed on the 16 front-end boards, each one containing 6 ASICs. Such front-end boards are coupled in turn with a set of complementary boards, each one including a FPGA designate to manage the BASIC32_ADC configuration and read-out. Finally, a board named *Concentrator* is in charge to generate a trigger signal, to collect the data of all the FPGAs to build the event, and to supply the communication with an external DAQ machine through an ethernet link. During my Ph.D. I also designed the FPGAs using VHDL language, and I developed the software tools for the *Concentrator* and the external PC for the data acquisition, based on C/C++ libraries. In this section the read-out system main features are described.

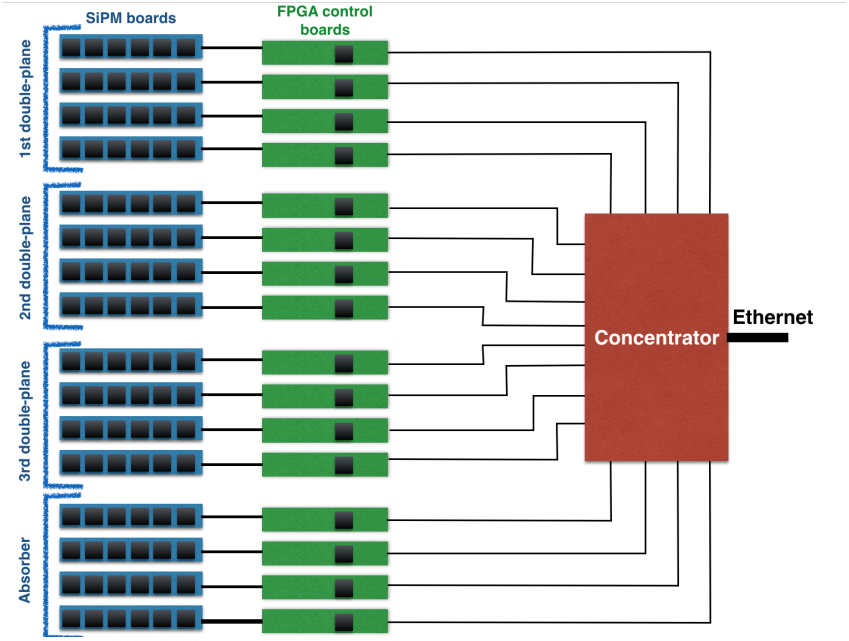

Figure 3.12. Schematic view of the read-out electronics: 16 SiPM boards are controlled by 16 FPGA boards, which are managed by the Concentrator.

3.3.1 BASIC32_ADC

The BASIC32_ADC (BASIC) is a self-triggering, 32-channel ASIC, designed in 0.35 μm standard CMOS technology, purposely developed to read-out Silicon Photo-Multiplier detectors in medical imaging applications [77]. The architecture of the front-end channel is based on a current mode approach, and is outlined in figure 3.13. The bias voltage of each SiPM can be tuned changing the input channels DC voltage level (*V_offset*) using a 12-bit DAC (dynamic of 1.0V). The current signal, scaled with a current buffer input stage, is sent to a Charge Sensitive Amplifier (CSA), that gives as output a voltage signal whose peak is proportional to the charge. The CSA gain can be varied setting a different feedback capacitance C_F, in the range (1 pF - 6 pF). The integration time $\tau_F = R_F C_F$ can be also tuned varying the feedback resistance R_F, that can be chosen between six different value too (33 $k\Omega$

- 200 $k\Omega$). A peak detector evaluates the peak value, and records the information in a storage capacitance. The output signal of the CSA is also sent to a voltage discriminator, with adjustable threshold. The 32 voltage discriminator outputs are OR-ed, generating an internal trigger signal which is also routed to an external pad, in order to be available to the user. The peak detector outputs of the 32 channels are sent to the input of an 8-bit ADC, which provide the charge digital conversion, via an analog multiplexer.

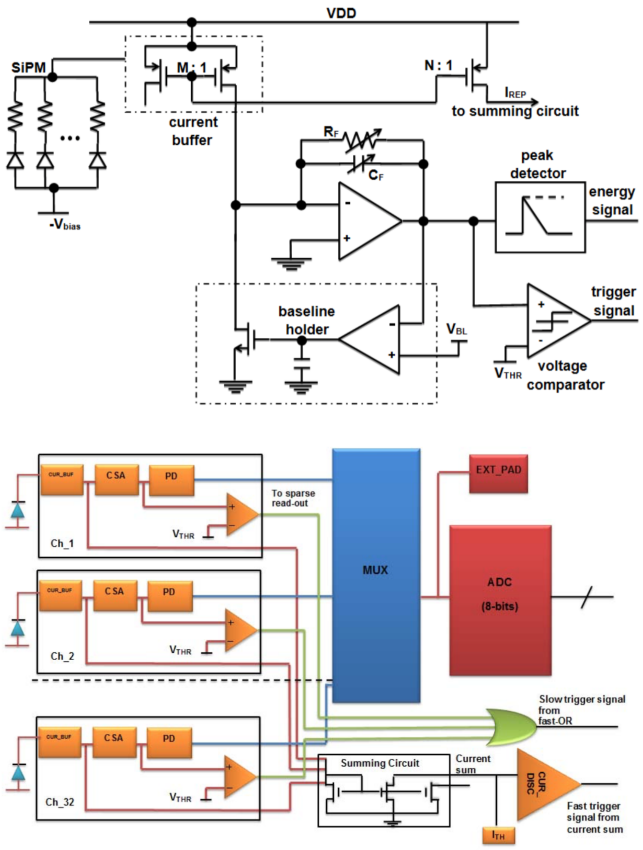

Figure 3.13. Top: Architecture of the BASIC32_ADC input channel. Bottom: Architecture of the analog part of BASIC32_ADC [77].

The chip read-out can be performed in two different modes, named *sparse* or *serial*. In the *sparse* mode only the channels that have gone over the set up thresholds are read-out, while in the *serial* mode all the channels are read-out independently from the discriminator outputs. The chip read-out can be launched by the internal trigger activation or by an external trigger. The procedures are the following:

- **Internal trigger:** As soon as the trigger is generated, two time windows of programmable duration, named TWA and TWB, are opened and a clock (maximum frequency 10 MHz) has to be sent to the ASIC. During TWA, all the channels that have gone over threshold are registered, so that when the *sparse* mode is activated only such channels are read-out. Therefore, the TWA duration is adjusted to minimise the probability that uncorrelated events can

be mixed in a single acquisition. After the expiration of TWA, no more trigger are accepted. The second time window, TWB, allow to delay the read-out procedure, which takes place only if an external coincidence signal (*coinc*) is be sent to the BASIC before the expiration of the TWB. It this does not occur, the ASIC is automatically reset and the read-out does not take place, i.e. the related event is ignored. After the expiration of TWB, two more clock cycles are needed for the ADC conversion. Finally, the channel address and the integrated charge are output on the respective pads of the chip at each clock rising edge. When all the channels are read-out, the chip is automatically reset, becoming ready for a new trigger.

- **External trigger:** In this case the read-out operations start when an external trigger is provided to the chip, independently of what happens to the internal trigger. The external trigger signal, sent as input to the *coinc* pad, forces the read-out, hence TWA and TWB are opened and the process follows the same procedure described above.

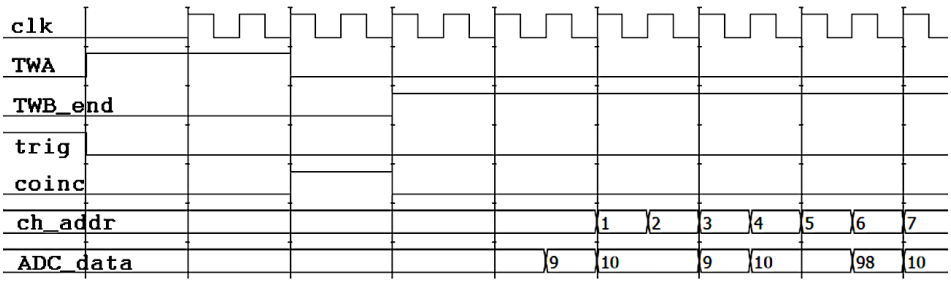

Figure 3.14. Read-out procedure of the BASIC32_ADC.

The BASIC contains two register needed to store the configuration. The first one contains the global configurations, common to each channel, as discriminator thresholds, read-out and trigger modes. Instead, the aim of the second one is to store the settings for C_F, R_F, and V_offset, which are configurable for each single channel. The 524 bit configuration is sent to the chip using a serial protocol, through 4 lines. All the main signals used to manage the BASIC are summarised in table 3.1.

150 BASICs have been carefully tested before the board assembly, to check their main functionalities. I developed a dedicated test-stand based on a test-board, designed by the Milan INFN electronics service (figure 3.15), controlled by a CAEN module V1495, a customisable FPGA unit controlled via VME bus. The best 96 basic have been selected according the test results, in order to be assembled on the SiPM boards.

Name	Description	Direction
CLK	Master clock	Input
TRIG	internal trigger	Output
BFC	Data valid	Output
COINC	Coincidence, ext trigger	Input
ADDRESS[4:0]	Channel address	Output
DATA[7:0]	ADC Data out	Output
SDI	Input SPI interface	Input
SDO	Output SPI interface	Output
SSN	Ctrl SPI interface	Input
RESET	Reset signal	Input

Table 3.1. Digital signals for the control of the BASIC32_ADC.

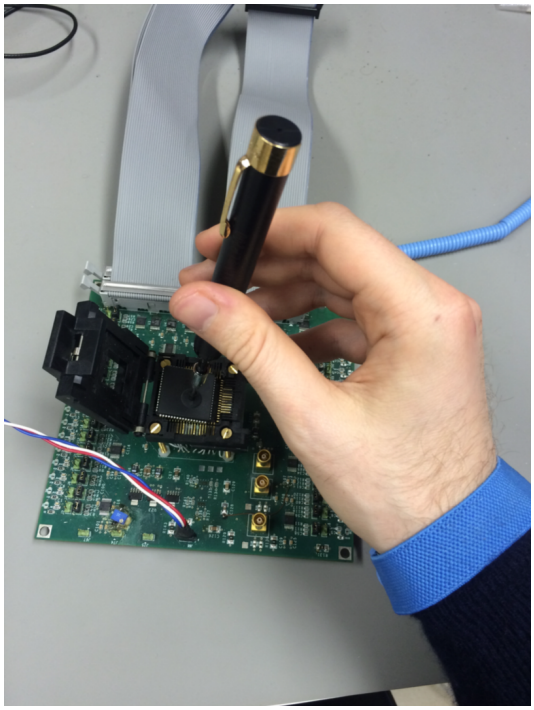

Figure 3.15. Board used to test the BASICs, housed in the specific location with the aid of a vacuum pick-up pen.

3.3.2 FPGA boards

Each front-end board, which includes 6 BASIC32_ADC, is paired with a control board, shown in figure 3.16, containing two main components: an FPGA, and a removable module for SiPM power supply. It also include a temperature sensor, placed on the board top side, capable to measure the local temperature with a 3° accuracy.

SiPM power supply The SiPM Power supply is provided by a DC-DC converter. The output voltage can be tuned setting a 12-bit DAC, configurable via SPI. The

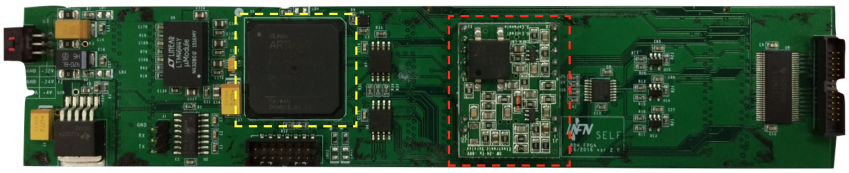

Figure 3.16. FPGA board. The yellow square highlight the FPGA, while the red one point out the module for SiPM power supply.

DAC generate a low voltage level between 0V and 2.5 V, corresponding to an output bias voltage between -70 V and -60 V. The voltage supply can be enabled or disabled setting respectively at low or high the status of a specific signal, driven by the FPGA. The effective voltage supplied by the module can be monitored using a 12-bit ADC.

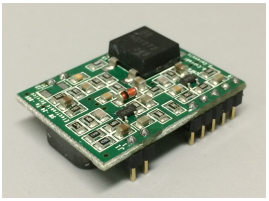

Figure 3.17. Module for SiPM voltage supply.

FPGAs design The FPGA assignments are basically to sent the configuration bit stream to the BASICs and to perform the data read-out. The chosen model is the *Artix7* XC7A50T by Xilinx. The firmware has been designed with the Xilinx Tool *Vivado 16.2*, using the VHDL language. A simple scheme that summarise the firmware functionality is shown in figure 3.18.

The communication with the BASIC is shown on the left side of the scheme, while the communication with the Concentrator, provided by 12 lines, is sketched on the right side. The logic or of the 6 basic internal trigger (OR_TRIG) and of the data valid signals (OR_BUSY) are output by the FPGA towards the Concentrator, respectively for the global trigger signal generation and to manage the read-out procedure operated by the Concentrator.

The core of the firmware is formed by a set of control register, two RAM blocks, and six FIFO buffers. A SPI interface (driven by the MISO, MOSI, SCLK, CS signals coming from the Concentrator) allows to have the reading/writing access by the Concentrator to the registers and to the RAM block. The first RAM block is used to store the configuration words that have to be input to the BASICs. The configuration procedure is triggered by a writing cycle in the dedicated register: this activate a finite state machine (FSM) that manages the configuration process, reading the configuration word stored in the RAM, and sending it bit by bit to the ASICs. The configuration is sent twice, and the output configuration, resulting from the BASIC internal shift registers, is registered in the second RAM block. In this way it is possible to perform a validity check of the actually sent configuration, comparing the values wrote in the two RAM blocks.

The six 16-bit wide, 32 deep, FIFO buffers (one per BASIC) are used to store

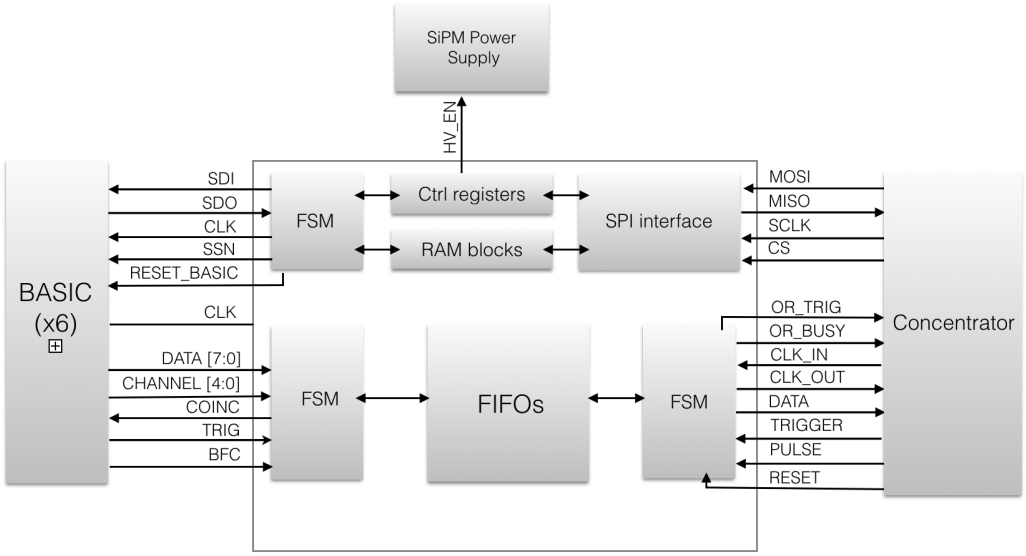

Figure 3.18. Block diagram view of the FPGA design.

the output data. A finite state machine, activated by the trigger sent by the Concentrator, manage BASICs read-out and the FIFO writing process. As soon the trigger arrives, a COINC signal is sent to the BASIC to enable the read-out procedure, and a BUSY signal is sent to the Concentrator, remaining active until the read-out is completed. The data are organised in 16-bit word as outlined in the figure 3.2. The eight last significative bits contain the charge information, preceded by the channel number (five bits). The three more significative bits flag which is the BASIC of origin.

[15:13]	[12:8]	[7:0]
Basic number	Address	Charge

Table 3.2. .

As soon the read-out procedure is completed, the BUSY signal expires and the Concentrator starts to read the FIFOs content. The BASIC read-out and the FIFO writing processes are shown in the figure 3.19, as a result of the design simulation performed with the Vivado tool.

The BASICs are read-out in parallel, then the time needed to read-out a single board is dominated by the BASIC with the highest number of channels over threshold. A very conservative estimate of the read-out time can be done considering an event in which all the channels go beyond the threshold. In this case 32 clock cycles are needed. The duration of TWB, set to 4 clock cycles, and the conversion time needed to the internal ADC (2 clock cycles) have to be added, giving as a result $\sim 4\ \mu s$.

Each FPGA board is coupled with the complementary BASIC-board. In figure 3.20 you can see the Dose Profiler immediately after the board assembly.

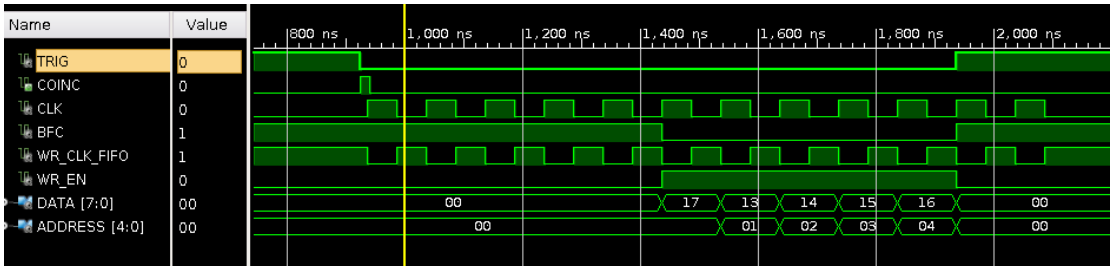

Figure 3.19. BASIC read-out procedure, simulated with the Xilinx Vivado tool.

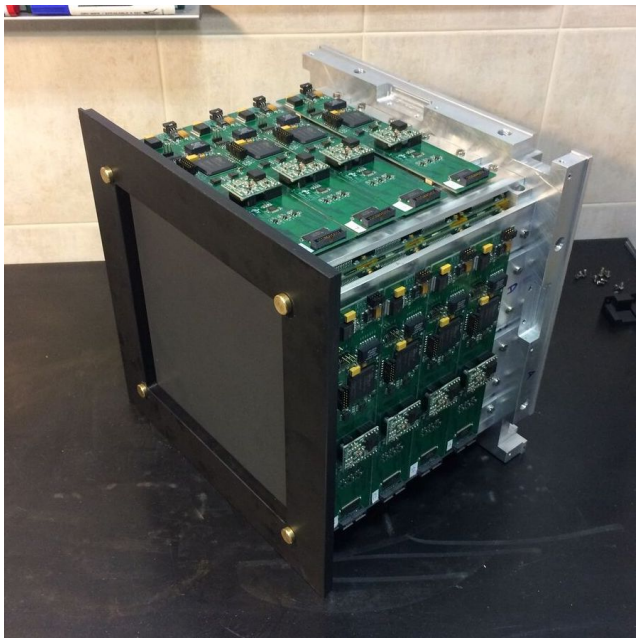

Figure 3.20. Dose Profiler view after the FPGA board assembly.

3.3.3 Concentrator

The Concentrator is located on the bottom side of the Dose Profiler, behind the last plane of the absorber. The 16 FPGA boards are connected by means of twisted cables ~ 25 cm long to the Concentrator board, shown in figure 3.21. Each side of the board hosts 5 connectors, 4 wired, one spare. The core of the board is constituted by an embedded system based on the *PicoZed*, a commercial System-On-Module (SOM) that is based on the Xilinx Zynq-7000 All Programmable SoC (System-On -Chip). It provides the access to over 100 user I/O pins through three I/O connectors on the backside of the module. It includes an Ethernet interface, USB, and 1GB RAM block. Moreover, the Concentrator provides all the necessary low voltage supplies for the FPGA and BASIC power source.

Trigger The charged secondary fragments trigger is generated on the base of the 16 OR_TRIG signals coming from the FPGAs. The trigger logic is fully configurable, and can be changed before each data acquisition according to the necessity. The signals belonging to the same *double-plane* (defined in the section 3.1.3), two for

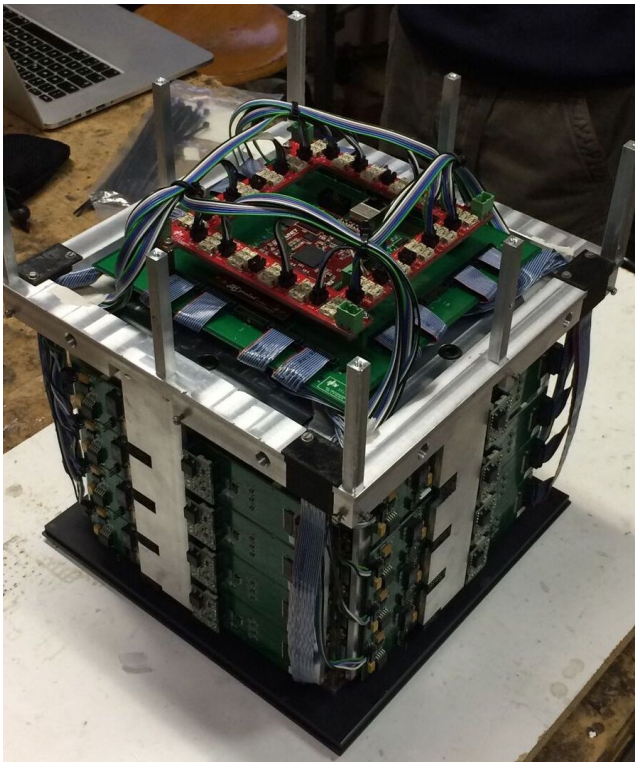

Figure 3.21. Picture of the back-side of the Dose Profiler, where the Concentrator board is placed.

the x-view and two for the y-view, are input to 4-input Look-Up Tables (LUT), embedded in the Zynq device. The design scheme is shown in figure 3.22. The LUTs can be programmed with few writing cycles in the Zynq control registers. The input addresses correspond exactly to the logic state of the OR_TRIGs, and the corresponding outputs can be conveniently defined according the chosen kind of trigger logic. The outputs of these LUTs are sent as input to a final LUT, which is in charge to generate the global trigger, with the same criteria. This signal is used to start the acquisition flow. Notice that the OR_TRIG signals are gated in a 50 ns width, in order to avoid the generation of random coincidences.

Furthermore, other two kind of trigger are available for different purposes. An external trigger can be given using a specific pin of the board, and an internally generated random trigger, given by a square wave with adjustable frequency in the range (1 Hz - 50 kHz), can be also used (for instance to measure pedestals).

Data collection The trigger transmission activates the BASIC read-out by the FPGA, which save data in a set of FIFO buffers. As soon as all the OR_BUSY signals expire, indicating that the BASIC read-out is completed, the FPGA read-out procedure starts. The data are transmitted towards the Concentrator with a serial protocol, defined as follows: a 100MHz clock is sent in parallel from the Concentrator to all FPGAs (CLK_IN line). The words coming from the FPGAs are serialised, and each bit is available on the DATA line at each rising edge of the clock. The Concentrator deserialises the received bits and, when the word is totally

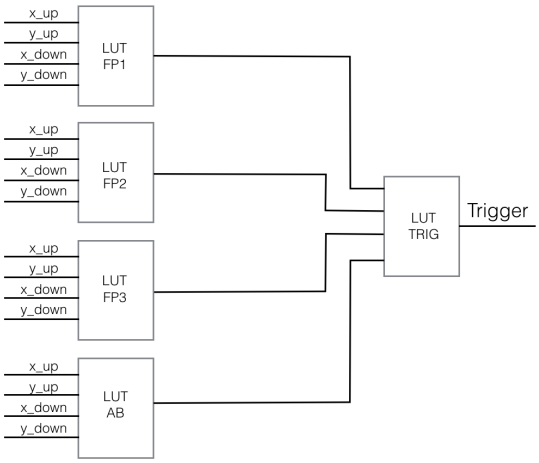

Figure 3.22. Schematic view of the trigger unit.

reconstructed, a further 8-bit flag that indicates the board number is appended to the data, building a 32-bit word (the 8 residual bits are not used). Each word is again saved in a 32-bit wide, 256 deep FIFO buffer (one FIFO per board). Until the end of the data transmission, a data valid signal (CLK_OUT) is sent from the FPGA to the Concentrator. When the last bit has been sent, the CLK_OUT signal expires and the Concentrator clock stops. The aforementioned process is in figure 3.23.

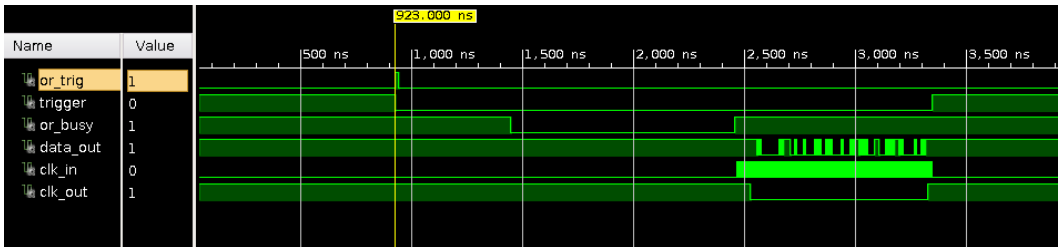

Figure 3.23. FPGA data read-out process, simulated with the Xilinx tool Vivado. As soon as the BASIC internal trigger is activated (OR_TRIG), the Concentrator send the trigger that enables the BASIC read-out procedure. The OR_BUSY signal remains active until all BASICa have download their data. When the busy signal has expired, the FPGA starts to sent the collected data to the Concentrator, according the CLK_IN and CLK_OUT signals.

At this point the event is built, joining all the available information: a 32-bit header is the first word that marks the beginning of the event; it is followed by the event number, that is simply given by a counter reset at each new data acquisition. Than three word with the event supplementary information are added in the event stack, namely the trigger mask information, the event time difference and the dead time of the previous event. Finally the event is filled with the data registered in each FIFO, and a final footer. The full event is wrote on the PicoZed RAM though DMA (Direct memory Access), in order to allow the accessibility to the data by means of the PicoZed software tools. As a last step, the event is transmitted to the

external PC, linked with 1Gb/s Ethernet connection.

3.3.4 Software tools

The communication between the Concentrator and the external DAQ PC is provided by an Ethernet link, using the TCP-IP protocol. Two software applications are needed for the data-acquisition. The first application is developed in C language, and it runs in the Picozed, providing the tcp-ip implementation by means of an open source *lwIP* TCP-IP stack [78]. When the power is turned on, the application is automatically launched, opening a communication channel with the PC in listening mode, in which the system is continuously waiting for a message. The second software applications run on the DAQ PC, and has been developed in C++ using the ROOT libraries. It provides the TCP-IP communication with the Dose Profiler by means the opening of a socket, and it acts as interface between the external user and the Dose Profiler. The CERN software framework includes classes for the development of GUI, that allows to easily manage the configuration parameters, and also for the TCP-IP socket implementation. The developed program is organised in three windows, shown in figures 3.24, 3.25, 3.26, that are opened when the program is launched, allowing to:

- Set the threshold for the BASIC internal discriminators.
- Set the C_F and R_F of the charge sensitive amplifier, to adjust the gain and integration time constant.
- Set the duration of TWA and TWB.
- Adjust the *V_offset*, for the SiPM gain fine tuning.
- Set the BASIC readout modality (sparse or serial).
- Set the kind of trigger and, if the internal trigger is chosen, the trigger logic with the procedure described in 3.3.3.
- Set and monitor the SiPM voltage, by means a dedicated monitor panel
- Monitor the environmental temperature.
- Launch the acquisition, setting the required number of events and the file name that is created for the data saving. It is possible to on-line check the daq rate in a dedicated monitor that refresh every 30 seconds.

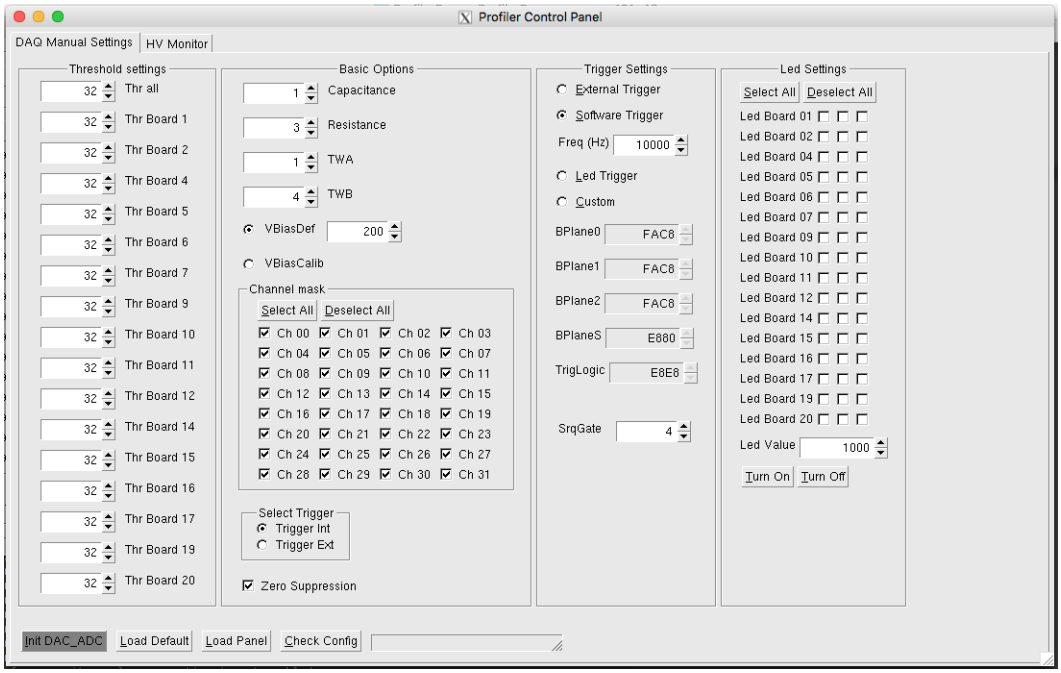

Figure 3.24. View of the configuration panel.

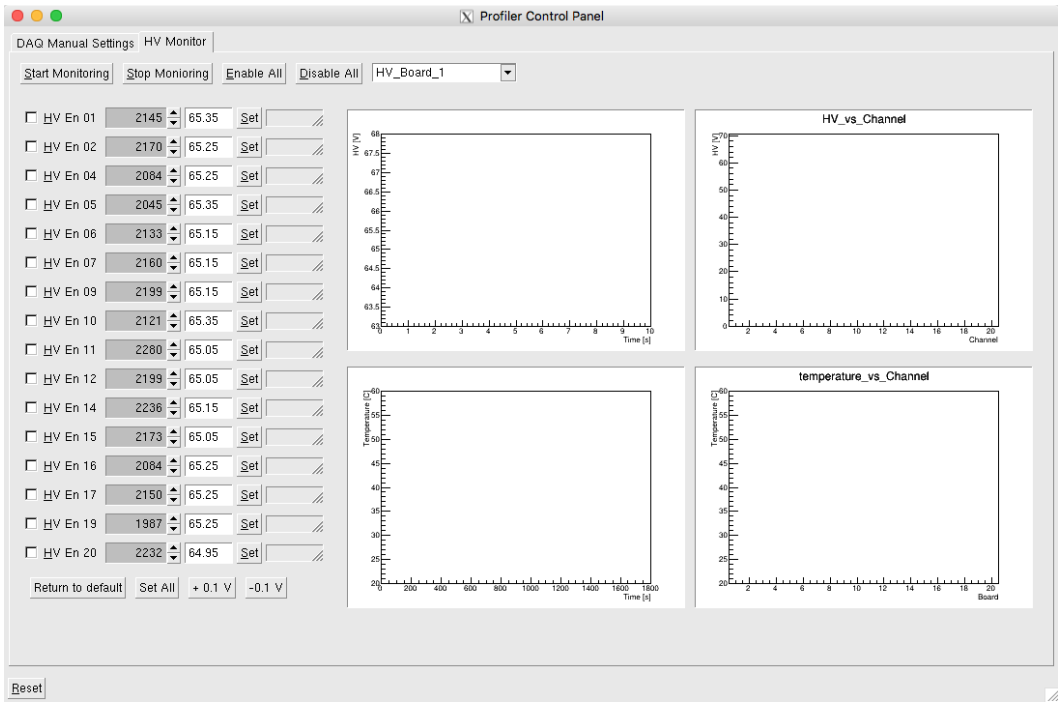

Figure 3.25. HV and temperature monitoring panel.

3.4 Cooling system

The overall power dissipated by the full read-out electronics system is on the order of 100 W, distributed as follows: $\sim 50\ W$ for BASIC_32 low voltage supply, $\sim 40\ W$

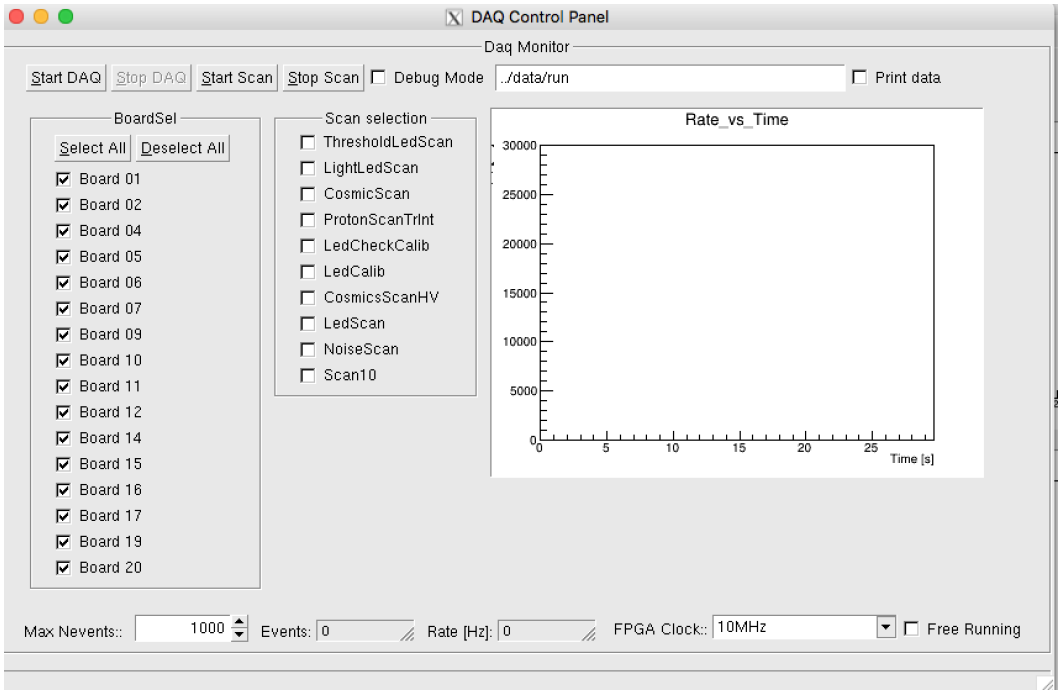

Figure 3.26. Data acquisition panel.

for FPGA and Concentrator and $\sim 10\ W$ for SiPM voltage supply. The detector is inevitably enclosed by a light-tight box, then the air circulation is limited. A water-cooling system has been thought to preserve a temperature close to the environment one. Aluminium rods 6 mm thick, having different surface sizes, are put in thermal contact with each heat source (ASICs, FPGAs) by means of a thin thermal grease layer. Despite the copper has twice the thermal conductivity then aluminium, the latter has been chosen to minimise the total detector weight ($\rho_{Cu} \simeq 3\rho_{Al}$), allowing a simplification in the design of the Dose Profiler support mechanical structure. The rods extremities are fixed to a bigger aluminium plate ($4 \times 21 \times 21\ \mathrm{cm}^3$) placed on the back side of the detector, acting as a cold mass. The water-cooling is provided by a chiller, capable to refrigerate and pump water in a closed circuit, in which water flows in a cooling coil that is put on thermal contact with the back-side aluminium mass. In figure 3.27 a view of the aluminium rods that constitutes the core of the cooling system is shown.

The temperature internally measured, setting the cooling water at 12°, are reported in figure 3.28. The large temperature spread is due to the low sensor precision as well as the temperature non-uniformity: the boards closest to the cold mass have clearly a lower temperature than the furthermost ones. However, the temperature varies from 25 °C up to 34 °C. It is not possible to reduce the temperature more, due to condensation on the detector that occurs due to the temperature gradient with the environment, typically at 20-25 °C.

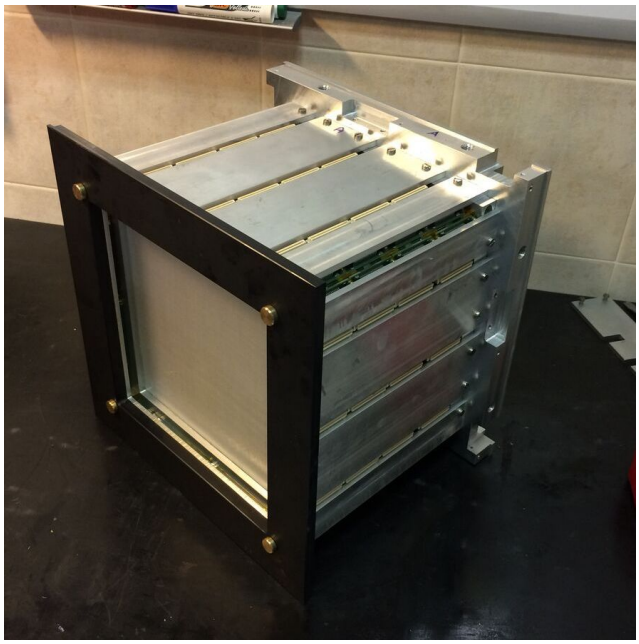

Figure 3.27. Aluminum rods used to dissipate the front-end electronics heat.

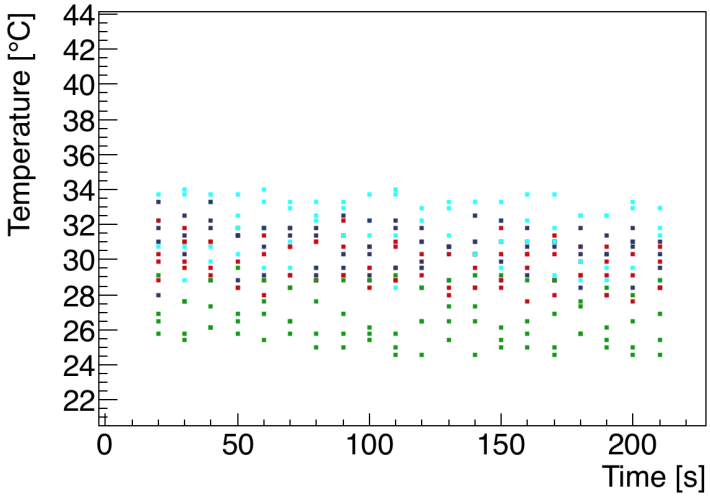

Figure 3.28. Temperature as a function of the time. The cooling water temperature was set to 12 °C.

Chapter 4

Bragg peak reconstruction

The charged secondary particles emission profile along the beam axis is reconstructed back-tracing the tracks measured inside the Dose Profiler to determine the production point inside the patient. The Bragg peak retrieving method described in section 2.3 can not be applied straight in a real treatment, since the fraction of the fragments stopping in the patient derives from the tumour depth inside the patient and from the crossed organs density. As a consequence, the measured emission shape depends on the treatment topology, and a technique to bring it back to a reference scenario, in which the Bragg peak correlation is known from experimental measurements, is needed. In this chapter the flow of operations that leads to the Bragg peak position extrapolation starting from the raw data is examined. In this chapter the emission profile reconstruction method is described and a method, that allows to unfold the distortion effect on the emission profile due to the tissues absorption, is proposed. Its application in a realistic case, investigated with a Monte Carlo simulation developed with the FLUKA software, is discussed.

4.1 Emission shape reconstruction

The passage of a proton inside the Dose Profiler active volume is identified by the fibres light emission, detected by the SiPMs. A preliminary version of the reconstruction code has been developed in C++ languages, using the ROOT libraries. The Dose Profiler geometry has been implemented in the code using the ROOT *Geometry* package, providing a bijective map between the SiPM read-out addresses and their position in the detector local reference frame. The detector representation is shown in figure 4.1. A proton track is searched looking at the SiPMs with a signal over a certain threshold, defined as *hits*. When a proton crosses a fibre, the light can be collected by more than one SiPM, because of the potential cross-talk between neighbour fibres or just due to the arrangement of the SiPM (a single SiPM does not exactly match with two whole fibres). For this reason the consecutive hits in the separate x-y view are grouped in 2-dimension *Clusters*, assigning the arithmetic mean of the hits positions to each built cluster. Given a list of clusters in the two views, a track finder algorithm is launched to search for possible track candidates. Noise clusters can be present due to the SiPMs dark counts. In any case, the expected average number of noise hits (N_{noise}) per event is small. The SiPM Dark Count

Rate $DCR_{0.5}$, i.e. the dark pulses rate measured with a 0.5 photoelectrons threshold, is $\sim$ 100 kHz, while the the cross-talk probability is $\sim$ 20%. Since the $DCR_{1.5}$ is essentially due to the optical cross-talk, then $DCR_{1.5} \simeq 20$ kHz. The number of expected noise hits in the Dose Profiler with a 2 photoelectrons threshold $N^{2p.e}_{\text{noise}}$ can be estimated using the eq. 4.1,

$$N^{2p.e}_{\text{noise}} \simeq (DCR_{1.5} \cdot 100 \text{ ns} \cdot N_{\text{ch}}) \simeq 6 \tag{4.1}$$

where N_{ch} is the number of electronics channels (3072), and 100 ns is the coincidence time window. This means that even with a very low threshold of 2 p.e., the expected noise due to the SiPMs dark current is negligible.

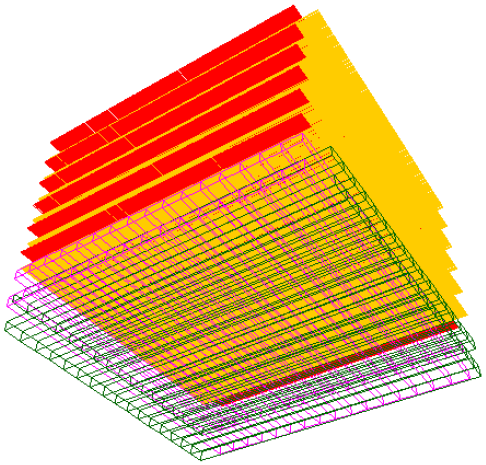

Figure 4.1. Implemented design of the Dose Profiler in the reconstruction code. The red and yellow strips represents the fibres, while the green and purple rods correspond to the absorber.

4.1.1 Track identification: Hough transform

The track-finder is based on the *Hough transform* application to find points aligned on a straight line. The Hough transform is a pattern-recognition algorithm typically used in image processing, initially conceived to find straight lines in images, but later extended to different kind of shapes. It was patented by Paul Hough in 1962 [79], but the algorithm as it is commonly used today has been introduced by R.Duda and P. Hart in 1972 [80]. A straight line in the cartesian space, parametrised as $y = mx + b$, is represented by a point in the parameters space (also named *Hough space*), while a single point is associated to a straight line, as shown in figure 4.2. Hence, a series of N aligned clusters in the cartesian space corresponds with a N-lines sheaf converging in a common point. Thus, using quantised values of (m,q), all the lines allowed by the detector geometry are evaluated and saved for each cluster. If a (m,q) couple is counted at least 4 times, meaning that at least 4 clusters are aligned within the precision determined by the parameters quantisation, a track is identified.

In figure 4.3(a) a 6-clusters track example, given by the passage of a muon inside the Dose Profiler, is shown. The event display shows a 2-D outlined view of the detector. The vertically arranged orange and blue rectangles represent the fibre planes and the absorber, respectively, while the red stars are associated to the clusters reconstructed in the event. The view of the same event in the Hough space (figure 4.3(b)) exhibits an accumulation point populated by 6 counts, corresponding with the 6 aligned clusters. The slope discretisation step Δm is 0.025 mm^{-1}, corresponding to the minimum angle allowed by the inter-planes gap (2 cm) and the inter-fibres distance (0.5 mm). The intercept step size is fixed by the slope quantisation, corresponding with $(\Delta m \cdot L) = 2$ mm, where L is the distance between the first and the last fibre layer (10 cm).

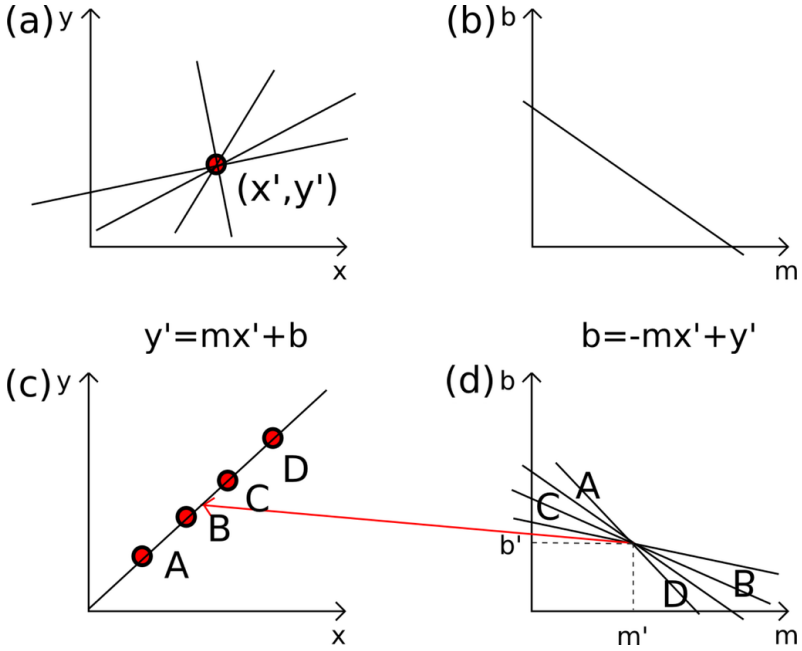

Figure 4.2. Principles of working of the Hough transform algorithm. A line sheaf intercepting in the x',y' point (a), is associated to a straight line in the *Hough* space (b). Then, 4 aligned point in the cartesian space (c) correspond to a line sheaf centred in a point.

4.1.2 Track parameter extraction: Kalman filter

The track parameters are calculated with two different methods: (1) a fit with a straight line minimising the χ^2, (2) applying the Kalman filter, since at low energies ($E < 50$ MeV) the multiple scattering in the fibres has to be taken into account to better reconstruct the true proton direction. The extended Kalman filter is a general recursive algorithm that finds the optimum estimate $\underline{\hat{x}_k}$ of a system that undergo noisy measurements, together with the corresponding covariance matrix C_k [81]. In our case $\underline{x}_k$ corresponds with the track parameters at the k-th fibre plane. In the Kalman algorithm the evolution of the state of $\underline{x}$ can be described by the equations system 4.2

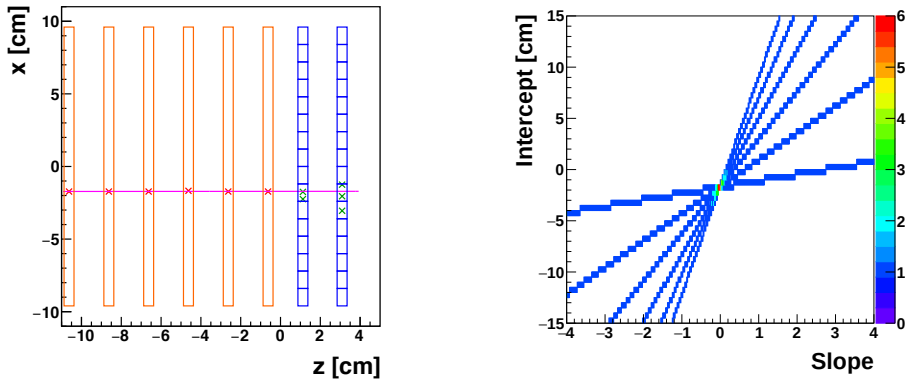

(a) (b)

Figure 4.3. Reconstructed clusters generated by a cosmic ray passage inside the Dose Profiler (a), and respective representation in the Hough space (b).

$$\underline{x}_k = f_{k-1}(\underline{x}_{k-1}) + \underline{w}_{k-1} \tag{4.2}$$

where $f_{k-1}(\underline{x}_{k-1})$ is a function that describes the propagation from the (k-1)th to the k-th, and $\underline{w}_{k-1}$ parametrises all the noise sources (multiple scattering, fluctuation of energy losses). $Q_k = \langle \underline{w}_k \underline{w}_k^T \rangle$ defines the noise covariance matrix. However, $\underline{x}_k$ is not directly measured, but the known experimental measurements $\underline{m}_k$ are related to the $\underline{x}_k$ according the eq. 4.3

$$\underline{m}_k = h_k(\underline{x}_k) + \underline{\epsilon}_k \tag{4.3}$$

where $h_k(\underline{x}_k)$ is the measurement function and $\underline{\epsilon}_k$ the experimental uncertainty. Moreover, both ϵ and w are assumed to be gaussian distributed with zero mean. The Kalman procedure consists of three steps: *prediction*, *filtering* and *smoothing*. In the prediction phase, the track parameter state in the k-th plane is evaluated making a prediction based on the state belonging to (k-1)th plane, without considering the noise contribution (eq. 4.4). On the other hand, in the respective covariance matrix prediction the noise contribution is propagated according the eq. 4.5, where F_k is the Jacobian matrix of the propagation function, defined as $F_k = \partial f_k / \partial x_k$.

$$\underline{x}_k^{k-1} = f_k(\underline{x}_k) \tag{4.4}$$

$$C_{k-1}^k = F_k C_{k-1}^{k-1} F_k^T + Q_k \tag{4.5}$$

In the filtering phase, the prediction is updated to the value $\underline{x}_k$ which minimises the incremental χ^2, defined in eq. 4.6.

$$\begin{aligned} \Delta\chi^2 = (\underline{x}_k - \underline{x}_k^{k-1})[C_{k-1}^k]^{-1}(\underline{x}_k - \underline{x}_k^{k-1})^T + \\ (\underline{m}_k - \underline{h}_k(\underline{x}_k))[V_k]^{-1}(\underline{m}_k - \underline{h}_k(\underline{x}_k))^T \end{aligned} \tag{4.6}$$

The terms $\underline{x}_k$ and C_k, are the minimisation outcomes

$$\underline{x}_k = \underline{x}_k^{k-1} + K_k(H_k(\underline{x}_k^{k-1}) \tag{4.7}$$
$$C_k = (I - K_k H_k)C_{k-1}^{k-1} \tag{4.8}$$

where K_k is the *Kalman Gain* (defined by eq. 4.9) and $H_k = \partial m_k / \partial x_k^{k-1}$.

$$K_k = C_k^{k-1} H_k^T (H_k C_k^{k-1} H_k^T + V_k)^{-1} \tag{4.9}$$

Then, $\underline{x}_k$ nd C_k are used for extrapolation from k-th plane to (k+1)th plane, and so on until the total number of planes is reached. After the Kalman steps have been performed on all hits of the track, the track can still be biased due to wrong starting values $\underline{x}_0$. This bias can be reduced by the repeated application of the procedure in the opposite order of hits (smoothing), using the previous fit result as starting values for the track parameters.

The Kalman filter is implemented in the reconstruction code using the GENFIT software toolkit [82, 83], that can easily integrated with the ROOT framework.

4.2 Expected performances

A Monte Carlo simulation tool, in which the Dose Profiler design is implemented, has been developed to study the detector features. The detector is simulated with the FLUKA software, while an event generator, based on the experimental data collected at HIT 2.3, is used to simulate the secondary proton production, in order to achieve the most reliable prediction on the emission shapes and energy spectra. In all the explored setup, a ^{12}C ion beam at 220 MeV/u with a gaussian shape with $\sigma = 0.8$ cm impinges a cylindrical or spherical phantom, while the Dose Profiler is placed at 40 cm with respect to the beam axis at 90° with respect to the beam direction. A preliminary evaluation of the detector performances has been performed, using a cylindrical PMMA target with radius 2.5 cm.

To select proton events, a discrimination on the basis of the energy released in the different detectors is performed. The energy release in the tracker, defined as the sum of the energy of all the fibre energy deposits (E_{fib}) and that in the scintillator (E_{scint}) have been studied for this purpose. In figure 4.4 the E_{Scint} vs E_{fib} distribution. The pinnacle structure graphed in black is due to reconstructed protons in the tracker. Two regimes can be distinguished: all the protons that stop in the absorber lead to the right curve, whereas the fastest protons that are able to go beyond the absorber generate the left curve. Conversely, the red events, characterised by E_{fib}<4 MeV and E_{scint}<7 MeV are due to particle different by protons, so they are excluded by the selection.

The relevant quantity that characterises the performances of the detector is the resolution on the proton origin along the beam direction (x in our case). It clearly depends on the angular resolution on the track, which in this case is $\sim 35\ mrad$. Such value is consistent with the multiple scattering angle inside the phantom, as expected. In figure 4.5 the difference between the reconstructed and the true

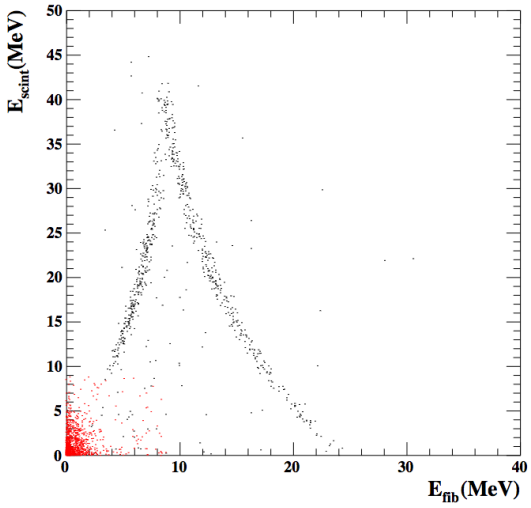

Figure 4.4. Released energy in the Absorber E_{Scint} as a function of the total released energy in the fibres E_{Fib}.

coordinate of the proton origin, fitted to the sum of two Gaussian functions, is shown. It results that for 90% of events, $\sigma_x = 0.42 \pm 0.02$ cm. This value represents the uncertainty on the single proton emission point, thus the Bragg peak uncertainty depends on the number of reconstructed proton that is possible to collect during a treatment.

4.3 Bragg peak reconstruction in a realistic case

The correlation between the Bragg peak position and the falling edge of the double Fermi-Dirac function, that is used to model the emission profile, has been studied in case of a fixed dimension homogeneous PMMA phantom impinged by Carbon ions [75]. In a real treatment secondary protons cross different path and materials inside the patient, generating a distorted emission shape with respect to the measured one in that situation. Thus, the Bragg peak position extrapolation can not be directly assessed with the mathematical parametrisation discussed in 2.3. In [84] the following method to overcome this technical difficulties is proposed:

- Associate to each emitted secondary proton the emission point coordinates in the plane orthogonal to the beam direction, that can be provided by the dose delivery system (DDS), in case of a scanning pencil beam treatment (a dedicated bus on the Dose Profiler Concentrator is dedicated to the communication with the DDS).
- Use the CT to obtain which kind of materials have been crossed by each fragment.
- Evaluate the emission profile assigning to each proton a different statistical weight, calculated according to the path lengths covered in each material, going

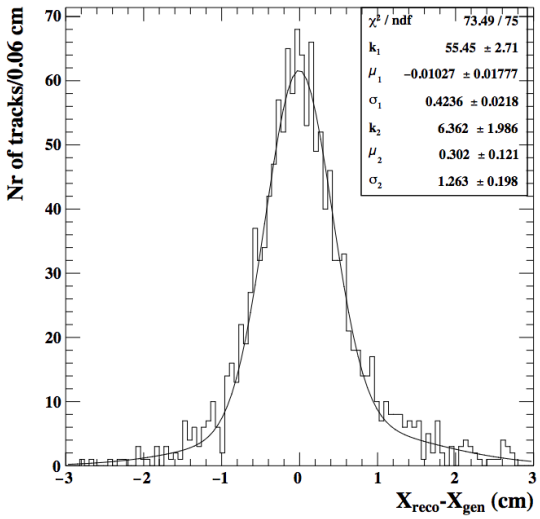

Figure 4.5. Distribution of the difference between the true and reconstructed proton emission x coordinate, as a result of the Monte Carlo simulation. A resolution of ~ 4 mm, compatible with the multiple scattering angle in inside the PMMA phantom.

back to the case measured in 4.3.1 and apply the mentioned technique. The Bragg peak depth is determined according to a previously built look-up table.

The correction factors evaluation procedure, as well as the application of such method in a realistic case are discussed hereafter.

4.3.1 Correction factors

The emission profiles for different PMMA thicknesses have been evaluated with the Monte Carlo simulation described above using cylindrical phantoms with radius in the range of 2.5 - 10 cm. The resulting shapes, shown in figure 4.6, have been used to study the behaviour of the parameters $\underline{p}(l)$. To take into account the attenuation effect in the mathematical model used in 2.3, the crossed thickness l dependence is introduced as shown in eq. 4.10.

$$f(x,l) = p_0(l) \cdot \frac{1}{1+e^{\frac{x-p_1(l)}{p_2(l)}}} \cdot \frac{1}{1+e^{-\frac{x-p_3(l)}{p_4(l)}}} \tag{4.10}$$

Each profile has been fitted using the equation 4.10, while the variation of the six parameters $\underline{p}(l)$ as a function of l has been fitted with polynomial function, as shown in figure 4.7. A large statistical sample ($2 \cdot 10^6$ primary Carbon ions) has been used in order to avoid large uncertainties which could affect the accuracy on the attenuation correction.

For each secondary proton passing though a PMMA target with thickness l, the weight is defined in the eq. 4.11

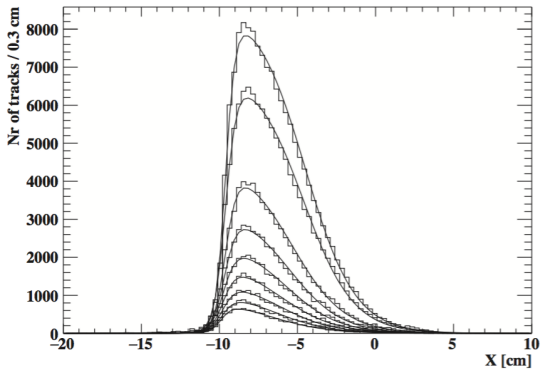

Figure 4.6. Reconstructed proton emission shape for different PMMA target thickness resulting of the simulation. Fits with the model described by eq 2.3 are superimposed.

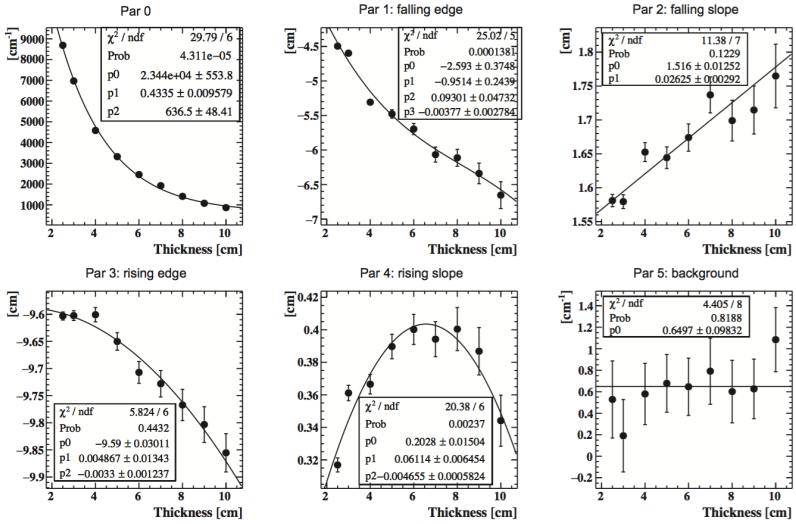

Figure 4.7. Parameters of the Fermi-Dirac model as a function of the PMMA radius, obtained with the Monte Carlo simuation.

$$w(x,l) = \frac{f(x,l_0)}{f(x,l)} \tag{4.11}$$

where $l_0 = 2.5$ cm corresponds to the reference length used in the experimental measurements. In case of different kind of crossed materials, the weight is calculated using an effective total path l_{eff}, defined in eq. 4.12

$$l_{\text{eff}} = \int_0^{s_{\max}} \frac{\rho(s)}{\rho_0} \left(\frac{Z(s)}{A(s)}\right) \left(\frac{Z_0}{A_0}\right)^{-1} ds \tag{4.12}$$

where ρ_0, Z_0, A_0 are the density, atomic number and mass number of PMMA, respectively, while $\rho(s)$, $Z(s)$, $A(s)$ correspond to the material features at the position s inside the patient.

4.3.2 Realistic case analysis

The aforementioned procedure has been tested reproducing a realistic case with a Monte Carlo simulation, whose results are summarised in[84]. A PMMA sphere of 10 cm radius, containing three smaller spheres of different materials to reproduce the effect of adipose tissue (1 cm radius), bones (1 cm radius) and a metallic implant (0.5 cm radius), has been used as a phantom to simulate a patient (figure 4.8). The emission profile has been estimated generating $\sim$ 15000 secondary protons. These correspond to the fragments that are approximately emitted from the distal slice of a treatment plan in which 1 Gy of physical dose is deposited in a $3 \times 3 \times 3$ cm^3 water cube, irradiated by ^{12}C ion beam at 220 MeV/u.

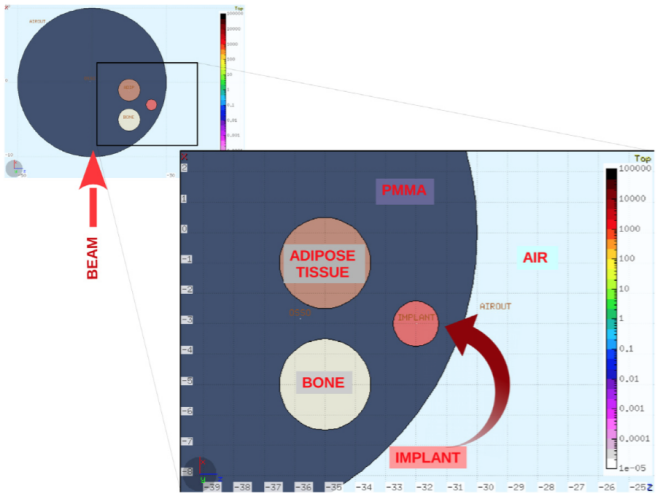

Figure 4.8. Non homogeneous phantom used in the simulation to evaluate the effect of the secondary proton absorption.

In figure 4.9 the raw emission profile, obtained considering the secondary protons emitted by the sphere, the reference profile, and the filtered profile, in which the correction factors are applied, are shown. A good agreement between the filtered and the reference profiles is observed, giving a preliminary confirmation of the technique efficacy.

However, the evaluation of the achievable resolution with this back-filtering technique is yet object of investigation. The CT miscalibration has clearly an impact on the capabilities of this method, as well as the uncertainties on the weight factor. The sensitivity of the method has been roughly checked shifting the sphere by 2 mm. As it is visible in figure 4.10, the effect is clearly detectable.

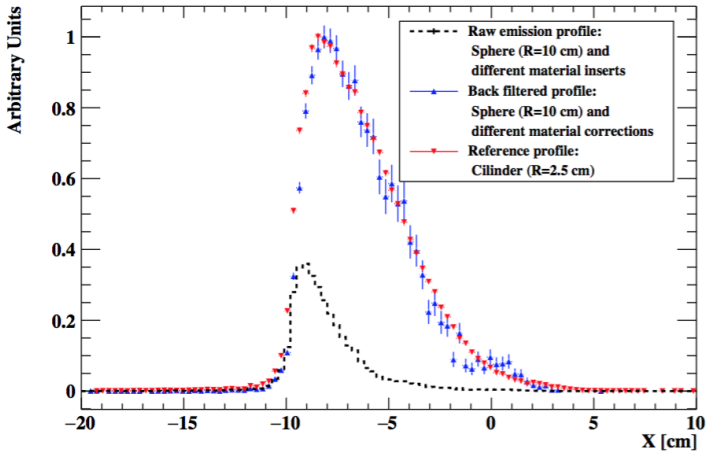

Figure 4.9. Raw emission profile (black dircles), reference emission profile (red circles), and filtered emission profile (blue circles).

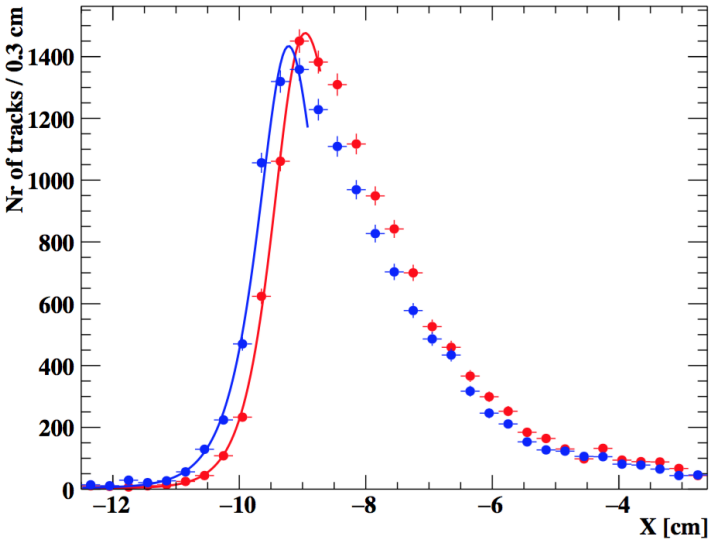

Figure 4.10. Filtered profiles obtained shifting the PMMA sphere by 2 mm with respect to the beam axis. The separation between the profiles is clearly noticeble.

Chapter 5

Detector characterisation

The Dose Profiler has been assembled in March 2017, with the aid of the mechanic service of the SBAI (Scienze di Base e Applicate per l'Ingegneria) University of Rome "La Sapienza" department. A preliminary study of the detector functionalities has been carried out using cosmic rays, to determine the working point in terms of thresholds, integration time constant of ASICs, and operation temperature. In May 2017 a test-beam has been performed in the experimental room of the Trento proton therapy center, with the aim to characterise the detector response using protons beams at the energies of interest of PT. As a final task of my Ph.D. activity, I was involved in the data-taking, directly handling the experimental setup and analysing the collected data. The charge response, the detection efficiency and the reconstruction spatial resolution of the Dose Profiler have been evaluated. The obtained results are summarised hereafter.

5.1 Cosmic rays preliminary measurements

The number of parameters that determines the Dose Profiler signal response is quite large: the gain and the integration time constant $\tau = C_F R_F$ of the ASICs amplification stages, the corresponding discriminators thresholds, the SiPMs bias voltage and the operation temperature, which deeply affects the SiPMs gain and noise. Moreover, the effects induced by the tuning of the above-mentioned parameters are clearly correlated, then the definition of a *golden* set of parameters, capable to maximise the detector signal-to-noise ratio is not an easy task. Notwithstanding the Dose Profiler has been expressly thought to detect protons, this work has been performed exploiting cosmic rays, exploring the detector performances even with MIP (Minimum Ionising Particles).

5.1.1 Experimental setup and trigger

The Dose Profiler has been vertically oriented and placed on the laboratory desk, as shown in figure 5.1. The internally generated trigger has been used for the data acquisition, requiring the coincidence in a 50 ns time window between the three *double-plane* involved in the fibres read-out (defined in 3.1.3). Each *double-plane* signal is generated by the time coincidence of at least one SiPM per view. This

entails that in a triggered event at least 6 SiPM over threshold are acquired. A synthetic view of the trigger logic is shown on figure 5.2, while a 2-D event display of a cosmic that crosses the detector is shown in fig 5.3,

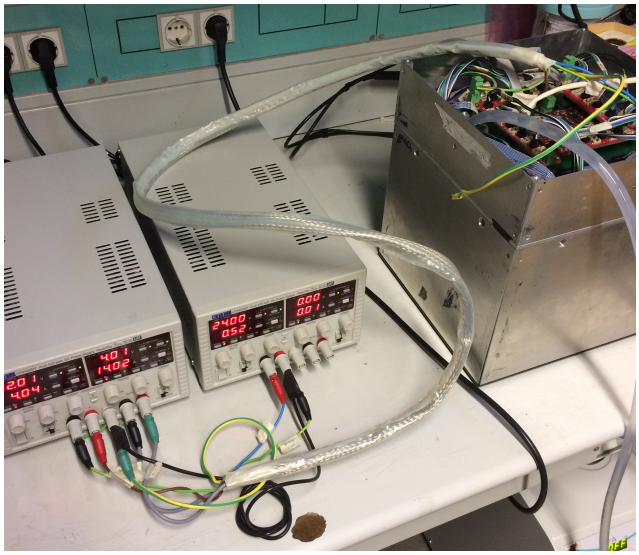

Figure 5.1. Dose Profiler during a cosmic rays data acquisition.

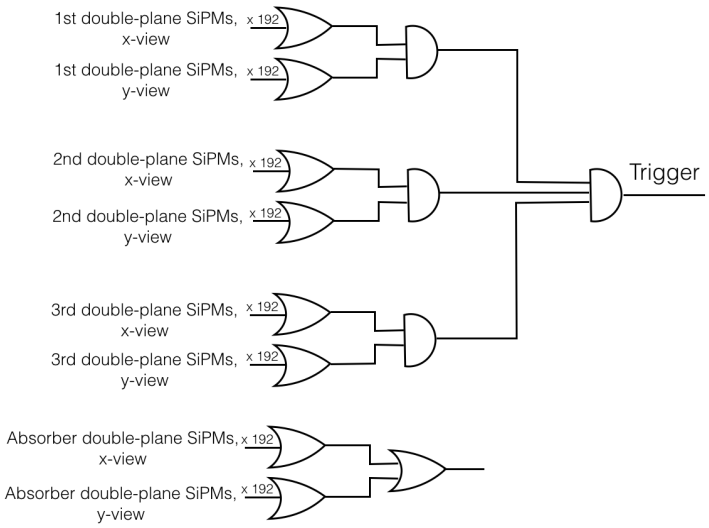

Figure 5.2. Schematic view of the trigger logic used to detect muons. The absorber is not involved in the trigger generation.

5.1.2 Working point determination

To reduce the parameter space, it was decided to fix the SiPM bias voltage, supplying each board in order to have the same SiPM gain, according the specifics provided by

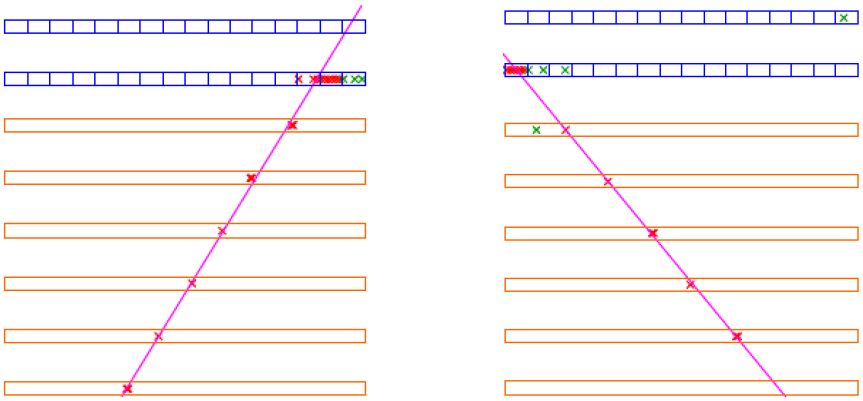

Figure 5.3. View of the muon passage in the Dose Profiler, in the x-y views. The fibres planes and the scintillator rods are represented by the orange and blue rectangles, respectively. The red stars are associated to the SiPMs whose charge is over the set threshold.

Hamamatsu for each single SiPM. An additional simplification has been introduced fixing the amplifiers feedback capacitance C_F to 1 pF, corresponding to the configuration with the maximum available gain but at the same time the smallest dynamic range ($\sim$ 28 pC, as reported in [77]), sufficient to cover the 50-150 MeV proton range. Considering a SiPM gain of $1.25 \cdot 10^6$, 28 pC coincides with $\sim$ 140 photoelectrons, which is comparable with the expected number of photoelectrons by a 50 MeV proton. The value of the feedback resistance R_F, which determine the integration time, could slightly affect the charge amplifier gain, since if the time constant is small with respect to the duration of the SiPM signal, the feedback capacitance C_F starts to discharge before to reach the peak, reducing the gain. The impact of this effect on the detection efficiency has been evaluated looking at the cosmic detection rate as a function of the internal discriminator threshold, for different τ, fixing the cooling water temperature at 12°C. Two concurrent effects are expected: reducing the time constant the gain decreases and the signal discharges more quickly, forcing to use a lower threshold to achieve the same detection efficiency. On the other hand, an excessive threshold reduction enhances the internal trigger rate due to the SiPMs noise, until the muon signal detection is avoided by the intrinsic ASIC dead time. The rate of reconstructed tracks as a function of the threshold and τ is shown in fig. 5.4. The maximum rate, i.e the maximum detection efficiency, is achieved for $thr = 32$, $\tau = 66ns$. This couple of parameters is taken as a reference for the rest of the measurements.

5.1.3 Temperature determination

The temperature impact has been studied separately, setting the cooling water to 18 °C, 15 °C and 12 °C. It was not possible to explore lower temperatures, because of condensation on the detector aluminium skeleton. The reconstructed tracks rate as a function of the temperature is shown in figure 5.5. Between 121 °C and 15 °C the cosmic rays detection efficiency drops at $\sim$ 10%, while between 12°C and 18°C the reduction is of the order of $\sim$ 30%. Although these variations are not expected using

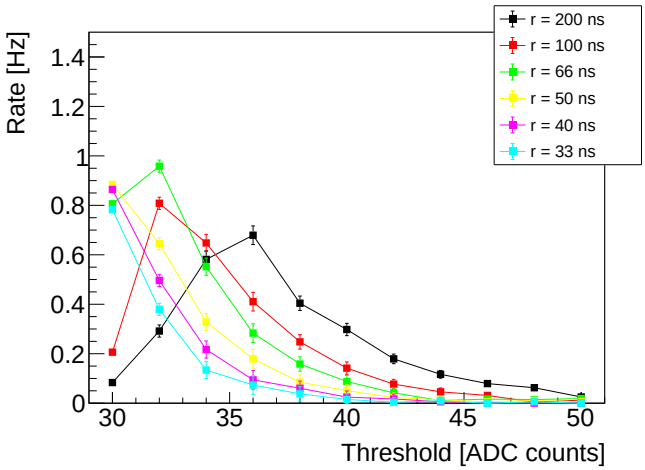

Figure 5.4. Rate of the reconstructed tracks as a function of the threshold, for different integration time constants.

protons, because of the larger amount of emitted light, 12°C has been prudently chosen as reference working temperature for the characterisation measurements with proton beams.

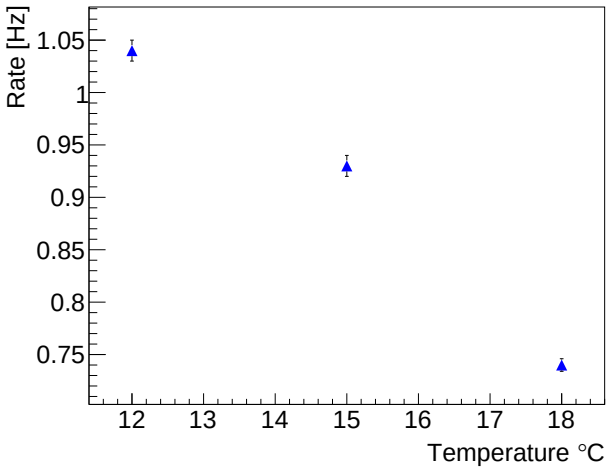

Figure 5.5. Rate of the reconstructed tracks as a function of the cooling water temperature.

5.2 Test-Beam @ Trento proton therapy center

The Trento proton-therapy centre is an Italian particle therapy facility that started the clinical activity in 2014. A cyclotron provided by IBA serves two medical treatment rooms both equipped with rotating gantries, where more than 300 patients have been treated (updated at March 2017) including paediatric patients [85]. The

facility is also equipped with an experimental cave, dedicated to a large spectrum of scientific applications, and supervised by the Trento Institute for Fundamental Physics and Applications (TIFPA). The IBA cyclotron accelerates protons up to 228 MeV, with a minimum exit energy of 70 MeV, while the beam spot size measured at the isocenter are in the 3 - 7 mm (sigma) range, depending on the beam kinetic energy. Despite the beam intensities typically used in standard treatments are 10^6 - 10^8 p/s, it is possible to reach lower intensities 10^1 - 10^5 p/s decreasing the high voltage of the accelerator source below the threshold used for standard operations.

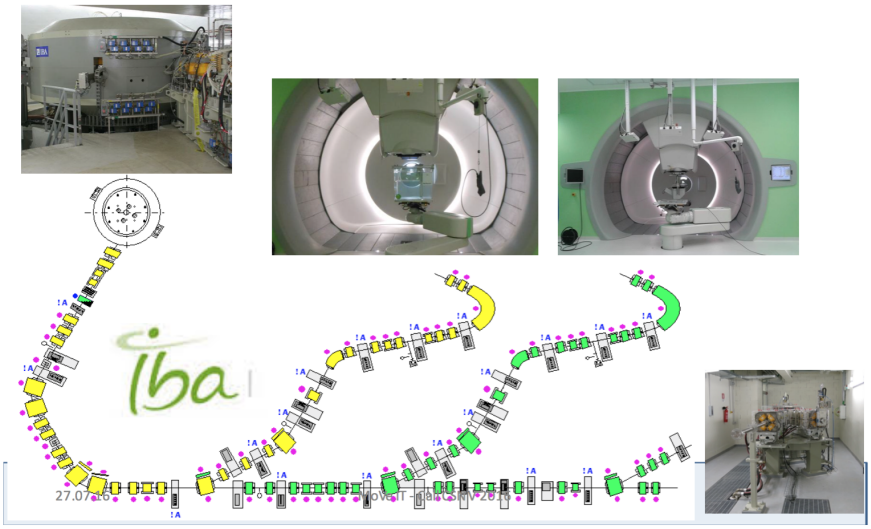

Figure 5.6. View of the Trento facility: the beam is delivered in two treatment rooms, and an additional experimental cave dedicated to research.

5.2.1 Experimental setup and trigger

The Dose Profiler has been tested using proton beams at intensities of the order of $\sim 10^3$ p/s. It has been placed on a remotely controllable table, able to shift along the direction perpendicular to the beam line with millimetre-level precision steps. The height with respect to the floor was manually regulated with two jack laying on the table surface. The detector entrance face was 50 cm distant from the room isocenter. Two plastic scintillators (STS1 and STS2) with size ($5 \times 5 \times 1$ cm^3), and read-out by photomultipliers Hamamatsu H10520, have been positioned before the Dose Profiler, at times. The number of time coincidences between STS1 and STS2 was counted with an oscilloscope to independently monitor the beam intensity. Furthermore, the time coincidence could have potentially acted as an external trigger for the Dose Profiler data acquisition. However, all the results presented in after in this chapter, are obtained using the internally generated trigger, with the same logic set for cosmic rays (5.1.1). In figure 5.7 the experimental setup is schematically reported, while in the figure 5.8 a picture taken during the measurement operations is shown.

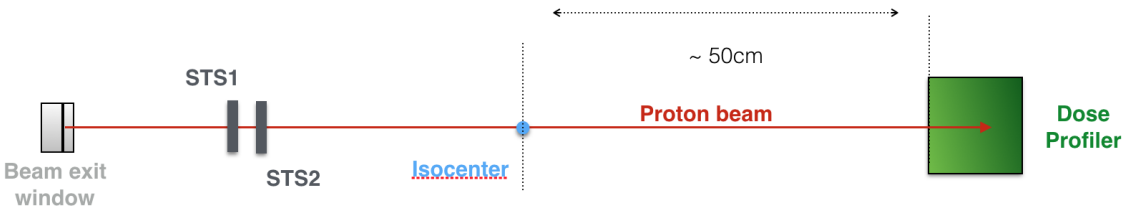

Figure 5.7. Setup of the test-beam for the Dose Profiler characterisation.

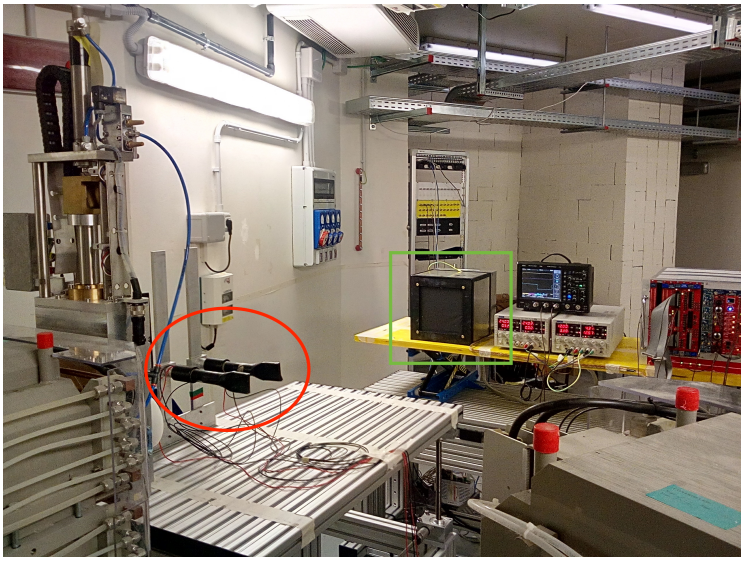

Figure 5.8. Picture of the Trento experimental room, showing the test-beam setup. In the red circle STS1 and STS2 scintillators, used to monitor the beam intensity, can be observed, while the Dose Profiler is pointed out by a green square.

5.2.2 Signal topology

Firstly, the topology of the signal generated by the passage of a proton inside the detector has been studied. As explained in the section 4.1, the tracks are obtained using SiPM clusters, formed joining the neighbour SiPMs. Then, the track-finder looks for at least 4 aligned cluster in both the x-y views to identify a track in the event. A small cluster size, i.e. the number of SiPM contained in a cluster, is clearly desirable since it directly affects the spatial resolution on the reconstructed emission point coordinate. In figure 5.9a the cluster size distributions for proton at 228, 159, 112, 70, and 44 MeV, obtained selecting only the clusters belonging to the track using a 10^6 event sample, are shown. The lower energy has been achieved placing a solid water layer in front of the beam exit window. The corresponding mean cluster size as a function of the proton kinetic energy is shown in figure 5.9b. The cluster size is greater at low energies, as expected, since a larger number of photons is produced in the fibres, always resulting less than 2 in the energy range between 44 MeV and 228 MeV.

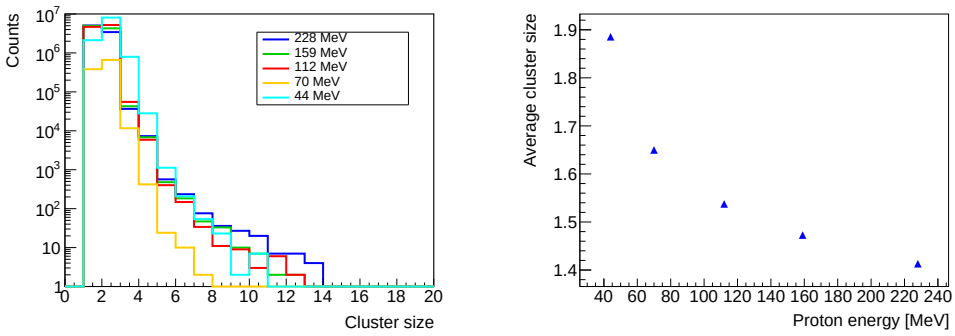

Figure 5.9. Cluster size for different proton energies (top picture), and mean cluster size as a function of the proton energy (bottom picture).

5.2.3 Charge response

The Dose Profiler is designed to measure the proton energies using the deposited charge in the fibres and in the absorber, to potentially exclude the slowest protons, which worsen the resolution on the emission point coordinate reconstruction because of the multiple scattering in the patient. Moreover, the kinetic energy is taken as input by Kalman filter to find the best-estimate of the track parameters taking into account the effect of the multiple scattering inside the Dose Profiler itself, as explained in chapter 4.1.2. In this paragraph the charge response of the Dose Profiler is investigated, and a preliminary estimate of the incoming secondary protons charge resolution is assessed. In figure 5.10 the single channels charge distribution are shown for proton of 228 MeV, 159 MeV, 112 MeV, 70 MeV and 44 MeV, distinguishing from the contribution of the tracker SiPMs and the absorber SiPMs, marked in blue and in green, respectively. The charge spectra are broaden on the whole dynamic range of the ASICs. By the way, the fraction of events in which the SiPM charge is saturated is less 0.2% for energies between 70 MeV and 228 MeV, while is of the order of 2% at 44 MeV. The events in which at least one SiPM suffer of charge saturation are skipped in this analysis.

The total amount of released charge Q_{fib} and Q_{ab}, in the fibres and in the absorber respectively, are shown in figure 5.11. 44 MeV protons stops in the first absorber layer, thus inducing very large fluctuations in the deposited energy. However, the charge resolution has been evaluated using normalised value defined in eq 5.1

$$Q^N_{fib} = \frac{Q_{fib}}{N_{lay}} \tag{5.1}$$

$$Q^N_{ab} = \frac{Q_{ab}}{N_{SiPM}} \tag{5.2}$$

The charge deposited in the fibres is normalised to the number of layers N_{lay} which have at least one cluster above threshold, to reduce the fluctuations due to the potential layer inefficiency. Instead, the charge released in the absorber has been normalised to the number of SiPM N_{SiPM} over threshold associated to the track, to reduce the fluctuations due to the light collection inefficiency of the SiPM further away from the scintillator slab in which the energy has been deposited.

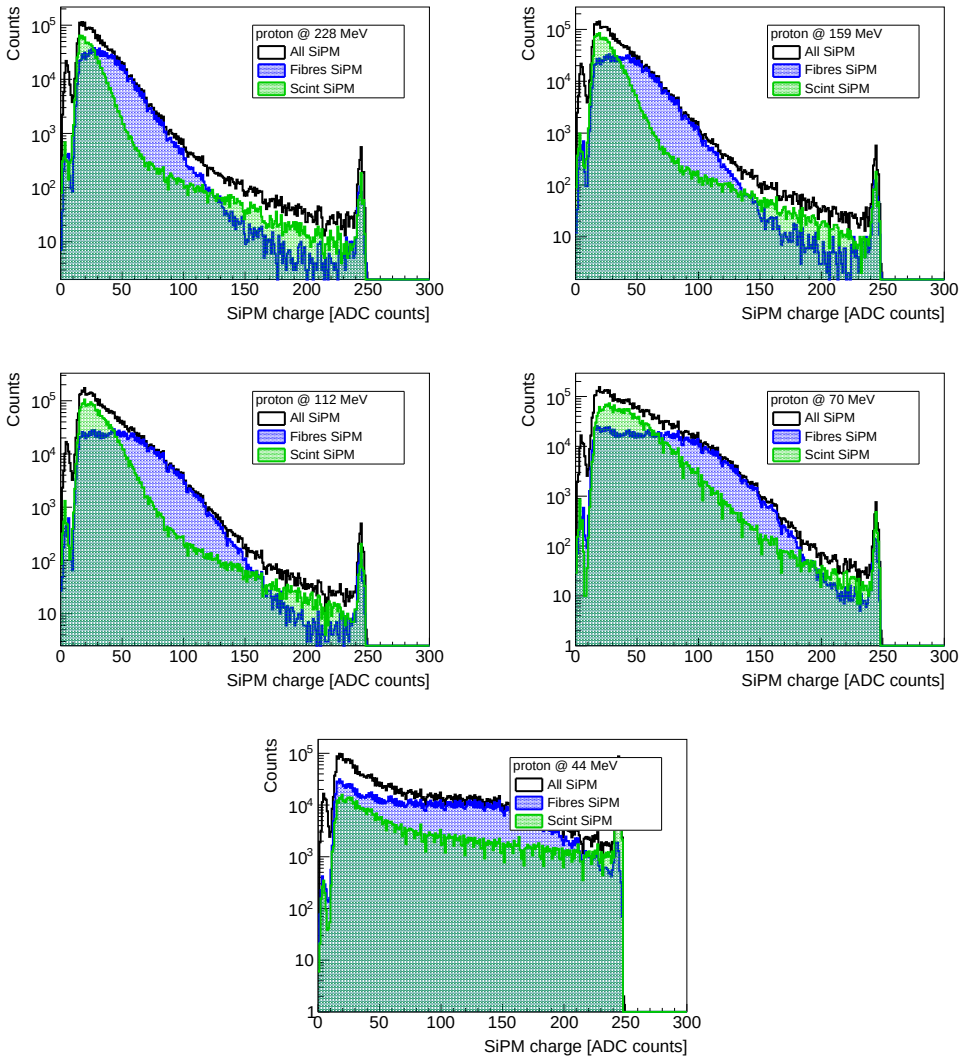

Figure 5.10. Distribution of the SiPM charge for proton at 228 MeV, 159 MeV, 112 MeV, 70 MeV and 44 MeV. The blue and green histograms discern the contribution of the SiPMs coupled to the fibres and to the plastic scintillator rods, respectively.

The achieved distributions of Q^N_{fib} and Q^N_{ab}, shown in figure 5.12, have been fit with gaussian functions to evaluate $\sigma(Q)/Q$ as a function of the proton kinetic energy. The results are summarised in the graphs shown in figure5.13. Using the charge released in the fibres, the charge resolution varies between 14.7% and 17.3 % for proton energies in the 44-228 MeV. On the other hand, using the energy deposited in the scintillator slabs, the energy resolution is below 10% for all the available energies.

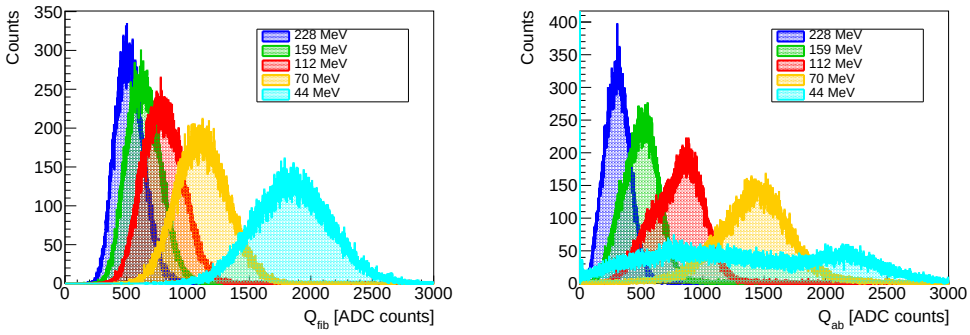

Figure 5.11. Total amount of released charge Q_{fib} and Q_{ab}, in the fibres and in the absorber, respectively.

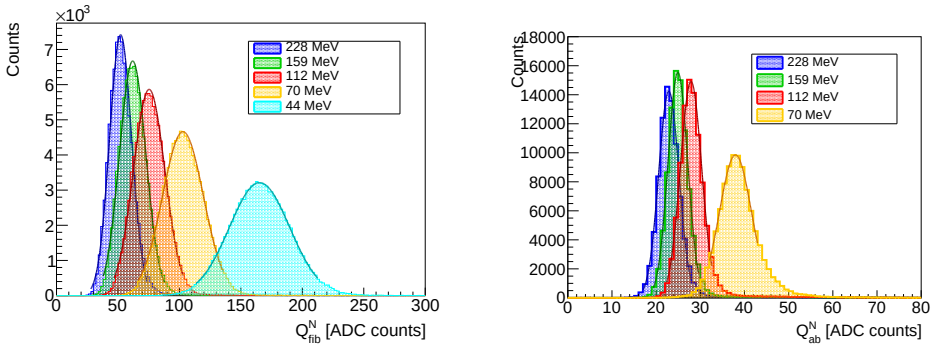

Figure 5.12. Distributions of the normalised deposited charge in the fibres (left figure), and in the absorber (right picture), for different energies. The charge distribution for protons at 44 MeV have not been considered since they stop in the first scintillator layer.

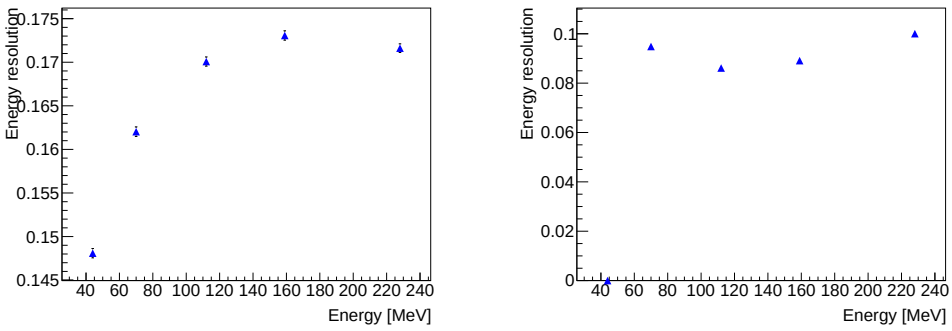

Figure 5.13. Charge resolution as a function of the proton energy obtained with the fibres signals (left figure), and with the absorber signal (right figure).

5.2.4 Detection efficiency

Monitoring the beam range with charged secondary particles can be a more useful approach with respect to the gammas detection in ^{12}C ion beams treatments. Indeed, the relatively low number of charged fragments emitted at large angle with respect

to the beam direction is compensated by a potentially high detection efficiency, overcoming the difficulties of neutral radiation based technique. Hence, the evaluation of the Dose Profiler efficiency is an issue of outmost importance. For this purpose, the detector has been irradiated with proton beams at 228 MeV, 159 MeV, 112 MeV, 70 MeV, and 44 MeV, impinging the device centre, and with proton at 91 MeV, continuously moving the platform position with respect to the beam direction in order to test the full detector active volume. The events have been acquired using the internally generated trigger, with the logic described in 5.2.1. The layer detection efficiency ϵ_{iv} has been evaluated for each fibre layer i separately for the two x-y views v, using the formula reported in eq. 5.3

$$\epsilon_{iv} = \frac{N^{iv}_{rec}}{N^{iv}_{\text{tot}}} \tag{5.3}$$

where N^{iv}_{tot} is the number of the 2D tracks reconstructed in the v-th view excluding the i-th layer in the track-finding algorithm, while N^{iv}_{rec} is the number of identified tracks in which a cluster in present in the i-th plane of the v-th view. This definition assures an unbiased estimate of the layer detection efficiency without using an external trigger. The layer efficiencies resulting by the full volume scan at 91 MeV (corresponding at $\sim 3 \cdot 10^6$ events) are reported in the graph shown in figure 5.14. Systematic uncertainties have to be still evaluated at present, while the statistical uncertainty bar is smaller that the point maker. For all the layers, the detection efficiency is of the order of 90%, which is an expected value considering the dead space between the fibres (see 3.1.1), fibre cladding and the possible light collection inefficiencies in the coupling with read-out electronics.

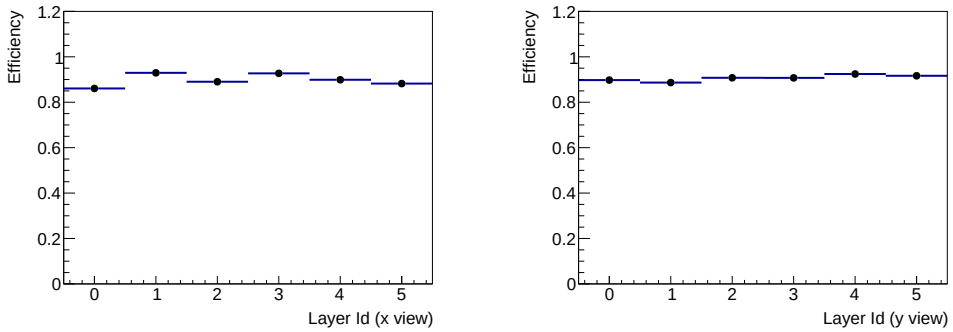

Figure 5.14. Detection efficiency for each fibre plane: the layer oriented in the x-view and the y-view are shown in the left and right figure, respectively.

To check the uniformity of the detection efficiency as a function of the position along the layers, the detection efficiency has been computed grouping the track according the track impact point on each layer x (or y), in 1 mm bins. The results are shown in figure 5.16, and a very good homogeneity can be observed. Starting from the single layer efficiency ε_{iv}, the overall efficiency ε, defined as the probability to trigger and track a proton that crosses the Dose Profiler, has been calculated. Reminding that the trigger signal fires when at least one SiPM per view goes over

threshold in at least three *double-plane*, and and that a track is identified by 4 aligned clusters (4.1.1), all the possible combinations in which three double-planes are fired and at the same time four plane have given a signal, have to be considered. It's convenient to define the following quantities:

- $\epsilon_i = \epsilon_{ix}\epsilon_{iy}$, corresponding at the probability to detect a signal both the x-y views of the i-th plane.
- $s_j = \epsilon_j(1-\epsilon_{j+1}) + \epsilon_{j+1}(1-\epsilon_j)$, which is the probability to detect a signal in one of two adjacent planes, forming a j-th *double-plane*.
- $d_j = \epsilon_j\epsilon_{j+1}$, which represent the probability to detect a signal in both of two adjacent planes, forming a j-th *double-plane*.

Thus, ε can be calculated summing all the possible combinations for the three double-plane, identified by the indexes 0,1,2. The mathematical expression is given by eq. 5.4

$$\epsilon = d_0s_1s_2 + s_0d_1s_2 + s_0s_1d_2 + d_0d_1s_2 + d_0s_1d_2 + s_0d_1d_2 + d_0d_1d_2 \tag{5.4}$$

ϵ is shown as a function of the proton kinetic energy in figure 5.15. It varies between 95% for protons at 44 MeV, down to $\sim$ 80% for protons at 228 MeV.

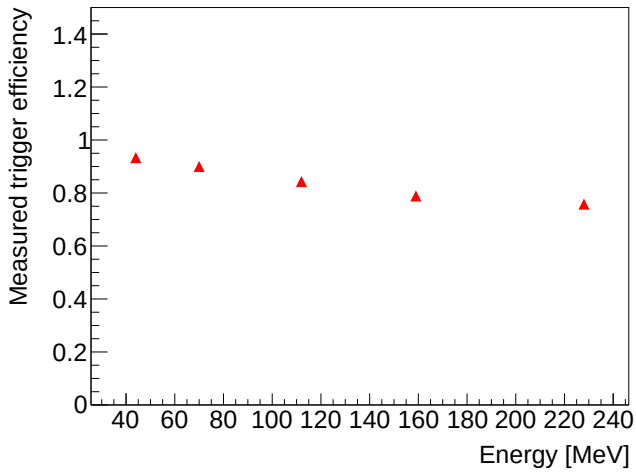

Figure 5.15. Global efficiency, defined as the probability to trigger and track a proton crossong the Dose Profiler, for protons at 228 MeV, 159 MeV, 112 MeV, 70 MeV, 44 MeV.

5.2.5 Back-tracing resolution

The aim of the Dose Profiler is to back-trace the reconstructed protons trajectories inside the detector volume toward the patient, to reconstruct the emission points. The back-tracing capabilities of the detector were tested reconstructing the Trento

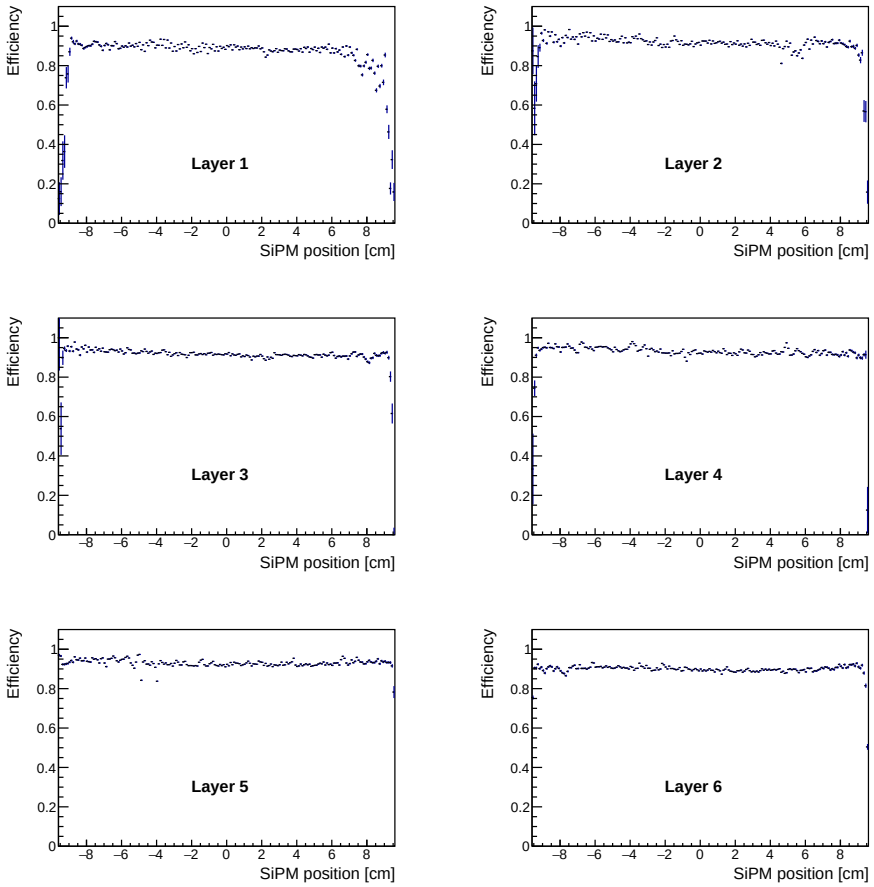

Figure 5.16. Detection efficiency as a function of the position along the Y layer.

beam spot at the isocenter position, which was $\sim$ 50 cm distant from the Dose Profiler entrance face in order to reproduce the planned distance in working operation conditions at CNAO. The beam profiles were reconstructed both in the X and Y view, exploring four different energies, namely 228 MeV, 159 MeV, 112 MeV and 70 MeV. Lower energies would have been also available inserting solid-water scatterers after the beam exit window, but the resulting beam spread-out avoids to obtain the Dose Profiler spatial resolution without a dedicated Monte Carlo simulation development, not available at present. Each beam profile has been fit with a gaussian function, and the spatial resolution on the reconstructed position has been extracted by quadrature subtraction, according the eq. 5.5

$$\sigma_{\text{reso}} = \sqrt{\sigma^2_{\text{meas}} - \sigma^2_{\text{beam}}} \tag{5.5}$$

where σ_{beam} are the nominal spot size, derived by the beam characterisation measurements reported in [85], and σ_{meas} are the corresponding sigma obtained by the fit. The results are shown in figures 5.18 and 5.19. The achieved spatial resolutions on the reconstructed coordinates are in the range between 3 mm and 5 mm, resulting quietly independent by the beam energy down to to 100 MeV. Hence,

the Dose Profiler intrinsic tracking resolution gives a quite negligible contribution to the overall resolution achievable in standard treatment conditions, since the accuracy worsening due to the multiple scattering inside the patient is of the order of ~ 8 mm.

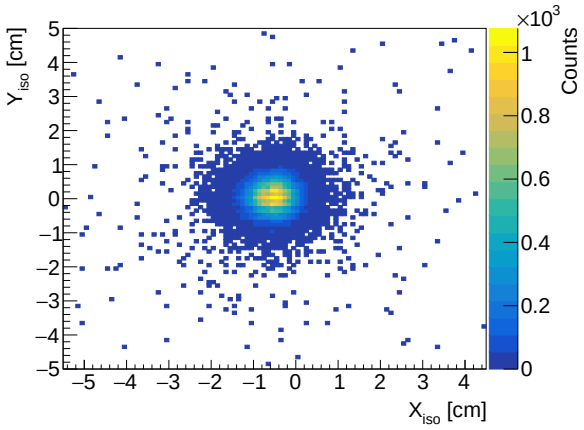

Figure 5.17. Bidimensional reconstructed beam spot at 228 MeV.

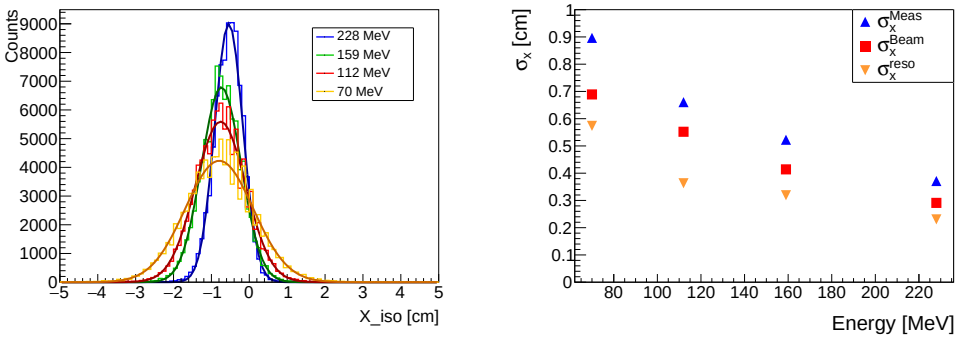

Figure 5.18. Beam profiles along the x-axis for different energies (left figure), and corresponding achieved resolutions (right figure).

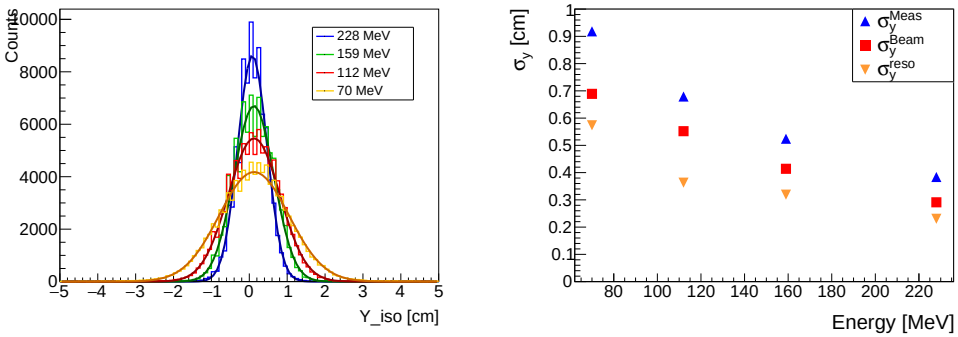

Figure 5.19. Beam profiles along the y-axis for different energies (left figure), and corresponding achieved resolutions (right figure).

The tracking resolution capabilities has been also directly observed reconstructing the image of a tantalum absorber, placed along the beam axis at the isocenter as shown in figure 5.20, and in the proximity of the entrance face of the detector, leaned to the Tedlar window. In the second setup, a solid-water layer has been positioned after the beam exit window to broaden the beam, in order to cover all the detector surface. The reconstructed images are shown in figure 5.21 .

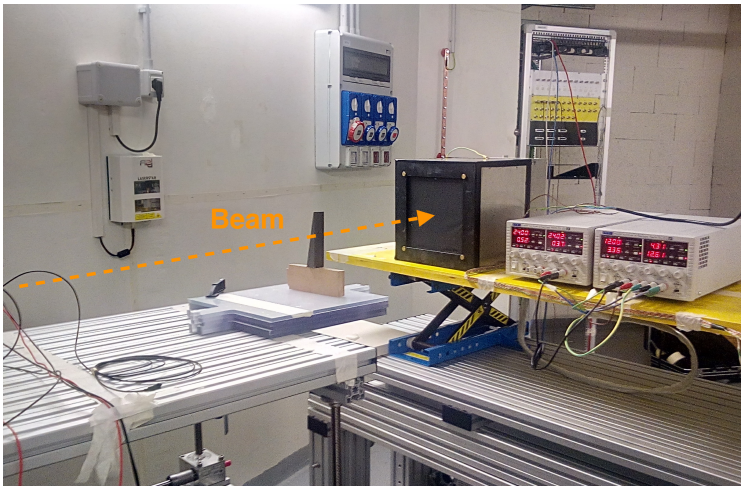

Figure 5.20. Picture of the tantalum absorber placed at isocenter position.

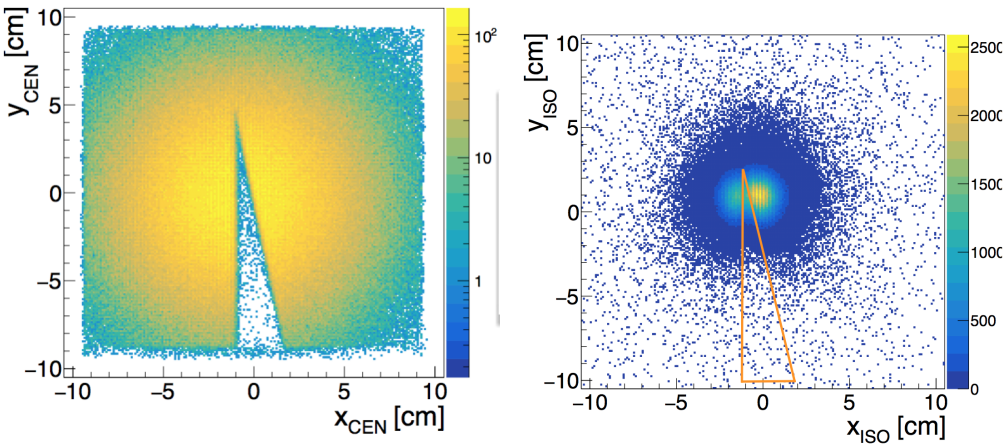

Figure 5.21. Reconstructed image of the tantalum absorber placed at on the Dose Profiler entrance face (left) and at isocenter position (right), obtained by the proton track back-tracing.

5.2.6 Dead time

A dead time estimate has been finally performed, to test the maximum data acquisition rate capabilities of the read-out system in realistic operating conditions. The dead time is internally measured by a counter (10 ns clock period), located in the Concentrator, that is activated when the trigger fires and stops when the event transmission has completed and a new trigger could be generated. Except for the first acquired event, in each data structure a 32-bit word contains the dead time of the previous event. The dead time distributions obtained by the acquisition of runs at different proton energies, are shown in figure 5.22. The mean value is $\sim 80\ \mu s$, and does not depend on the energy, despite the mean event multiplicity (defined as the number of SiPM that have provided a signal over the threshold) varies between 30 and 60 with increasing the energy. This is confirmed directly looking at the multiplicity-dead time scatter plot (figure 5.22), obtained integrating the events at all the explored energies. None correlation is observed, indicating also that the multi-peak dead time structure does not derive from the event multiplicity fluctuations.

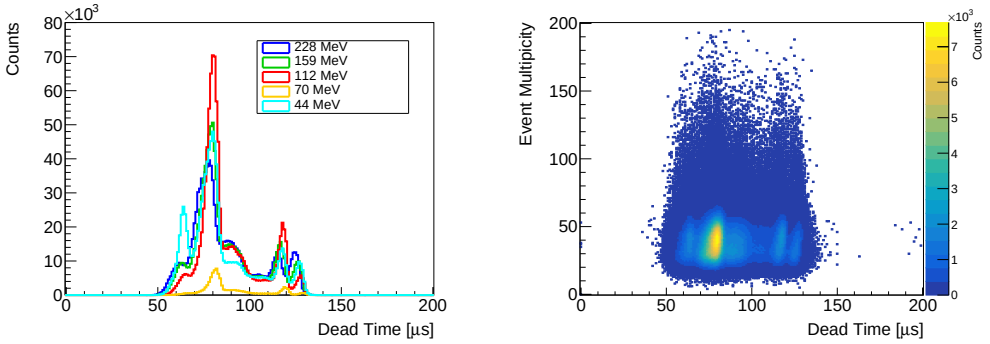

Figure 5.22. Dead time distributions (left figure) and multiplicity-dead time correlation (right picture)

A toy Monte Carlo simulation has been developed to evaluate the dead time impact on the event loss fraction, considering the measured dead time distributions. The simulation is structured as follows:

- Giving a initial *true rate*, the number of events expected in a 10 s time window is extracted according a Poisson distribution.
- Then, the arrival times are extracted according a uniform distribution between 0 and 10 s.
- For each event a dead time is provided, sampling the measured dead time distribution. The lost events are excluded, and the *expected measured rate* is computed counting the number of the detected events.

The expected rate as a function of the true rate is shown in figure 5.23, compared to the expected rate obtained applying the same procedure but considering a fixed dead time of 80 μs. In the explored range between 1 kHz and 20 kHz, small difference

are present above $\sim$ 12 kHz between the two methods. The fraction of lost events is evaluated by the the ratio between the measured rate and the true rate.

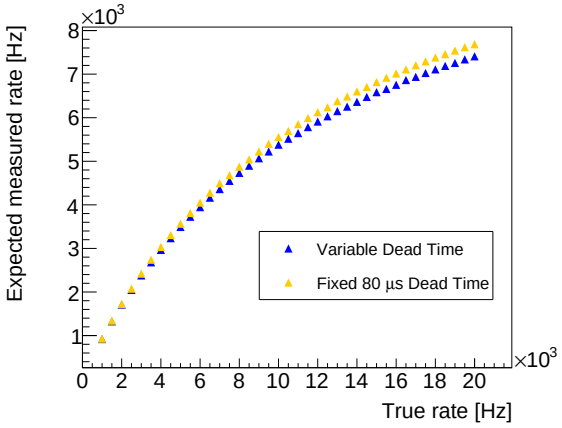

Figure 5.23. Expected measured rate with the Dose Profiler, obtained taking into account the dead time. A slight difference at rate $>$ 12 kHz is observed

Chapter 6

Secondary charged fragment production with ^{12}C ions beam

In chapter 2 the measurements of charged fragments production at large emission angles have been shown for PMMA targets irradiated by ^{12}C ion beams. A patient is evidently a more complex target, due to its irregular geometry and composition. Hence, experimental measurements reproducing a realistic clinical case are strongly needed to confirm the feasibility of the technique proposed in this thesis, due to the scarce reliability of Monte Carlo models for the production at large emission angles. At this purpose, in July 2017, a data taking campaign has been performed at CNAO to measure the charged secondary fragments production in a realistic case, using an anthropomorphic phantom irradiated by ^{12}C ion beams. The Dose Profiler was used for the fragments detection, to test its performances in treatment-like conditions. The data analysis is currently ongoing, but preliminary results are already available and are presented as a final item of my Ph.D. thesis, in this chapter.

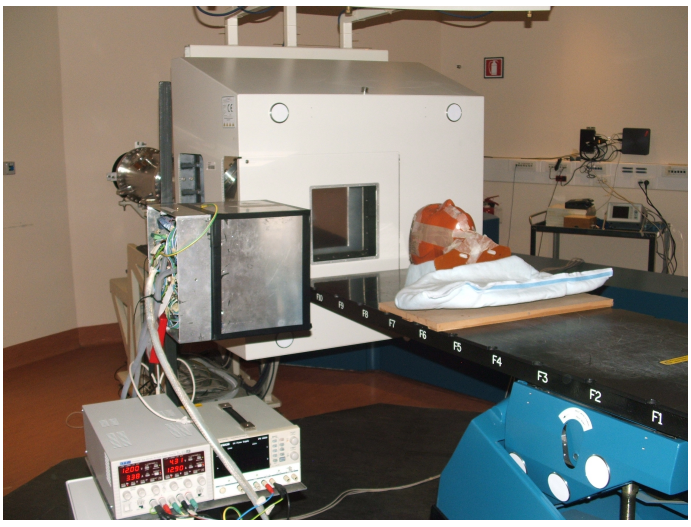

Figure 6.1. Picture of the CNAO treatment room where the experiment has taken place. The Dose Profiler appears on the left, while the anthropomorphic phantom lies on the room table.

6.1 Experimental setup

CNAO is an Italian PT facility which started its clinical activity in 2011, providing treatments both with protons and ^{12}C ions beams. The particles are accelerated by a synchrotron, which can provide energies up to 250 MeV for protons and 480 MeV/u for ^{12}C ions, and are routed and in three different treatment rooms. The experiment setup has been installed in third CNAO treatment room, as shown in figure 6.1. The Dose Profiler (DP) has been placed on the side of the table, supported by a provisional cart with wheels, capable to easily move in different positions. The device height above ground was fixed at 120 cm, in such a way that the horizontal plane containing the room isocentre (IC) intersected the Dose Profiler centre. Two different configuration have been investigated to detect secondary fragments at 90° and 60° with respect to the beam direction (figure 6.2). In the former case the DP was at $\sim$ 45 cm from the room isocentre, to explore the planned distance in the final configuration. In the second arrangement, such distance was avoided due to encumbrance of the robotic arm which controls the table movements, so the DP was positioned at $\sim 1\ m$ from the isocentre.

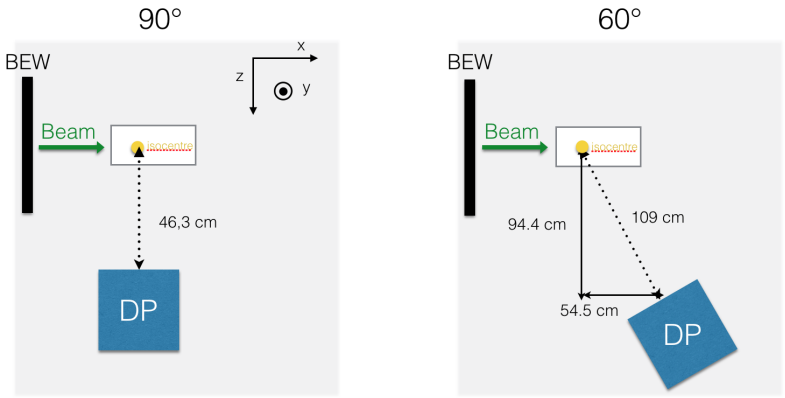

Figure 6.2. Schematic view of the CNAO experimental setups, at 90° and 60° detection angles.

An anthropomorphic head phantom (PH), moulded of tissue-equivalent materials, has been used as a target. The phantom lied on the table, in such a way to completely enter in the Dose Profiler field of view. The beam impinged the skullcap centre, placed at $\sim$ 60 cm form the beam exit window (BEW) as shown in figure 6.3.

The phantom was irradiated in three different ways:

- Producing single spots using monochromatic ^{12}C ions pencil beams with energies of 180 MeV/u, 220 MeV/u, 280 MeV/u and 320 MeV/u.
- Creating 3×3 matrixes using monochromatic ^{12}C ions pencil beams at distance 3 cm from each other, with energies of 180 MeV/u, 220 MeV/u, 280 MeV/u and 320 MeV/u.
- Building a $3 \times 3 \times 6$ cm^3 dose cube using beams at different energies.

The same SiPM bias voltages, thresholds, gain and trigger logic used at Trento test-beam were used 5.2.1, to maintain the same detector response.

Figure 6.3. Head phantom irradiated by ^{12}C ions beams for secondary fragments production studies at CNAO.

6.2 Simulation

A Monte Carlo simulation, in which the CNAO experimental setup is reproduced, has been developed with the FLUKA software. A faithfully implementation of the CNAO dose delivery system, provided by the CNAO staff, is included as well. In figure 6.4 the schematic setup view, provided by the FLUKA graphic user interface, is shown. The purple and ocher parallelepipeds in the picture background represent the beam exit window, while the black one reproduces the table surface. Customised routines have been coded to built a track database in which the fundamental information about all the created particles in each event, such as the generation positions, the momentum and the released energy in the Dose Profiler fibres, are stored. The software tools that perform the particles track reconstruction are the same used for experimental data, adapted to manage the Monte Carlo quantities.

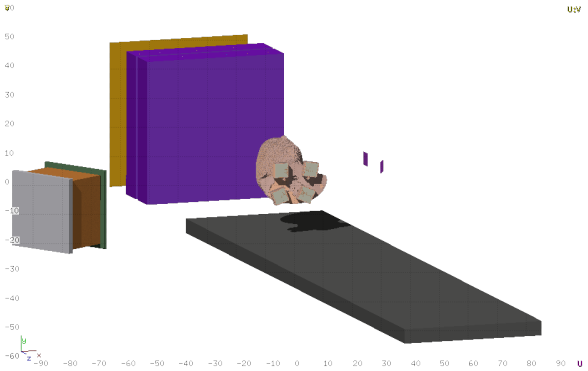

Figure 6.4. View of the CNAO experimental setup in the FLUKA software.

To correctly simulate the phantom head, the densities obtained by a phantom CT scan have been used. To this aim, FLUKA is able to import the densities for each voxel, given by the DICOM files [1]. CT densities are expressed in Hounsfield units (HU), typically used in CT images to parametrise the stopping power of a certain tissue. The conversion between HU and the real material density is automatically

[1]DICOM (Digital Imaging and COmmunication in Medicine) is the standard used to store the medical images information, developed to ensure the interoperability of different medical imaging systems

performed by a specific FLUKA tool, basically applying calibration coefficients available for different tissues [86]. The resulting imported geometry is shown in figure 6.5.

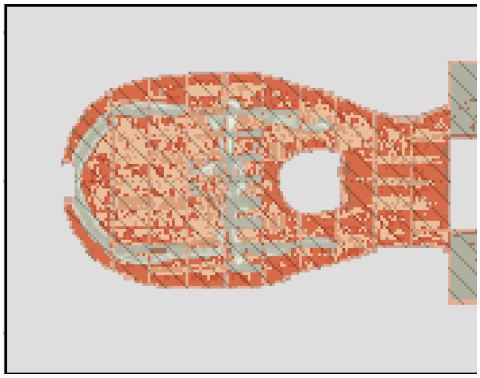

Figure 6.5. CT image of the head phantom, implemented in the FLUKA simulation.

6.3 Track distributions

The measured emission point distributions along the x-y axes, standing for the beam and vertical axes respectively, are shown for the three different irradiation modalities in figures 6.6, 6.7, 6.8. The detection angle is 60°. In all the explored conditions a halo surrounding a hot region is evidently observed. A single pencil beam at 220 MeV/u impinging the head phantom has been simulated to evaluate the origin of such tracks. From a preliminary analysis performed with a restricted event sample, it results that such particles are due to the nuclear fragmentation in the ionisation chambers material and in the air. This can be observed in figure 6.9, where the secondary fragments profile along the beam axis x, obtained using the reconstructed tracks in Dose Profiler, is shown. The three different contributions are highlighted.

At present, only a preliminary consideration on the achieved spatial resolution can be assessed. Considering the single beam spot irradiation, the y-axis profile width is approximately given by the sum of different incoherent contributions:

$$\sigma_y^2 = \sigma_{beam}^2 + \sigma_{ms}^2 + \sigma_{track}^2 \tag{6.1}$$

where $\sigma_{beam} \simeq 2$ mm is the beam size at isocenter, σ_{track} is the intrinsic back-tracing resolution of the Dose Profiler and σ_{ms} is due to the multiple scattering that the particles undergo inside the phantom. From a gaussian fit a σ_y of the order of 7.5 mm is achieved. The evaluation of the angular dispersion due to the multiple scattering in the phantom has been evaluated with the Monte Carlo simulation. In figure 6.10 the scattering angle in the space θ_0 for fragments exiting from the phantom, is shown. None energy selection is applied. A standard deviation is of the order of 2° is observed, corresponding to 35 mrad. This corresponds to a dispersion between about ~ 7 mm in the y coordinate, compatible with the measured sigma. Then, the resolution on the emission point is to be dominated by the multiple scattering, as expected.

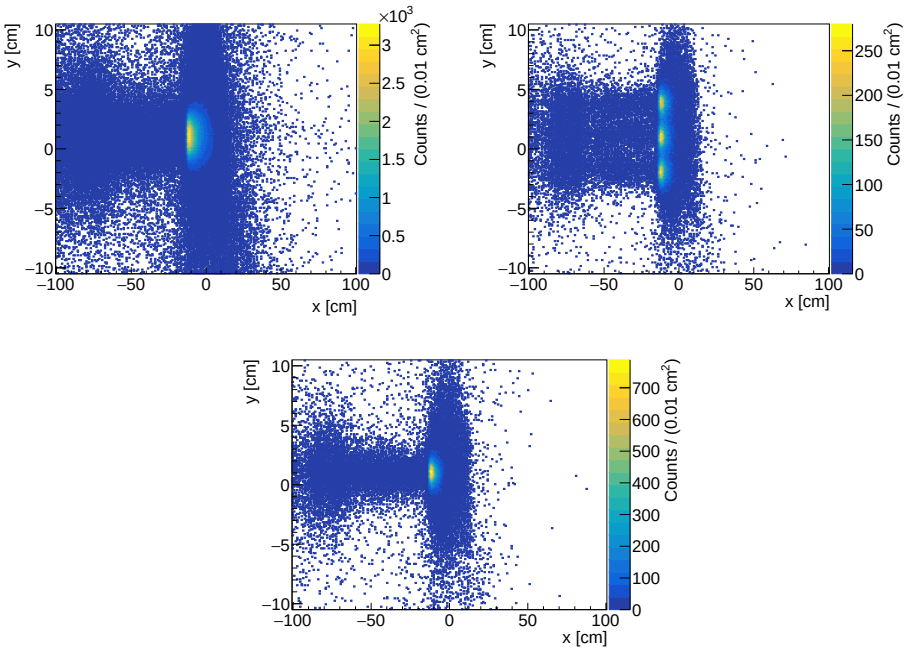

Figure 6.6. 2D distributions of all the track reconstructed in the Dose Profiler for different kind of irradiations: dose cube (top left), matrix (top right) and single pencil beam at 220 MeV/u (bottom).

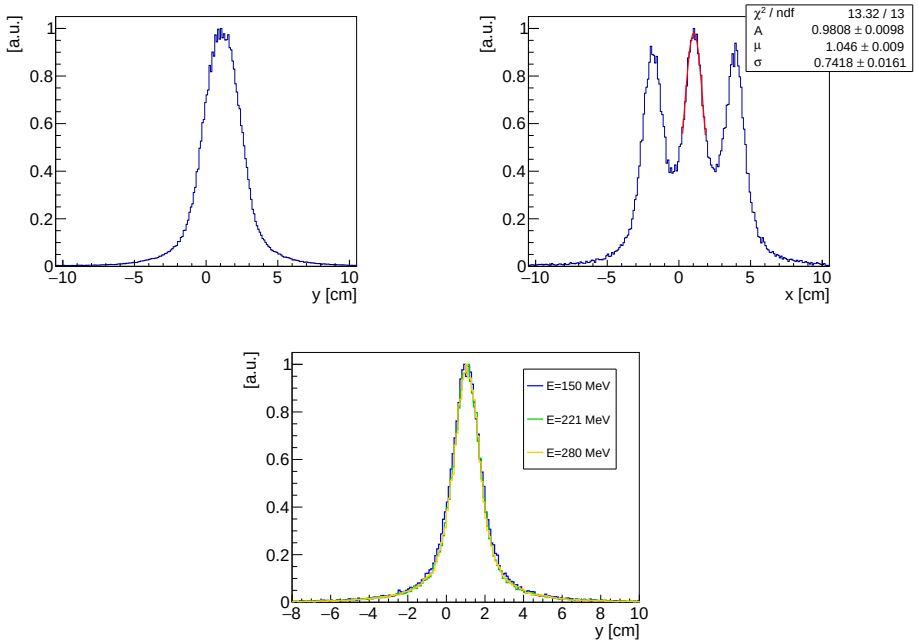

Figure 6.7. Reconstructed vertical emission point coordinate of all fragments reconstructed in the Dose Profiler for different kind of irradiations: dose cube (top left), matrix (top right) and single pencil beam at 220 MeV/u (bottom).

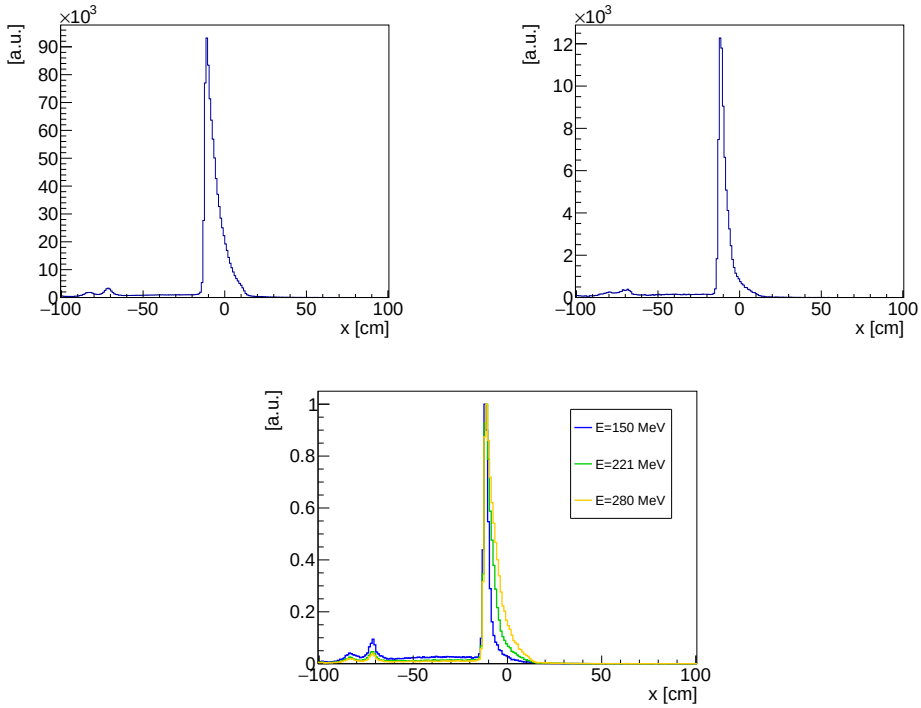

Figure 6.8. Reconstructed emission point coordinate along the beam axis x of all fragments reconstructed in the Dose Profiler for different kind of irradiations: dose cube (top left), matrix (top right) and single pencil beam at 150 MeV/u, 220 MeV/u and 280 MeV/u (bottom).

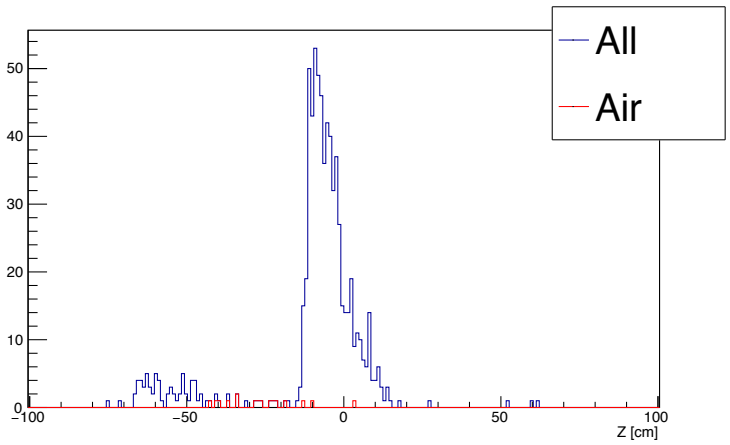

Figure 6.9. Preliminary Emission profile along the beam axis obtained by means of the Monte Carlo simulation. The reconstructed tracks below -60 cm point are produced in the ionisation chambers placed before the beam exit window.

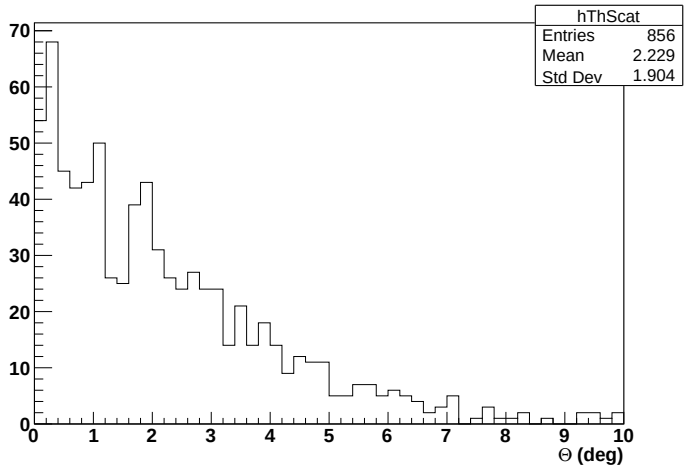

Figure 6.10. Scattering angle of fragments produced in the head phantom, evaluated with a Monte Carlo simultaion.

6.4 Feasibility study

The monitoring technique proposed in this thesis of course represents a big challenge in terms of signal modelling, because of the unavoidable difficulties in the Bragg peak retrieving procedure due to absorption in the patient, and several further studies have to be carried out to validate and refine the method. However, the fundamental issue that represents the zero-level requirement for a practicable clinical application of this technique is related to the amount of particles that are produced during a PT treatment, that deeply affects the achievable precision on the Bragg peak position. In this section some preliminary analysis performed at this purpose are presented. To understand how many tracks are expected in a treatment, firstly the number of charged secondary particles N_{fr} emitted in the field of view of the Dose Profiler by the head phantom, impinged by ^{12}C ion beam at 220 MeV/u, have been evaluated, both in the 90° and the 60° placement, assuming a distance between the detector and the phantom of 50 cm. N_{fr} has been roughly assessed using the eq. 6.2

$$N_{fr} = \frac{N_{detected}}{\varepsilon_{DT} \cdot \varepsilon_{track} \cdot \varepsilon_{\Omega}} \tag{6.2}$$

where $N_{detected}$ is the number of reconstructed tracks, ε_{DT} is a mean efficiency factor that takes into account the events loss due to the dead time, ε_{track} is the tracking efficiency, i.e. the probability to detect and track a particle that cross the Dose Profiler, and ε_{Ω} is the scaling factor due to the angular acceptance.

- $N_{detected}$ includes only the tracks whose reconstructed emission point is within the head phantom.
- ϵ_{DT} has been evaluated from the measured dead time distribution and data acquisition rate. The former is shown in figure 6.11, and the same shape measured at Trento with mono-energetic beams can be observed (see 5.2.6).

The CNAO beam has a bunched time structure (figure 6.13), so that the particles are extracted from the accelerator only during *spills* of few seconds, followed by a time interval with similar duration in which the extraction is stopped. The DAQ rate has been evaluated using 10^3 in-spill events samples, and the corresponding acquisition time. Mean rate of 6.7 kHz and 7.1 kHz are found for run at 90° and 60°, respectively, as shown in figure 6.12. ϵ_{DT} has been estimated using the simulation described in section 5.2.6, finding an event loss fraction of $\sim 64\%$ and $\sim 63\%$

- ε_{track} has been measured at Trento test-beam for different protons energies (see figure 5.15). A 90% mean efficiency value has been used in this analysis.
- In the 90° setup, the Dose Profiler is at 46 cm from the phantom, then ε_Ω is $\varepsilon_\Omega = (46\text{ cm}/50\text{ cm})^2 \simeq 0.84$. Instead, in the 60° setup, the distance between the target and the detector is 109 cm, then a factor $\varepsilon_\Omega = (50\text{ cm}/109\text{ cm})^2 \simeq 0.18$ is used.

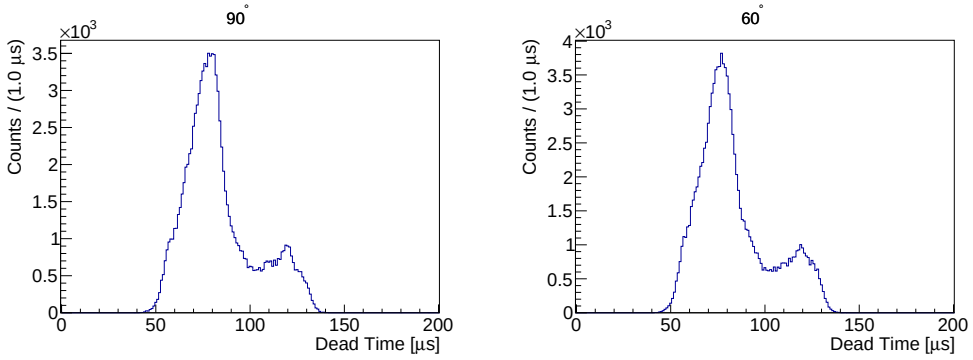

Figure 6.11. Dead time distribution measured in the 90° (left) and 60° setup (right)

.

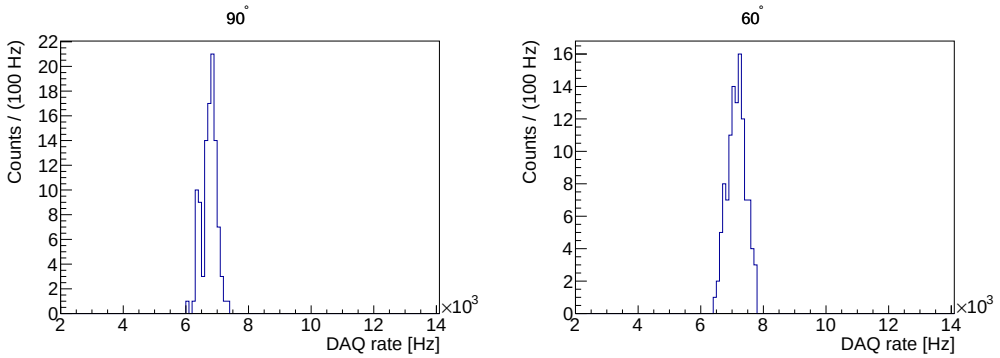

Figure 6.12. DAQ rate distribution measured in the 90° (left) and 60° setup (right).

Primary ions have been delivered at typical therapeutic intensity, so that the number of impinging primary ^{12}C ions N_{ion} could be easily provided by the ionisation chambers of the CNAO dose delivery control system. Considering the measured

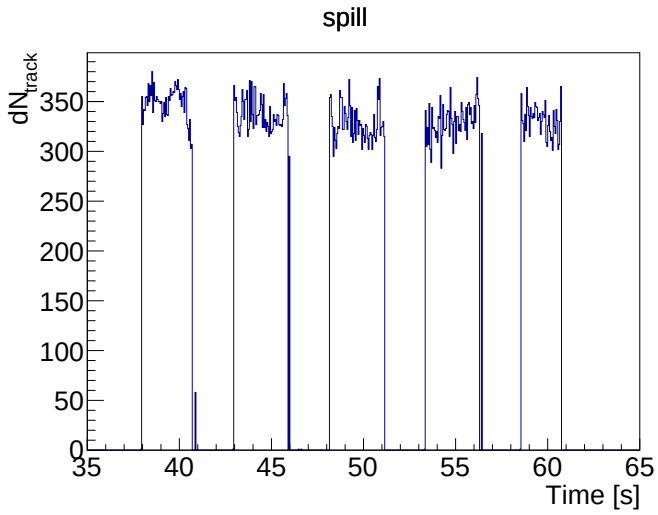

Figure 6.13. Bunched time structure of the CNAO beam, obtained counting the reconstructed fragments tracks as a function of the acquisition time.

$N_{ion} = 0.99 \cdot 10^9$, a DAQ total time of 27 s and a beam duty cycle of the order of 50%, the beam intensity was $\sim 10^8\ s^{-1}$. The estimate of the number of secondary fragments expected in a treatment has been performed rescaling N_{fr} according the number of particles planned in a treatment. We focused on the number of fragments produced by a single pencil beam N_{pb} and by a slice N_{slice}, evaluated employing a treatment plan used for a patient affected by a chondrosarcoma at CNAO, shown in figure 6.14.

	$N_{detected}$	ε_{DT}	ε_{track}	ε_{Ω}	N_{fr}	N_{ion}	N_{pb}	N_{slice}
90°	$7.9 \cdot 10^4$	64%	90%	0.84	$1.4 \cdot 10^5$	$0.99 \cdot 10^9$	12	1823
60°	$9.5 \cdot 10^4$	63%	90%	0.18	$7.8 \cdot 10^5$	$0.99 \cdot 10^9$	80	12222

Table 6.1. Preliminary evaluation of the expected number of fragments per pencil beam and per slice, in treatment conditions.

The results are summarised in table 6.1. ∼10 and ∼ 80 fragments are produced for each pencil beam, while ∼ 1200 and ∼ 18000 fragments are expected for a single slice, at 90° and 60° respectively. It immediately can be noticed that, with such geometrical acceptance, the technique described in this thesis is not suitable to monitor each single beam spot, because of the low achievable statistic. Instead, the measured number of fragments per slice would allow to achieve a millimetre-level precision on the Bragg peak position reconstruction, reminding the 3 mm resolution obtained with a 10^3 event sample, as previously reported in section 2.3.

A final consideration can be done on the Dose Profiler performances. Assuming to place the detector at 60° with respect to the beam direction at the previously considered distance of 50 cm from the patient, the expected fragments arrival rate considering a $r_{ion} = 10^8\ s^{-1}$ beam intensity is approximately given by the eq. 6.5

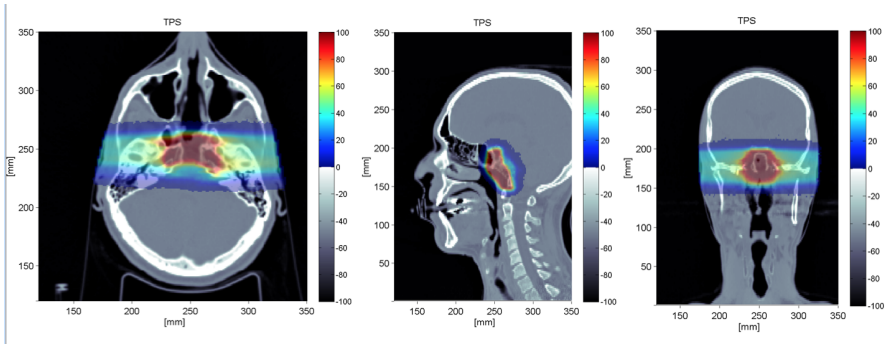

Figure 6.14. Delivered dose planned for a chondrosarcoma treatment. This treatment plan has been used to evaluate the expected number of ions per spot and per slice in clinical conditions.

.

$$r^{60^\circ} \simeq \frac{N_{fr}^{60^\circ}}{N_{ion}} r_{ion} = 180\ kHz \tag{6.3}$$

meaning that expected trigger rate have been under-estimated for the detector read-out development. The actual number of fragments N_{slice}^{DT} produced in a slice, taking into account the mean detector dead time of $83\mu s$, is drastically reduced.

$$N_{slice}^{DT} = \varepsilon_{DT}^{83\mu s} \cdot N_{slice} \simeq 1200 \tag{6.4}$$

So the data acquisition system design should be reconsidered to optimise the dead time. The lower limit imposed by the hardware design is given by the time needed to extract the data from the ASICs to the FPGAs, and the time needed to send the data from the FPGAs to the Concentrator. On the basis of the read-out procedure described in section 3.3, it results to be of the order of $20\mu s$, leading to a N_{slice}^{DT} improvement by a factor ~ 3.4

$$N_{slice}^{DT} = \varepsilon_{DT}^{20\mu s} \cdot N_{slice} \simeq 4100 \tag{6.5}$$

The remaining dead time is due to the time spent by the system to access to memory and to send the data towards the DAQ machine by means of the ethernet link. In principle, a smart data buffering system implemented in the FPGA included in the Concentrator, will allow to avoid this dead time contribution.

Conclusions

In this thesis I investigated the possibility to develop an innovative on-line beam range monitoring technique that exploits charged secondary fragments. The concept of the technique is to reconstruct the ion beam range using the correlation between the fragment emission profile fall-off and the Bragg peak position. The fragment emission points are obtained revealing and back-tracing the fragment trajectories towards the patient. The unavoidable resolution worsening because of the multiple scattering that the secondary fragments suffer inside the patient, can be balanced by a high detection efficiency and a low background contamination. Then, this technique appears particularly appealing for ^{12}C ion beams treatment monitoring, where a significant fragments emission at large angle with respect to the beam direction has been measured, and at the same time prompt-γ and PET techniques are far to achieve the required precision due to to the large neutral background.

I presented an innovative detector designed to monitor the beam range during the PT treatments, named Dose Profiler, that is under development within the INSIDE collaboration, in order to be installed in the CNAO treatment room. The Dose Profiler aims to measure the secondary fragment emission profiles, reconstructing the particle trajectories using a tracker made by six planes of scintillating fibres, read-out by SiPMs. An Absorber composed by four 6 mm plastic scintillator layers is placed beyond the tracker to provide the fragment energy. As a trade-off between the room geometrical constraints and the maximisation of the fragment detection statistics, the detector will be placed at ~ 50 cm from the patient, oriented at 60° with respect to the beam direction. The read-out and data acquisition system of the Dose Profiler has been designed and tested within this thesis work. It has planned to sustain a 20 kHz fragment rate, according the available measurements of charged secondary fragments production.

The emission profiles obtained in a real treatment are strongly dependent on the patient geometry and tumour localisation, since the emitted particles can cross different thicknesses of material, with different densities. Then, the Bragg peak position assessment is not straightforward. A method that aims to make the Bragg peak depth evaluation independent from the different absorptions is proposed. The emission profile could be reconstructed assigning a weight to each fragment according the amount of crossed materials, extracted by the patient CT. A preliminary test of the method has been performed by means a Monte Carlo simulation, showing promising results that have been published in [84]. However, the described procedure has to be still validated in real cases, and further investigations are clearly needed.

The Dose Profiler has been assembled in 2017. In my thesis work, I studied the detector response, performing measurements with Minimum Ionising Particles and

with proton beams at the energies of interest for PT applications. The detector working point in terms of gain, thresholds and temperature has been determined maximising the detection efficiency with cosmic rays. The charge resolution, the detection efficiency, the back-tracing resolution and the dead time of the detector have been investigated with a test-beam at the Trento proton-therapy centre, impinging the Dose Profiler with proton beams with energy in the range between 44 MeV and 228 MeV. The charge resolution achieved with the total amount of energy released in the tracker is of the order of 15-18 %, whereas the resolution obtained using the charge released in the Absorber is somewhat below 10 %. The detection efficiency has been evaluated for each layer, irradiating the whole detector volume with proton beams at 91 MeV/u. It results of the order of 90% for all the layers, in agreement with expectations. The back-tracing resolution has been estimated measuring the beam spot size at isocentre position, and subtracting the nominal beam size measured by the Trento staff. A resolution of 3-5 mm has been found, slightly worsening at low energies. The mean dead time is of the order of 80 μs.

Finally, the measurement of the fragment production from an anthropomorphic head phantom impinged with ^{12}C ions beams at different energies has been carried out at CNAO. The preliminary reconstructed emission profiles have been shown and the amount of produced fragments has been preliminary assessed. The clinical applicability of the technique proposed in this thesis is preliminary discussed. According the primary ion delivered in a real chondrosarcoma treatment, it clearly arises that the Dose Profiler, with such geometrical acceptance, is not suitable to monitor the beam range for each pencil beam. The number of fragments in the detector field of view per beam spot is less than 100, whereas $\sim 10^3$ events are needed to achieve a millimetre-level precision on the Bragg peak position. On the other hand, the beam range monitoring could be feasible collecting the events of a whole slice, where are emitted ~ 20000 fragments. A primary ion rate of the order of $\sim 10^8$ s^{-1} has been also measured, higher than supposed at the beginning. Hence, the detector dead time avoids to collect all the produced events, resulting in a significant events loss. A change of the Dose Profiler read-out system design is foreseen to reduce the dead time, and tests on patient will follow immediately after at CNAO.

Ringraziamenti

Non mi lascio andare tanto facilmente. Provo a farlo (un po') scrivendo questa pagina. In questi quattro anni passati a SBAI ho conosciuto tante persone. Alcune di loro oggi vivono lontano da qui, tra Foggia e Belfast. Ognuno mi ha lasciato qualcosa durante questa esperienza, che al momento prosegue e spero proseguirà ancora. Voglio ringraziare tutti, nessuno escluso, per avermi sopportato.

In particolare ringrazio Adalberto, per il suo costante supporto, i suoi insegnamenti e per la incredibile pazienza che ha avuto nei miei confronti, seguendo la stesura di questa tesi. Ringrazio Vincenzo, per i suoi preziosi consigli e il suo immancabile aiuto in qualsiasi momento, per qualsiasi motivo. Voglio anche ringraziare Riccardo, con il quale ho intrapreso questa strada ormai quattro anni fa, con la mia tesi di laurea.

Un enorme grazie va ovviamente a Michela, per troppe cose. E ad Alessio, dal quale ho imparato tantissimo. Ti giuro che prima o poi verrò a correre con te sotto al ?rocione. Grazie a tutta la classe '92 del laboratorio per tutti i bei momenti che abbiamo condiviso: Debora (ogni tanto ho bisogno di risentire la nostra playlist), Riccardo, Micol, Marta. Ci metto in mezzo pure Eliana, tanto nessuno se ne accorgerebbe. Un grazie non può non andare a tutti i fisici *acquisiti* da SBAI: Federico, Alessandro, Vincenzo, Bob.

Voglio ringraziare Marco, per le splendide colonne sonore che hanno accompagnato le nostre lunghe giornate in laboratorio. Grazie a tutti i milanesi, in particolare a Ilaria (un test-beam senza di te non è la stessa cosa) la cui anima rimarrà sempre romana. Grazie a Valentina, per la sua allegria (e follia). Grazie a Martina, e a Paola M.F che mancano a tutti.

Tra tutti questi grazie, non possono mancare Grazia, Graziella e... (tanto per stemperare il terribile tono da *malinconia portami via* che percepisco rileggendo...)

Se ho raggiunto questo piccolo (ma importante) obiettivo, lo devo anche e soprattutto a tutti coloro hanno provato con tutto il loro cuore a starmi vicino, nonostante tutto. Non leggeranno mai questa pagina, ma il mio ultimo grazie va a loro.

Bibliography

[1] WHO. *Cancer report*. 2017. URL: http://www.who.int/mediacentre/factsheets/fs297/en/.

[2] Giaccia A. Lawrence TS Ten Haken RK. *Cancer: Principles and Practice of Oncology. 8th edition*. Lippincott Williams and Wilkins, 2008.

[3] Powell ME Taylor A. "ntensity-modulated radiotherapy, ĂŤwhat is it?" In: *Cancer Imaging* 4(2) (2004), pp. 68–73.

[4] R. Wilson. "Radiological use of fast protons". In: *Radiology* 47 (1946), pp. 487–491.

[5] PTCOG. 2017. URL: https://www.ptcog.ch/index.php/mission.

[6] Glenn F. Knoll. *Radiation Detection and Measurement 3rd edition*. John Wiley & Sons: New York, 2000.

[7] W. Jackson. *Techniques for nuclear and particle physics experiments*. Springer-Verlag: Berlin, Heidelberg, 1987.

[8] W. Leo. *Techniques for nuclear and particle physics experiments*. Springer-Verlag: Berlin, Heidelberg, 1987.

[9] Teruhiko T.and others. "Systematic Review: Charged-Particle Radiation Therapy for Cancer". In: *Ann. Intern. Med.* 8 (2009), pp. 556–565.

[10] Y.S. Tsai. In: *Rev. Mod. Phys* 46 (1974), p. 815.

[11] Schardt Dieter and Elsasser Thilo. "Heavy-ion tumor therapy: Physical and radiobiological benefits". In: *Reviews of modern physics* 82 (2010), pp. 323–425.

[12] Kraan A.C. "Range verification methods in particle therapy:underlying physics and Monte Carlo modeling". In: *Front Oncol* 5 (2015), p. 150.

[13] Gottschalk B. "Physics of proton interactions in matter". In: *Proton Therapy Physics* (2012), pp. 19–60.

[14] Cussol D. "Nuclear Physics and Hadron Therapy". In: *La Colle sur Loup: Lectures at Ecole Joliot Curie* (2011).

[15] D Schardt. "Precision Bragg-curve measurements for light- ion beams in water". In: *GSI-Report 2008-1* (2008), p. 150.

[16] L Sihver. "Depth-dose distributions of high-energy carbon, oxygen and neon beams in water". In: *Jpn. J. Med. Physics* 18 (2003), pp. 1–21.

[17] Giaccia A. Hall E. *Radiobiology for the Radiologist*. Philadelphia: Lippincott Williams and Wilkins, 2012.

[18] Sutherland B.M. Hada M. “Spectrum of complex DNA damages depends on the incident radiation”. In: *Radiat. Res* 165 (2006), pp. 223–230.

[19] Kramer M. “Calculations of heavy-ion track structure”. In: *Nucl. Instr. Meth. Phys. Res. B* 105 (1995), pp. 14–20.

[20] Scholz M. “Effects of ionradiation on cells and tissues”. In: *Adv.Polym.Sci.* 62 (2003), pp. 96–155.

[21] Paganetti H. and others. “Suit, H.D. Relative biological effectiveness (RBE) values for proton beam therapy”. In: *Int. J. Radiat. Oncol. Biol. Phys* 53 (2002), pp. 407–421.

[22] Paganetti H. “Relative biological effectiveness (RBE) values for proton beam therapy. Variations as a function of biological endpoint, dose, and linear energy transfer.” In: *Phys. Med. Biol.* 59 (2014), pp. 417–472.

[23] Durante M. Tommasino F. “Proton radiobiology”. In: *Cancers* 7 (2015), pp. 353–381.

[24] Puck T. T. and Marcus P.I. “Action of x-rays on mammalian cells,” in: *J. Exp. Med.* 103 (1956), pp. 653–666.

[25] C. A. Tobias E. A. Blakely et al. “Inactivation of human kidney cells by high-energy monoenergetic heavy-ion beams”. In: *Radiation Research* 80 (1979), pp. 122–160.

[26] D. K. Bewley. “A comparison of the response of mammalian cells to fast neutrons and charged particle beams”. In: *Radiation Research* 34 (1968), pp. 446–458.

[27] C. J. Koot G. W. Barendsen et al. “The effect of oxygen on impairment of the proliferative capacity of human cells in culture by ionizing radiations of different let”. In: *International Journal of Radiation Biology* 10 (1966), pp. 317–327.

[28] K. Fukutsu Y. Furusawa et al. “Inactivation of aerobic and hypoxic cells from three di erent cell lines by accelerated 3he-, 12c- and 20ne- ion beams”. In: *Radiation Reasearch* 154 (2000), pp. 485–496.

[29] D. Zukowski A. Staab et al. “Response of chinese hamster v79 multicellular spheroids exposed to high-energy carbon ions”. In: *Radiation Reasearch* 161 (2004), pp. 219–227.

[30] Pedroni E. et al. “A second generation proton scanning gantry”. In: *Z. Med. Phys* 14 (2004), pp. 25–34.

[31] Furukawa T. et al. “Design study of a raster scanning system for moving target irradiation in heavy-ion radiotherapy”. In: *Med. Phys* 44 (2007), pp. 1085–1097.

[32] Bortfeld T et al. “Effects of intra-fraction motion on IMRT dose delivery: Statistical analysis and simulation”. In: *Phys. Med. Biol.* 47 (2002), pp. 2203–2220.

[33] Minohara S. et al. “Respiratory gated irradiation system for heavy-ion radiotherapy”. In: *Int. J. Radiat. Oncol., Biol., Phys.* 47 (2000), pp. 1097–1103.

[34] Durante M. Bert C. “Motion in radiotherapy: particle therapy.” In: *Phys. Med. Biol.* 56 (2011), pp. 113–144.

[35] Assi A. et al. “Tumor tracking method based on a deformable 4D CT breathing motion model driven by an external surface surrogate”. In: *Int J Radiat Oncol Biol Phys* 88 (2014), pp. 182–188.

[36] Schlosser J. et al. “Tele-robotic system concept for real-time soft-tissue imaging during radiotherapy beam delivery.” In: *Med. Phys.* 37 (2010), pp. 6357–6367.

[37] Trofimov A. et al. “Tumor trailing strategy for intensity-modulated radiation therapy of moving targets.” In: *Med. Phys.* 35 (2008), 1718?1733.

[38] Seregni M. et al. “Tumor tracking based on correlation models in scanned ion beam therapy: an experimental study.” In: *Phys. Med. Biol.* 58 (2013), pp. 4659–4678.

[39] Tashiro M et al. “Technical approach to individualized respiratory-gated carbon-ion therapy for mobile organs”. In: *Radiol. Phys .Technol* 6 (2013), pp. 356–366.

[40] Rietzel E. et al. “Moving targets: detection and tracking of internal organ motion for treatment planning and patient set-up”. In: *Radiother. Oncol.* 73 suppl.2 (2004), pp. 68–72.

[41] Paganetti H. “Range uncertainties in proton therapy and the role of Monte Carlo simulations”. In: *Phys. Med. Biol.* 57 (2012), pp. 99–117.

[42] O. Jackel C. P. Karger et al. “Clinical dosimetry for heavy ion therapy”. In: *Zeitschrift fur Medizinische Physik* 169 (2002), pp. 159–169.

[43] Batista V. et al. “Planning strategies for inter-fractional robustness in pancreatic patients treated with scanned carbon therapy”. In: *Radiation and Oncology* 12 (2017), p. 94.

[44] A. Knopf and A. Loma. “In vivo proton range verification: a reviewy”. In: *Phys. Med. Biol.* 58 (2013), pp. 131–160.

[45] Raju M.R. Maccabee H.D. Madhvanath U. “Tissue activation studies with alpha-particle beams.” In: *Phys. Med. Biol.* 14 (1969), pp. 4445–4455.

[46] C. Agodi et al. “Study of the time and space distribution of $\beta+$ emitters from 80 MeV/u carbon ion beam irradiation on PMMA”. In: *Nuclear Instruments and Methods in Physics Research, Section B: Beam Interactions with Materials and Atoms* 283 (2012), pp. 1–8.

[47] K. Parodi and Others. “In-beam PET measurements of β^+ radioactivity induced by proton beams”. In: *Physics in medicine and biology* 47 (2002), pp. 21–36.

[48] Beebe W.J et al. “Simulation of proton therapy treatment verification via PET imaging of induced positron emitters”. In: *IEEE Nuclear Science Symposium and Medical Imaging Conference (NSS/MIC) Conference Records. Portland, Oregon* (2003).

[49] URL: `EXFOR,ExperimentalNuclearReactionDataFile,http://wwwnndcbnlgov/nndc/exfor/..`

[50] Enghardt W. et al. “Dose quantification from in-beam positron emission tomography.” In: *Radiother. Oncol.* 73 (2004), pp. 96–98.

[51] Enghardt W. et al. “Charged hadron tumour therapy monitoring by means of PET”. In: *Nucl Instrum Methods A* 525 (2004), pp. 284–288.

[52] K. Parodi. “PET monitoring in hadrontherapy”. In: *Nuclear Medicine Review* 15 (2002), pp. 37–42.

[53] Min CH et al. “Clinical application of in-room positron emission tomography for in vivo treatment monitoring in proton radiation therapy.” In: *Int J Radiat Oncol Biol Phys.* 86 (2013), pp. 183–189.

[54] Parodi K. et al. “Patient study on in-vivo verification of beam delivery and range using PET/CT imaging after proton therapy”. In: *Int J Radiat Oncol Biol Phys* 68 (2007), pp. 920–934.

[55] Hishikawa Y. et al. “Usefulness of positron-emissiontomographic images after proton therapy”. In: *Int J Radiat Oncol Biol Phys* 53 (2002), pp. 1388–1391.

[56] Zhu X. et al. “Monitoring proton radiation therapy with in-room PET imaging”. In: *Phys Med Biol* 56 (2011), pp. 4041–4057.

[57] Ferrero V. et al. “The INSIDE project: on-line monitoring and simulation validation with the in-beam PET scanner”. In: *Journal of Physics: Conference Series* 841 (2017), p. 012011.

[58] Y. Jongen F. Stichelbaut. “Verification of the proton beams position in the patient by the detection of prompt gamma-rays emission”. In: *39th Meeting of the Particle Therapy Co-Operative Group, San Francisco, CA.* (2003).

[59] P. Testa et al. “Dose profile monitoring with carbon ions by means of prompt-gamma measurements”. In: *Nuclear Instruments and Methods in Physics Research B* 267 (2009), pp. 993–996.

[60] Pinto M. et al. “Absolute prompt-gamma yield measurements for ion beam therapy monitoring”. In: *PMB* 60 (2015), p. 565.

[61] C. Agodi et al. “Precise measurement of prompt photon emission for carbon ion therapy”. In: *JINST* 7 (2012), P03001.

[62] Mattei I. et al. “Prompt-γ production of 220 MeV/u ^{12}C ions interacting with a PMMA target”. In: *PMB* 10 (2015).

[63] Min C.H. et al. “Prompt gamma measurements for locating the dose falloff region in the proton therapy”. In: *Appl. Phys. Lett. 89* 18 (2006).

[64] Krimmer J . et al. “Collimated prompt gamma TOF measurements with multi-slit multi-detector configuration”. In: *J. Instrum. 10* 1 (2015).

[65] Smeets J . et al. “Prompt gamma imaging with a slit camera for real-time range control in proton therapy”. In: *PMB* 57 (2012), pp. 3371–3405.

[66] M. H. Richard . et al. “Design guidelines for a double scattering compton camera for prompt gamma imaging during ion beam therapy: a monte carlo simulation study”. In: *Trans. Nucl. Sci* 58(1) (2011), pp. 87–94.

[67] Fernando Hueso-González et al. “Compton Camera and Prompt Gamma Ray Timing: Two Methods for In Vivo Range Assessment in Proton Therapy”. In: *Front. Oncol.* 6 (2016).

[68] Golnik C. et al. “Range assessment in particle therapy based on prompt-γ ray timing measurements”. In: *Phys. Med. Biol.* 59(18)) (2014), p. 5399.

[69] F. Hueso-Gonzàlez et al. “First test of the prompt gamma ray timing method with heterogeneous targets at a clinical proton therapy facility”. In: *Phys. Med. Biol.* 60(16)) (2015), p. 6247.

[70] Agodi C et al. “FIRST experiment: fragmentation of ions relevant for space and therapy”. In: *J Phy Conf Series* (2013).

[71] Pleskac R et al. “The FIRST experiment at GSI”. In: *Nucl Instrum Meth A* 678 (2012), p. 130.

[72] Braunn B et al. “Nuclear reaction measurements of 95 MeV/u 12-C interactions on PMMA for hadronherapy”. In: *Nucl Instrum Meth B* 269 (2011), p. 2676.

[73] Gunzert-Marx K. et al. “Secondary beam fragments produced by 200 MeV/u 12-C ions in water and their dose contributions in carbon ion radiotherapy”. In: *New J Phys* (2008).

[74] Agodi C. et al. “Charged particle?s flux measurement from PMMS irradiated by 80 Mev/u carbon ion beam”. In: *Physics in Medicine and Biology* 57(18) (2012), p. 5667.

[75] L. Piersanti et al. “Measurement of charged particle yields from PMMA irradiated by a 220 MeV/u C_{12} beam”. In: *Physics in Medicine and Biology* 59 (2014), pp. 1857–1872.

[76] Mattei I. et al. “Addendum: Measurement of charged particle yields from PMMA irradiated by a 220 MeV/u C_{12} beam”. In: *Physics in Medicine and Biology* 62 (2017).

[77] Ciciriello F. et al. “BASIC32_ADC, a Front-end ASIC for SiPM Detectors”. In: *Nuclear Science Symposium and Medical Imaging Conference (NSS/MIC), IEEE* (2013), pp. 1–6.

[78] *LWIP*. URL: `https://savannah.nongnu.org/projects/lwip/`.

[79] Hough P.V.C. “Method and means for recognizing complex patterns”. In: *U.S. Patent 3,069,654* (1962).

[80] R. O. Duda and P. E. Hart. “Use of the Hough Transformation to Detect Lines and Curves in Pictures”. In: *Comm. ACM* 15 (1972), pp. 11–15.

[81] R. E. Kalman. “A new approach to linear filtering and prediction problems”. In: *Transactions of the ASME. Series D, Journal of Basic Engineering* 82 (1960), pp. 35–45.

[82] Hoppener C et al. “A novel generic framework for track fitting in complex detector systems”. In: *Nuclear Instruments and Methods in Physics Research A* 620 (2010), pp. 518–525.

[83] Johannes Rauch and Tobias Schluter. “GENFIT - a Generic Track-Fitting Toolkit”. In: *Journal of Physics: Conference Series* 8 (2015), Conference 1.

[84] Traini G. et al. “Design of a new tracking device for on-line beam range monitor in carbon therapy”. In: *Physica Medica* 34 (2017), pp. 18–27.

[85] Tommasino F. et al. “Proton beam characterisation in the experimental room of the Trento Proton Therapy facility”. In: *Nuclear Inst. and Methods in Physics Research, A* 869 (2017), pp. 15–20.

[86] Schneider et al. “The calibration of CT Hounsfield units for radiotherapy”. In: *PMB.* 41 (1996), pp. 111–124.